SAPIENZA
UNIVERSITÀ DI ROMA

Dottorato di Ricerca in Scienza dei Materiali – XXV Ciclo

Growth Morphology, Electronic Properties and Interaction of Organo-Metallic Molecules Adsorbed on Graphene

Candidate: Mattia Scardamaglia

Thesis advisor:
Prof. Carlo Mariani

Ph.D. school coordinator:
Prof. Ruggero Caminiti

20 November 2012

Contents

Introduction

Since the isolation of a single graphene flake in 2004, the extraordinary electronic, optical and mechanical properties of this one-atom-thick material emerged, attracting a continuous rising interest both from fundamental and technological perspectives.

Within this research field, a key challenge is to move from model structures to more complex configurations: being graphene a surface without bulk, its properties are very sensitive to local perturbations, but the countless possibilities of modifying graphene properties by suitable functionalization procedures with atoms or molecules are still largely unexplored. The possibility to control and tailor the electronic, morphological and transport properties of graphene, by influencing its band parameters and interaction strength, is a requirement in the perspective of nanodevices fabrication. Furthermore, the effect that graphene itself could have on the molecular or metal nanostructure deposited onto it is an intriguing ambivalence of the graphene functionalization. However, reproducibility and reliability is still an issue.

An important help in the formation of ordered and reproducible nano-architectures on graphene comes from the epitaxial growth of graphene on hexagonally close-packed surfaces of transition metals, when a slightly mismatched lattice structure between these two materials occurs. This leads to the formation of an ordered modulation of the graphene sheet, also known as moiré pattern. This superstructure, whose actual geometrical and chemical corrugation depends on the degree of interaction with the substrate, can be used as a template for the formation of ordered arrays of adsorbates. Using epitaxial graphene with a nanoscale controlled corrugation leads to the opportunity to create regular 1D and 2D architectures by atom or molecular adsorption in order to tailor the electronic, magnetic or transport properties of these low-dimensional structures. A

fascinating perspective is to study arrays of size-selected magnetic nanoclusters or systems comprising a single magnetic atoms embedded in an organic frame in interaction with the graphene-metal support to elucidate their structural, electronic and magnetic properties: self-assembling of nanosized architectures is attractive for basic investigations as well as for device applications. In particular, supramolecular ordered assembly of metalorganic molecules on graphene is a suitable way to obtain regular nano-architectures with the magnetic atoms ordered in a spin network.

This Thesis lies within the scientific background described so far and it constitutes a first step on the way of the research in this field. The aim of this work is addressed to the control and the tuning of the electronic properties of regular arrays of organo-metallic molecules, metal-phthalocyanines, with a single magnetic atom embedded in an organic frame in interaction with the nanopatterned graphene-metal support. Magnetic properties represent a further step, only initially analysed here.

An introduction to the scientific background and an update state of the art is given in the first Chapter.

Chapter 2 presents the complementary experimental techniques which have been used to investigate the nature of the interaction in the materials, from an electronic and structural point of view. High-resolution angular-resolved photoemission spectroscopy will ensure a fine control of the electronic states as well as synchrotron-based X-ray techniques. A first task to achieve is the preparation of suitable metal-supported graphene ensuring a low interaction with the substrate while maintaining a natural corrugation to be exploited for molecular self-assembling. Within this context, the *in situ* growth of graphene has been an important part of this work; it consisted in an effort to design a new suitable experimental upgrading adaptable to the present experimental stage in order to reach the high temperatures required. This now allows, at the LoTUS Laboratory in Rome, the growth of graphene on different transition metals, among them iridium.

The characterization of the graphene sheet is described in Chapter 3, highlighting the most important properties that makes graphene epitaxially grown on Ir(111) the suitable substrate for metal-phthalocyanine adsorption.

A second task is the characterization of the metal-phthalocyanine molecules

deposited on graphene, described in Chapter 4. The control and the tuning of the coupling between the central metal atom of the molecules and the graphene layer is a fundamental point that determines the nature of the interaction. By investigating the effect on the graphene and molecular properties exploiting several spectroscopic techniques we aim to solve the puzzling problem of the balance between molecule-molecule and molecule-substrate interaction.

List of Publications

The results presented in this Thesis have been part of the following papers, which are referred to in the text by their Roman numerals.

I **Metal-Phthalocyanine Array on the Moiré Pattern of a Graphene Sheet**
M. Scardamaglia, G. Forte, S. Lizzit, A. Baraldi, P. Lacovig, R. Larciprete, C. Mariani, and M.G. Betti.
Journal of Nanoparticle Research, 13:6013, 2011.

II **Graphene Induced Substrate Decoupling and Ideal Doping of Self-Assembled Iron-Phthalocyanine Single Layer**
M. Scardamaglia, S. Lisi, A. Lizzit, S. Baraldi, R. Larciprete, C. Mariani, and M.G. Betti.
The Journal of Physical Chemistry C, in press, 2012.

III **Adsorption Energy of Iron-Phthalocyanine on Crystal Surfaces**
C. Struzzi, M. Scardamaglia, M. Angelucci, L. Massimi, C. Mariani, and M.G. Betti
Il Nuovo Cimento, in press, 2012.

IV **Adsorption Energy of Metal-Phthalocyanines on Graphene/Ir(111)**
M. Scardamaglia, *et al.*
in preparation.

V **Enhanced Magnetic Dichroism and Anisotropy in a Single Layer FePc on Graphene/Ir(111)**
S. Lisi, M. Scardamaglia, *et al.*
in preparation.

I have contributed to the experimental results in the following papers that are not included in this Thesis.

- **Nonenzymatic Ligation of an RNA Oligonucleotide Analyzed by Atomic Force Microscopy**
  S. Pino, M. Biasiucci, M. Scardamaglia, G. Gigli, M.G. Betti, C. Mariani, and E. Di Mauro.
  The Journal of Physical Chemistry B, 115:6296, 2011.

- **Cooling Dynamics and Thermal Interface Resistance of Glass-Embedded Metal Nanoparticles**
  V. Juvé, M. Scardamaglia, P. Maioli, A. Crut, S. Merabia, L. Joly, N. Del Fatti, and F. Vallée.
  Physical Review B, 80:195406, 2009.

Chapter 1

Low-dimensional structures

This is an introductory Chapter in which the two leading character of this Thesis are presented: graphene and metal-phthalocyanines. We contextualize this work in a scientific background and finally the state of the art of the research in this field and our aim are discussed.

1.1 Graphene: the carbon wonderland

The origin of graphene, as it is known nowadays, has to be traced back in... 2004! Within only eight years from its first isolation[1,2], the graphene topic in the scientific literature is exploded and the number of papers with the word *graphene* in the title rose from 20 in 2004 to more than 4000 in 2011. This exponential trend is reported in Fig. (1.1 left), neither to much influenced by the Nobel Prize in Physics assigned in 2010 to the two scientists A. K. Geim and K. S. Novoselov "*for groundbreaking experiments regarding the two-dimensional material graphene*" [3]. This new material earns many superlatives to its name and attracted so many researchers from a lot of different backgrounds since its extraordinary properties range from electrical and thermical conductivity, to elasticity, strength, transparency, impermeability, relativistic behaviour or even "only" its geometry: it is the first example of truly bidimensional atomic crystal, the thinnest object ever obtained. Graphene has captured the interest and imagination not only of the scientific community, but also of "common people" and media, thanks to the huge potential fascinating applications that it may reserve,

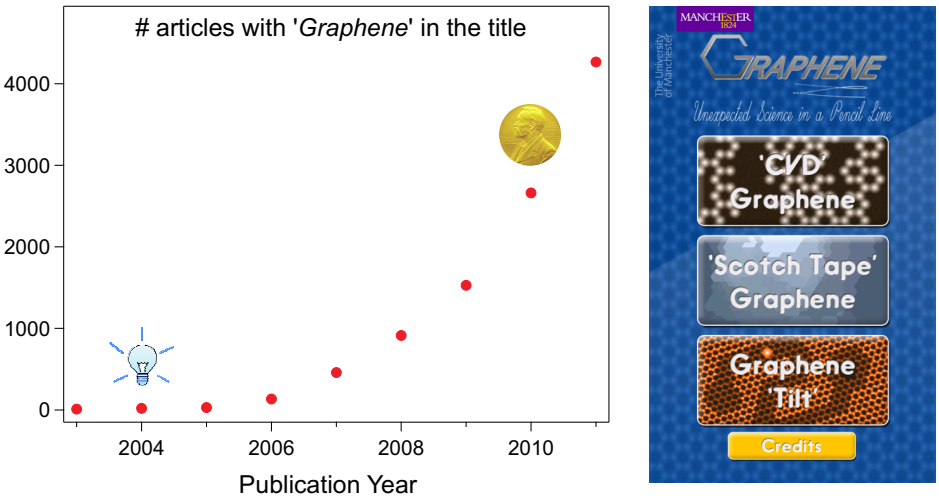

Figure 1.1: Left) Trend of the articles with *graphene* in the title during years (realized with data taken on isiweb). Right) Screenshot of the *Graphene Games* application in the Google Play Store; the games have been created for an exhibit at the Royal Society Summer Science Exhibition in London (July, 2011).

as testified by the presence of graphene-related applications also in the Google Play Store for Android (a screenshot is presented in Fig. (1.1 right)). It does not happen very often that a new substance only just discovered becomes so useful that it defines an era.

In the case of semiconductors, their 2D nature is due to quantum size effects that make the degrees of freedom for electron motion in the short direction irrelevant, but they however have a thickness that typically extends from 10 to 100 atomic layers. Graphene, instead, is a one-atom-thick crystal, a material that should not exist: a series of works by Peierls[4,5], Landau[6,7], Mermin[8] and Wagner[9] demonstrated the theoretical impossibility of long-range ordering (crystallographic or magnetic) in 2D at any finite temperatures, due to thermodynamically instabilities. Not the same thoughts as Abbott in 1884 in his novel *Flatland*... Actually this discrepancy is overcome by the support of 3D materials over which the 2D crystallites are quenched in a metastable phase and by a natural corrugation in the third dimension of the graphene sheet that suppresses thermal vibrations.

Paradoxically, this unpredictable 2D material has been experimentally discovered with a quite simple technique: the scotch tape method (or micromechanical cleavage) that consists in exfoliating bulk graphite. Revolutionary as much as for-

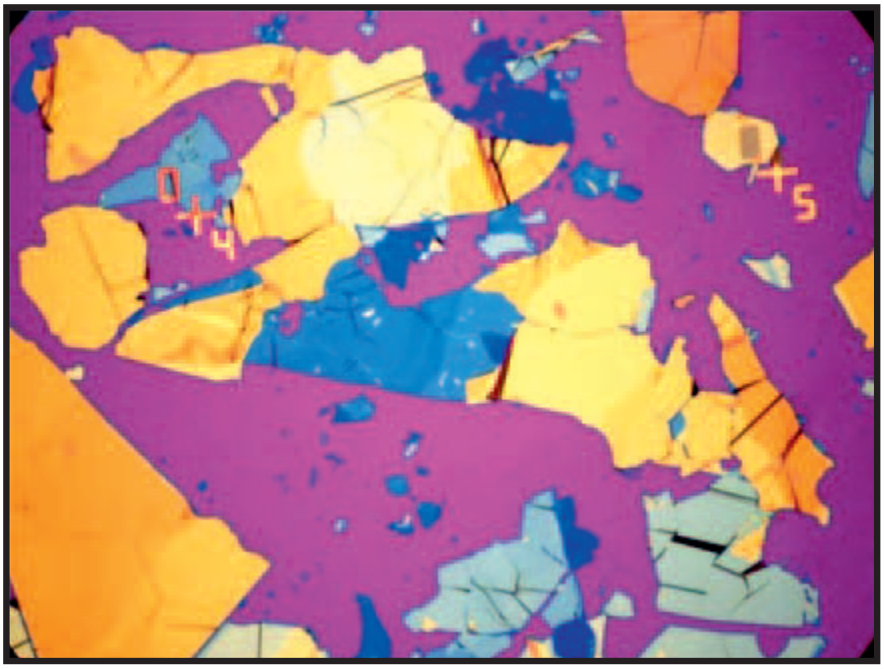

Figure 1.2: Thin graphitic flakes on a surface of Si/SiO_2 wafer (300 nm of SiO_2, purple colour). The different colours correspond to flakes of differing thicknesses, from $\sim$100 nm (the pale yellow ones) to a few nanometres (a few graphene layers - the most purple ones). The scale is given by the distance between the lithography marks (200 μm)[10].

tuitous discovery was the choice of the substrate on which to press the graphitic flakes against: oxyde silicon wafer (Si/SiO_2). Monolayers of graphite on this substrate produce a faint optical contrast for some wavelengths of incoming light, visible with an optical microscope, as we can see in Fig. (1.2).

However, there exist unaware and unlucky precursors of graphene: graphite intercalation compounds[11,12] and carbon monolayers derivating from catalytic cracking of hydrocarbons on metal surfaces[13–15] studied since the 1970s, but the electronic properties of this graphene was not investigated in detail.

In the next paragraphs we will give a short introduction in the description of graphene, starting from its geometric and electronic structure, we will concentrate then on graphene supported on transition metal substrates, and finally we will describe some of the most appealing properties that make graphene the future's material.

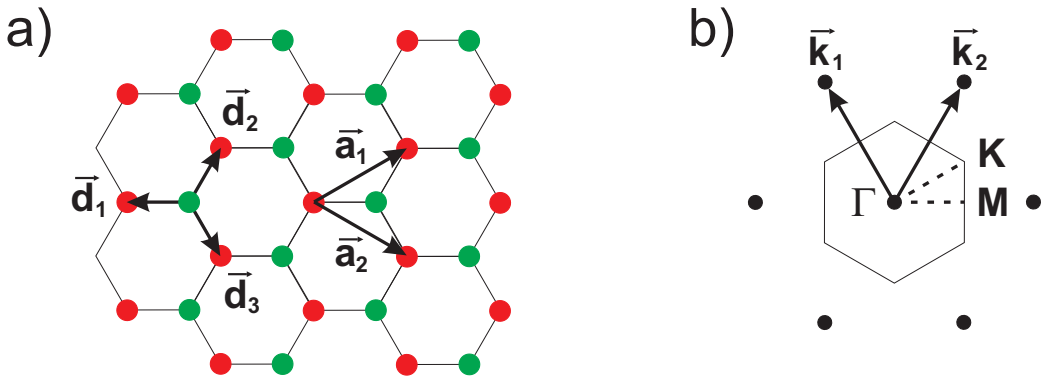

Figure 1.3: *a)* Direct honeycomb lattice, the two sublattices are made out of different colours. Also indicated the two direct lattice vectors $\mathbf{a}$ and the three earest-neighbour vectors $\mathbf{d}$. *b)* Brillouin Zone in the reciprocal space, with indicated the high symmetry points Γ, K and M and the reciprocal lattice vectors $\mathbf{k}$.

1.1.1 Lattice and electronic structure

Graphene is constituted by a honeycomb (or chicken wire...) lattice of carbon atoms arranged at the vertices of a hexagon. The honeycomb structure is generated by the presence of two atoms per unit cell, consisting in two interpenetrating triangular lattices: the sits of one sublattice are the centers of triangles defined by the other. The overall direct lattice is hexagonal, as clarified in Fig. (1.3 a) where the two sublattices are depicted with different colours.

An hexagonal structure is characterized by the lattice vectors:

$$\mathbf{a_1} = \frac{a}{2}\begin{pmatrix} 3 \\ \sqrt{3} \end{pmatrix}; \mathbf{a_2} = \frac{a}{2}\begin{pmatrix} 3 \\ -\sqrt{3} \end{pmatrix}, \tag{1.1}$$

where a=1.42 Å is the distance between two neighbour atoms in graphene. The three nearest-neighbour vectors are therefore:

$$\mathbf{d_1} = a\begin{pmatrix} -1 \\ 0 \end{pmatrix}; \mathbf{d_2} = a\begin{pmatrix} 1 \\ \sqrt{3} \end{pmatrix}; \mathbf{d_3} = a\begin{pmatrix} -1 \\ \sqrt{3} \end{pmatrix}. \tag{1.2}$$

The reciprocal lattice has again a hexagonal structure but rotated by 30° with

respect to the direct lattice, and its basis vectors are:

$$\mathbf{k_1} = \frac{2\pi}{3a}\begin{pmatrix} 1 \\ \sqrt{3} \end{pmatrix}; \mathbf{k_2} = \frac{2\pi}{3a}\begin{pmatrix} 3 \\ -\sqrt{3} \end{pmatrix}. \tag{1.3}$$

In the reciprocal space, with the Wiegner-Seitz method, we can construct the Brillouin zone and identify the high-symmetry point Γ, K and M, Fig. (1.3 b).

The carbon atoms in the basal plane are bound together by strong covalent bonds, sp^2 hybrids which are orbitals pointing in the direction of the neighbouring atoms. Since each carbon atom has four electrons available for bonding, three of them are assigned to these trigonally directed orbitals, which form σ states. The fourth electron has p_z symmetry, which is oriented normal to the σ-bonding plane and forms the highest occupied valence band π state continuing to the lowest unoccupied π* state.

The band dispersion can be calculated with a standard tight binding approximation[16–18],

$$E(\mathbf{k})_{\pm} = \pm t\sqrt{3 + f(\mathbf{k})} - t' f(\mathbf{k}) \tag{1.4}$$

with

$$f(\mathbf{k}) = 2\cos(\sqrt{3}k_y a) + 4\cos(\frac{\sqrt{3}}{2}k_y a)\cos(\frac{3}{2}k_x a), \tag{1.5}$$

where t and t' are the nearest-neighbour and the next nearest-neighbour hopping energy, the $+$ $(-)$ sign applies to the π* (π) band. We can see a plot of both σ and π bands in Fig. (1.4). By zooming around the high symmetry K point of the SBZ a conical dispersion can be seen: the valence and conduction π bands, in a neutral graphene sheet, meet exactly at the Fermi level with the energy varying linearly with the momentum, generating a zero-gap semiconductor. Near the K point, in fact, the energy dispersion assume the form

$$E(\mathbf{k})_{\pm} \approx \pm v_F \mid \mathbf{k} \mid \tag{1.6}$$

with a Fermi velocity $v_F \approx 1 \times 10^6$ m/s independent from the momentum, differently from the common crystals where a quadratic behaviour in momentum is found; this is what really makes graphene special.

By simple geometrical considerations due to the symmetry of the honeycomb lattice, an energy dispersion typical of ultrarelativistic massless particles has been

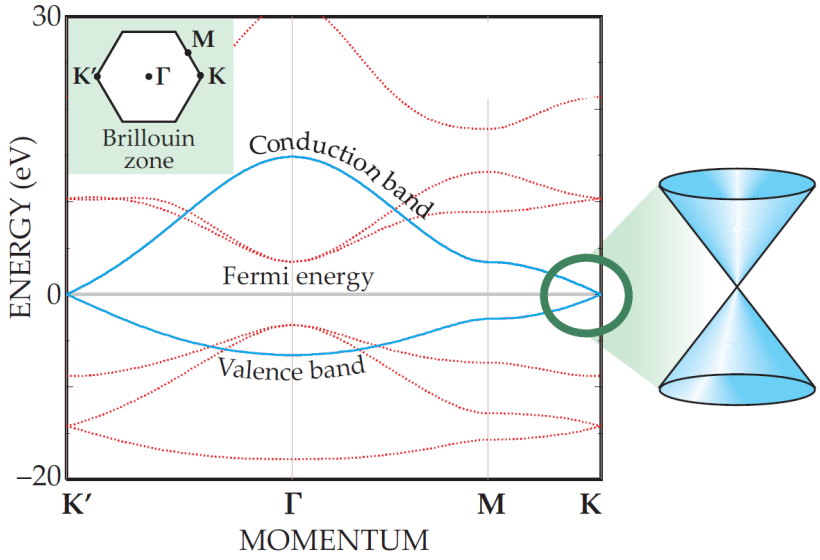

Figure 1.4: Tight binding calculation of the band dispersion in graphene. In red (blue) the bands with σ (π) symmetry. In inset the SBZ. Sketched a zoom of the Dirac cone[19].

obtained. The low-energy quasiparticles can in fact be described by a Dirac-like hamiltonian, rather than the Schrödinger equation[18,19]. The experimental discovery of graphene allows then a way to probe quantum electrodynamics phenomena by measuring its electronic properties in a traditional condensed-matter experiment. Some "exotic" consequences of the unusual Dirac fermions in graphene, that give us the taste of QED, are the half integer quantum Hall effect with non zero Berry's phase[20–22] measured even at room temperature[20] and the observation of the Klein paradox[23,24] that leads to perfect electron-to-hole conversion at a potential barrier, and an equal to unity probability of tunnelling through such a barrier at least for the normal incidence[25].

1.1.2 Graphene grown on transition metal surfaces

Free-standing exfoliated graphene presents ideal electronic properties resulting essentially undoped[18,26]. However, the softness of exfoliated graphene with associated flexural modes, the lack of long-range structural order and the size of the graphene flakes ($\approx$ 20 μm) hinder the measurement of the band dispersion with standard techniques, like angular resolved photoemission.

For traditional photoemission experiments, supported graphene is a more

suitable sample. The interaction of graphene sheet with a substrate freezes the flexural modes, but it can leave the presence of ripples, characteristics of free-standing graphene, whose morphology can be controlled by the choice of appropriate substrates.

Monolayer graphene can be grown epitaxially on silicon carbide (SiC) and other carbides, as well as on transition metals. Graphene on SiC is produced by vacuum graphitization[27], that consists in a high temperature annealing of SiC that leads to the evaporation of silicon and the formation of layers of graphite whose thickness can be controlled with high precision[28]. Transport properties of these samples reveal the Dirac nature of the charge carriers of the graphene layer[29]. However, the first graphene layer, at the interface with the substrate, results to be highly interacting with SiC, showing no π band by angle-resolved photoemission experiments, but it can act as a buffer layer for the subsequent graphene layer, which, instead, is a good approximation of the free-standing one. A residual n-doping is still present, testified by the Dirac point in valence band at 0.5 eV of binding energy[30]. Some differences are present for graphene grown on the Si- or the C- terminated face of SiC[31].

Another way to obtain high quality graphene is the epitaxial growth on transition metal surfaces by decomposition of hydrocarbons. This technique will be discussed in detail in Section (2.5). First evidence of the creation of a graphene layer was found accidentally on platinum and ruthenium in the 1960s[32,33]. While annealing the sample to high temperatures, carbon impurities segregated from the bulk to the surface, but it was seen merely as a surface reconstruction and no detailed investigation was made of these primordial graphene. Who knows what would ever be the present if graphene would have been discovered 40 years before... Now the interest in graphene adsorbed on metal surfaces is renewed.

Hexagonally close-packed surfaces of transition metal are chosen as substrate, where perfectly ordered epitaxial graphene overlayers have been obtained[34]. Depending on the metal, the nature of the interaction with graphene is different In particular, in going from 5*d* (Pt, Ir) to 4*d* (Rh, Ru) and to 3*d* (Ni), the hybridization between π band of carbon atoms and *d* shell becomes higher, due to the reduction of the *d* band occupancy. This is reflected in the electronic properties of the system, which show a continuous trend from almost free-standing graphene (on Pt and Ir) to highly hybridized on Ru and Ni. The degree of in-

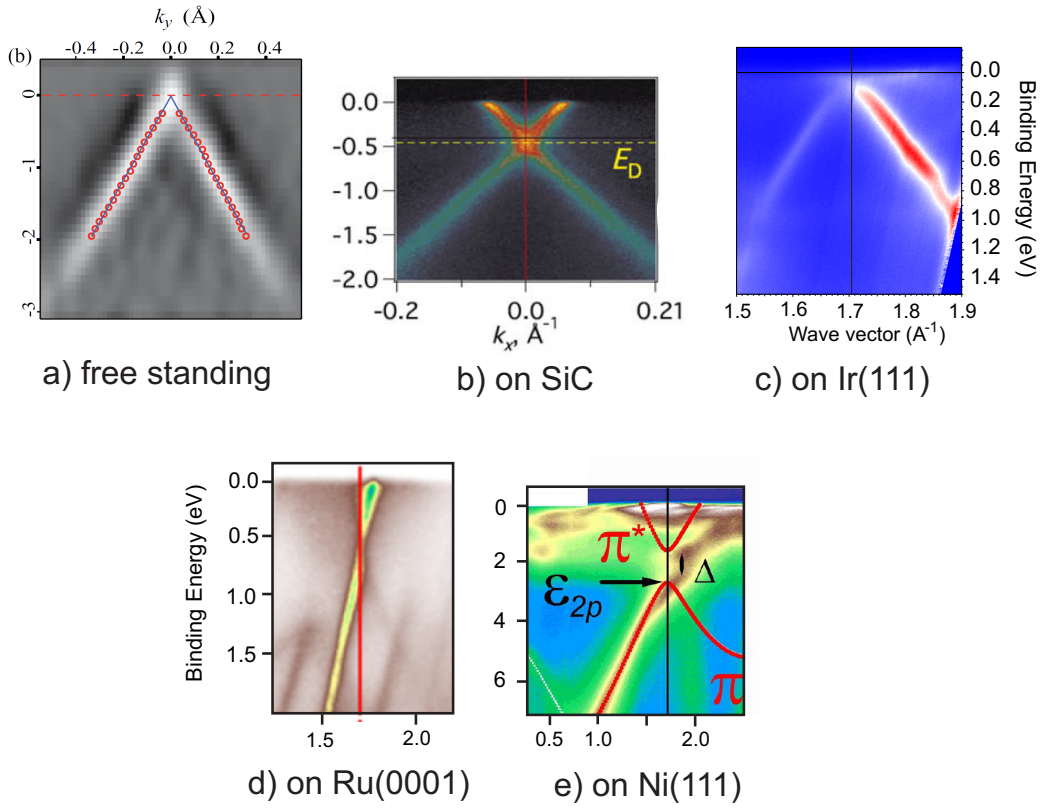

Figure 1.5: Dirac cones for different graphene's preparations: a) free-standing exfoliated[26] b) on SiC[35] c) on Ir(111) [II] d) on Ru(0001)[36] e) on Ni(111)[37]

teraction can be monitored, with Angular Resolved PhotoEmission Spectroscopy (ARPES), by the shift of the Dirac point with respect to the Fermi level, in particular the Dirac cone moves towards higher binding energy, sign of charge transfer from the metallic substrate. The interaction between epitaxial graphene and the substrate can distort the Dirac cone, shifting the corners away from the Fermi level and influencing the quasi-particle dynamics. ARPES is the fundamental experimental method used to probe the electronic structure of two-dimensional systems, and in particular to single out the basic parameters identifying graphene electronic structure (Dirac cone, Fermi velocity, doping, possible gap opening, etc.).

As an example we report in Fig. (1.5) a series of Dirac cones for free standing exfoliated graphene and graphene grown on different surfaces, measured by photoemission. For free standing exfoliated graphene the Dirac cone corner lies

close to the Fermi level (within 25 meV)[26], while for supported graphene the interaction with the underlying substrate can cause strong hybridization as the case of graphene on Ru(0001) and Ni(111) where the Dirac cone is shifted towards higher binding energies, down in the valence band. In the case of Ru(0001), in Fig. (1.5 d), we report the second layer of graphene, as the first one acts as a buffer layer, with strong hybridization and with the apex of the π-band at the K point down to $\approx$ 4 eV of binding energy[36,38,39]. The Dirac cone for graphene grown on Ir(111), because of the slight interaction, presents a small p-like doping[40], as measured by our group ^{II} and reported in Fig. (1.5 c).

Together with photoemission, X-ray Absorption Spectroscopy (XAS) is an useful technique to monitor the graphene interaction with the metallic surface. In Fig. (1.6) we report a serie of carbon K-edge spectra from graphite and graphene adsorbed on several TM surfaces. Graphene on Pt(111) and Ir(111) spectra though presenting the same main structures of graphite (peaks A, B and C) have some differences (A' and A"), see Section (3.2) for a detailed description. These differences become more evident while increasing the interaction with the substrate, manifested by the comparison of features in gap regions and broadening of the sharp graphene resonances[41,42].

The most important characteristic that makes graphene on TM surface different and, in some cases, more appealing than graphene on SiC is the natural and regular corrugation (moiré superstructures) which can be exploited to use graphene as a template to adsorb regular one-dimensional and bi-dimensional architectures. This pattern is visible both with LEED and STM technique, as reported for example in Fig. (1.7) for the case of graphene grown on ruthenium[34,43,44].

The multitude of spots with hexagonal symmetry in the diffraction pattern, showed in Fig. (1.7 d), is a sign of a long-range ordered superstructure: this highly-

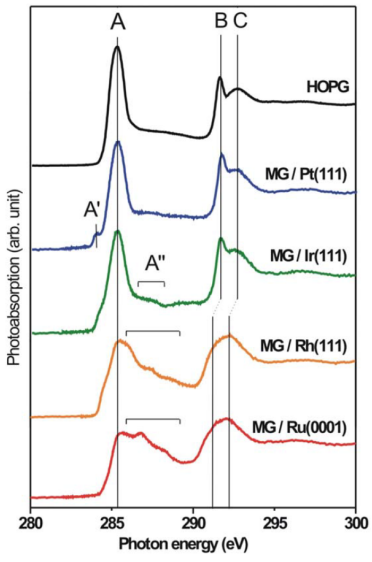

Figure 1.6: X-ray absorption spectra across the C 1*s* edge from graphite (HOPG) and graphene (MG) on several TM surfaces[41].

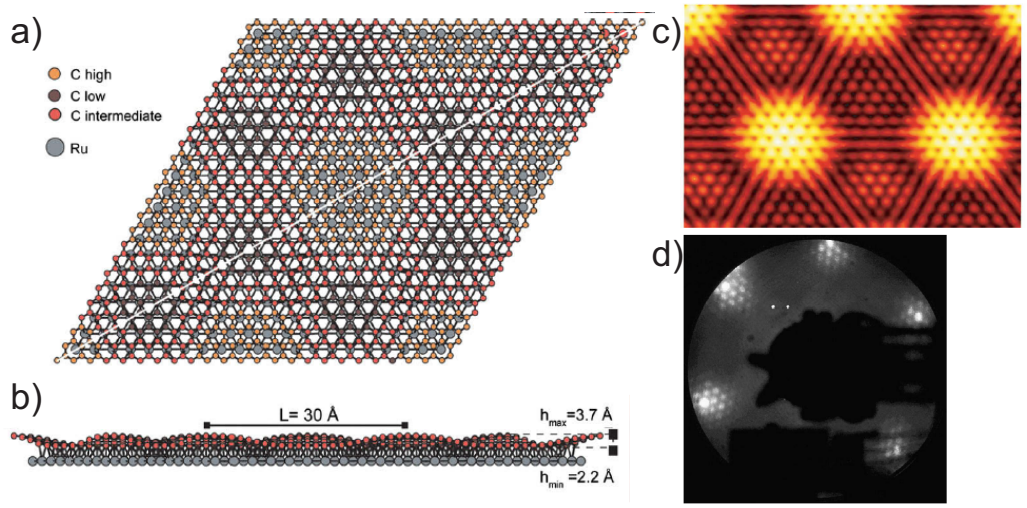

Figure 1.7: a,b,c) Relaxed model of the moiré structure of graphene on Ru(0001), obtained by a DFT calculation of a (12×12) graphene on (11×11) Ru structure. a) Top view of four unit cells of the moiré structure, 60 Å× 52Å. For clarity only one layer of Ru atoms is shown. b) Side view, showing the buckling of the graphene layer. The minimum spacing between the graphene and the metal surface is indicated. c) Computed STM image using the Tersoff-Hamann approximation[34,44]. d) LEED pattern of graphene/Ru(0001)[34,43].

ordered hexagonal modulated moiré is generated by the slight lattice mismatch between graphene and the underlying metal surface lattice.

For graphene, the lattice constant is assumed to be 2.46 Å , as for bulk graphite. The lattice constants of the hexagonally close-packed metal surfaces are reported in Tab. (1.1), together with the periodicity of the derived moiré pattern.

Graphene on Ni(111) is an exception because the lattice mismatch is so small that a (1×1) structure is formed. Graphene on Pt(111) is the most weakly bounded, in fact the substrate cannot force the overlayer to go in register with it and different moiré phases are present with different lattice constant and orientation with respect to the Pt surface[42,45]. While on Ir and Ru graphene forms a coherent corrugated domain that covers even the metal terraces without breaking[39,46,47].

Recent theoretical and experimental data have shown that the observed buckling is not only an electronic effect in the STM image, but it reflects a real height corrugation, with a modulation of $\approx$ 1.5 Å [48]. This spatial corrugation is also

	Pt(111)	Ir(111)	Rh(111)	Ru(0001)	Ni(111)
Lattice const.	2.77 Å	2.72 Å	2.69 Å	2.71 Å	2.49 Å
C/TM moiré	several	26 Å	29 Å	30 Å	no moiré

Table 1.1: Lattice constant of some hexagonally close-packed metal surface where graphene is usually grown. Eventual lattice constant of the moiré superstructure is also reported.

reflected in a chemical corrugation: carbon atoms in the valley regions will be more affected by the interaction with the underlying metal surface with respect to carbon atoms in the hills. If the interaction is strong (as for graphene on Ru and Rh) this causes a splitting of the C 1*s* core level spectra, due to the actual different chemical environment of the C atoms[41]. For graphene on Ir(111), the moiré corrugation is much smaller, of the order of 0.4 Å compared to 1.5 Å for graphene on Ru(0001). Furthermore, the variation in charge transfer over the moiré on Ir(111) is also roughly one tenth of that of graphene on Ru(0001)[49,50], thus, the higher the interaction the higher both the corrugation and the modification in the electronic properties (shifting of the Dirac cone, new features in XAS spectra).

Epitaxial growth of graphene on transition metal surfaces provides a viable method to test the effects of variable interaction strength on the graphene properties. While the extreme uniformity of some of the moiré structures can make these systems perfect templates for nanostructures, as we will see in the following Chapters.

1.1.3 From dream to reality

The unique combination of properties of graphene, which are not seen together anywhere else (like conductivity and transparency, mechanical strength and elasticity) makes this new material as much promising as one could possibly hope for. However, only recently graphene has been spotted in our world and now it is still the time to further expand the knowledge about its properties before obtain concrete applications. As Geim himself said "At the moment it's a dream, but it's a good dream - and in 20 years from now, who knows, graphene may replace silicon." More than a decade of research on carbon nanotubes (essentially rolled-up graphene) has already led to many applications.

Recently, the first measurements of graphene's mechanical and thermal properties were reported: it exhibits a Young's modulus of ∼1.0 TPa and a breaking strength of ∼40 N/m, reaching the theoretical limit[51].

Thermal conductivity is a fundamental parameter for electronic and optoelectronic devices, since their reliability and speed strongly depend on temperature. Materials with very high thermal conductivities are required to spread the heat generated locally in such devices[52,53]. Bulk copper, which is widely used as heat spreader in computers, has a thermal conductivity of ∼ 400 W/m·K at room temperature, but copper thin films, used as electrical interconnects, can have lower thermal conductivity (below 250 W/m·K)[54]. Graphene in contact with silicon dioxide, has a thermal conductivity of ∼ 600 W/m·K[55], higher than copper, even if reduced from the record values (∼ 5000 W/m·K[56] of suspended graphene, about 2.5 times as large as that of diamond, which has the highest thermal conductivity among natural materials. Pure-carbon materials (diamond, graphite, and carbon nanotubes) have very high thermal conductivities because the strong covalent bonding between carbon atoms results in a large phonon contribution (lattice vibration) to the thermal conductivity.

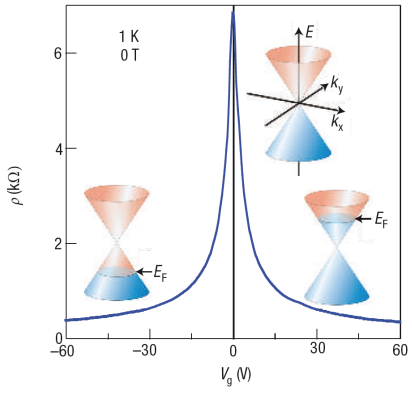

Figure 1.8: Ambipolar electric field effect in single-layer graphene. The insets show its conical low-energy spectrum $E(k)$, indicating changes in the position of the Fermi energy E_F with changing gate voltage V_g.[57].

The pronounced ambipolar electric field effect (Fig. 1.8) exhibited by graphene was surely its launching pad for applications in electronic devices. Charge carriers can be tuned continuously between electrons and holes in concentrations as high as 10^{13} cm^{-2} and their mobilities μ can exceed 15000 cm^2/V·s even under ambient conditions[1,58]. Positive (negative) V_g induce electrons (holes) in concentrations $n = \alpha V_g$ where the coefficient $\alpha \approx 7.2 \times 10^{10}$ cm^{-2} V^{-1} for field-effect devices with a 300 nm SiO_2 layer used as a dielectric. The rapid decrease in resistivity ρ on adding charge carriers indicates their high mobility and does not noticeably change with increasing temperature to 300 K[57].

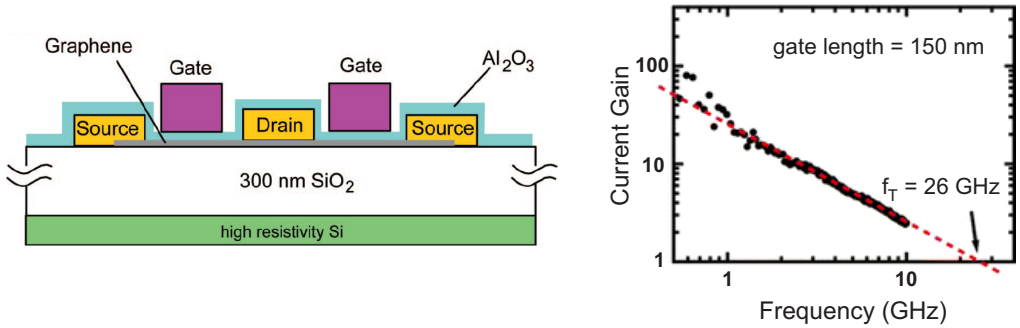

Figure 1.9: Left: schematic cross section of the graphene transistor. Right: measured current gain as a function of frequency. The dashed line correspond to ideal $1/f$ dependence for the gain[60].

Graphene offers a possibility to extend traditional transistor's operational range into terahertz frequencies, basing on the room temperature ballistic transport such that the charge transit between source and drain contacts takes only 0.1 ps for a typical channel length of 100 nm. Gate electrodes can be placed as close as several nanometers above graphene, which allows shorter channels and even quicker transit[59] making the reaching of terahertz range possible[60].

Band gap engineering efforts are going to overcome the Klein paradox which ensures a minimum conductivity for graphene (of the order of $4e^2/h$) even within the limit of nominally zero carrier concentration, thus the graphene's gapless spectrum leads to low on-off ratios for transistors.

IBM and Samsung are already using it in numerous electrical devices, the first fruitful born by IBM is a transistor, which uses graphene to achieve the record-setting speed of 100 GHz[60], as shown in Fig. (1.9).

As we have seen, efforts in realizing concrete applications are rising, a proof is the spread of graphene factories for large scale commercial production*. We reported only a few examples of possible applications, other important fields where concrete results have been reached are spintronics[61] and chemical sensing[62], graphene, being surface without bulk, can detect a single foreign molecule attached to it.

*www.grapheneindustries.com

1.2 Molecular electronics: more Moore

Since conventional inorganic semiconductors are fabricated by an optical technique, the lithography, the spatial resolution limit is determined by the wavelength of the light that is used, typically ultraviolet of hundreds of nanometers, that does not allow the control of the electronic properties at the nanoscale. Research and technological upgrades are developing even within this "conventional" field, improving the resolution by using light of always shorter wavelength, till the new EUVL (*Extreme Ultra-Violet Lithography*) technique developed at ASML[63] which make use of a 13.5 nm light to print circuits by exploiting different types of sources: synchrotron radiation, discharge-produced plasma, laser-produced plasma or EUV tubes (X-ray tubes optimized to emit EUV radiation)[64].

Together with graphene, another competitor, or better a supplement, of traditional inorganic semiconductors technology dominated by the Si/SiO_2 metal-oxide semiconductor field-effect transistor (MOSFET), is the organic electronics. In the last decades this fields developed rapidly and now organic devices are present in every day life (in touch-screens, for example). One of the reasons at the basis of the development of organic electronics is the continuous need and challenge of miniaturization, in order to maintain the trend described by the "Moore's Law", such as to double the areal density of transistors on integrated circuits every two years[65].

Driven by both the technological potential and by the interest from a fundamental point of view to understand the properties of these low-dimensional systems capable of efficiently transporting charge and interact with light, research in organic semiconductors arose[66]. Furthermore, other advantages of the organic systems which have made them the protagonist of the new "plastic electronics" are the capability to tailor their physical and electronic properties via synthetic methods (i.e. by changing the functional groups or some specific atoms within a molecule), the easy way of fabrication via vapor/solution phase and their capability of spontaneous self-assembly. This trend is driven by the demand for inexpensive, large-area, flexible devices processed at far lower substrate temperatures than Si chips.

Organic semiconductors are based on the π-conjugation properties of small molecules and polymers. In order to be utilised in a device, the charge transport

mechanism is of crucial importance. While for crystalline inorganic semiconductors the charge carriers are delocalized giving rise to the band structure of the solid and the transport mechanism occurs through the band transport from the highest occupied band (*valence band*) to the lowest unoccupied band (*conduction band*), the transport in organic materials is not fully understood[67]. Being the energy levels in molecules essentially localized, transport occurs via a hopping mechanism between overlapping molecular orbitals[68], this is the principle of the π-conjugated systems. These systems are characterized by the presence of *p*-orbitals on several neighbouring atoms capable of forming an extended system of π-orbitals. The overlapping between orbitals on the same molecule or adjacent molecules gives rise to occupied (bonding) and unoccupied (non bonding) orbitals, to which partially delocalized wave functions can be associated. The highest occupied molecular orbital (HOMO) and the lowest unoccupied molecular orbital (LUMO) are separated by an energy gap, typically in the 2-5 eV range[69,70].

In contrast to the covalent bonds of inorganic semiconductors, the solid-state structure of these kind of molecules and polymers is based on weak interactions (van der Waals, dipole-dipole) between neighbouring elements. This limits the mobility, values are found in the range 0.1-5 $cm^2/V{\cdot}s$ at room temperature, lower than 10^3 $cm^2/V{\cdot}s$ in monocrystalline silicon, but relatively high dealing with molecules. However, when organic molecules are assembled as regular arrays, conduction may also takes place via band formation, reaching higher value of conductivity[71].

Apart from the conduction mechanism, the charge injection into the organic material is also of crucial importance for the performance of the device. It strongly depends on the interface between the molecules and the substrate. The electronic hybridization with the supporting substrate perturbs the intermolecular interaction and determines the electronic structure of the molecular layer and the interaction with the substrate.

Within the category of the π-conjugated systems, the most commonly used classes of molecules are polyacenes (pentacene, above all), oligothiophenes, and phthalocyanines, schematized in Fig. (1.10) and (1.11). These materials present hetero-atomic or homo-atomic rings within which charge is largely delocalized and they are all characterized by a planar structure. We will concentrate here on

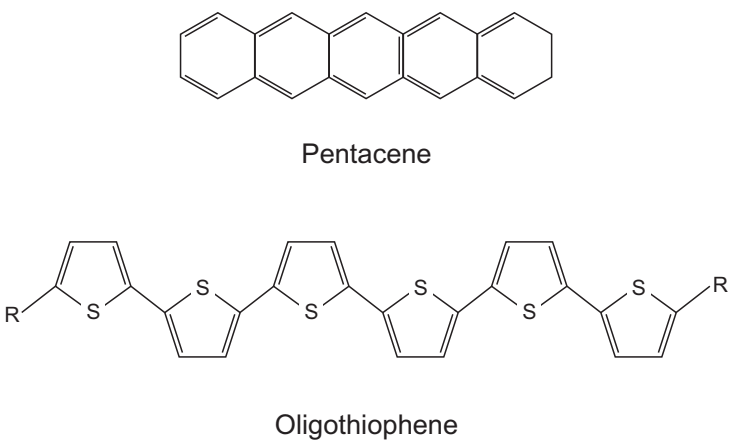

Figure 1.10: An example of a polyacene (pentacene) and a typical oligothiophene chain: the choice of the functional group R acts on the physical and chemical properties of the molecular assembly. If the R groups are not present, the molecule is the simple sexithiophene.

phthalocyanines, one of the subject of this thesis.

Phthalocyanines are one of the most stable organic materials largely used in a wide range of technological applications[72,73]. They are one of the most important class of colourants (as blue, cyan and green pigments) and dyes[74], their chemical sensing properties are used in the chemically sensitive field-effect transistors[75], and they found applications also in medicine[76]. Concerning their semiconducting and optoelectronic properties phthalocynines are widely used as organic light-emitting diodes[77], organic field-effect transistor[78], and together with fullerene are utilised in photovoltaic cells[79].

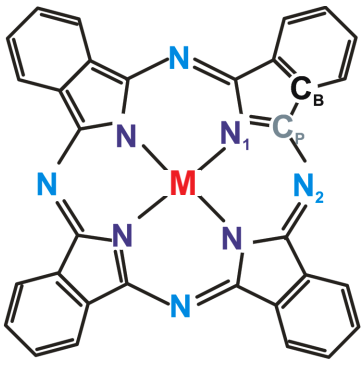

Figure 1.11: Sketch of a metal-phthalocyanine molecule

In particular metal-phthalocyanines (MPcs, M-$C_{32}H_{16}N_8$), in Fig. (1.11), are planar molecules characterized by a square shaped organic ring, containing 4 pyrrole rings (C_4H_5N) and 4 benzene rings (C_6H_6) which bind a central metallic ion. Two different species of nitrogen and carbon atom are present in a MPc molecules, depending on the different environment surrounding each atom: in Fig. (1.11) are marked C_B and C_P, the carbon atoms in the benzene and pyrrole ring, respectively, while N_1 and N_2 are the two non-equivalent

nitrogen atoms (N_1-isoindole and N_2-azomethine) in the pyrrole rings and in the bridge position.

About 70 different elemental ions can be placed in the central cavity of a Pc molecule[80] and its choice can strongly influence the physical properties. The possibility of tailoring its properties by changing the central atom makes these molecules a prototype to understand the behaviour of low-dimensional organic systems.

When the central site is occupied by a transition metal (TM) ion (Mn, Fe, Co, Cu....), MPcs become appealing not only for their π-conjugation but also for the interesting magnetic properties as low temperature ferromagnetic condensed phase[81] and site specific Kondo effect at room temperature[82], widening the field of application to magnetic switches[83] and spintronic devices[84]. By a fundamental point of view, the electronic and spin ground state of the incorporated transition metal ion, being affected by the interaction with the organic ligand[85], gives rise to molecular orbitals with a partial metallic character whose exact sequence of the occupied and unoccupied orbitals is still under debate. The understanding of the interaction between organic molecules and solid surfaces is then an important parameter for many technological applications.

1.3 State of the art

Metal-phthalocyanines are known to self-assemble into ordered 1D or 2D architectures on suitable substrates, their flat shape allows a direct interaction of the central metal atom with the supporting substrate, while the organic ligand ensures a robust and reproducible ordering of the molecular nanostructures. They act as building blocks for nanometer-sized electronic devices, exploiting the transport properties of π-conjugation of the macrocycle electrons.

A delicate balance between molecule-substrate and molecule-molecule interactions governs the specific formation of such patterns, in particular, in presence of reconstructed or nano-patterned surfaces, the molecule-substrate interaction is driven by both the substrate surface reconstruction, which enables the formation of long-range ordered molecular structures, and by the possible electronic interaction. If the substrate does not present a nano-patterned structure, the inter-molecular interactions induce the formation of closely packed molecular

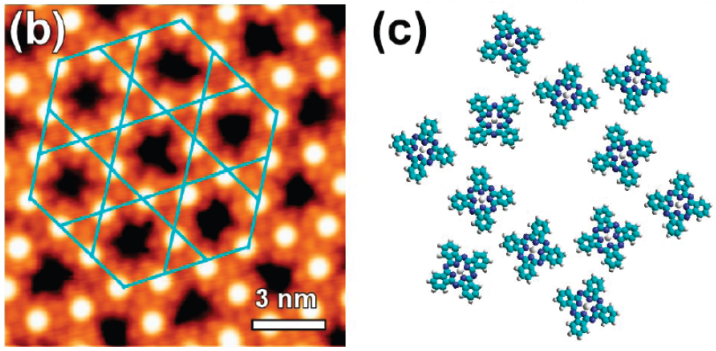

Figure 1.12: b) STM image of SL-FePc supramolecolar Kagome lattice on moiré pattern of graphene/Ru(0001). c) Structural model of the Kagome lattice[93].

single layers. Photoemission experiments of MPcs assembled on metallic substrates suggest a mixing of the 3*d* open shell MPc central metal atom with the underlying metallic states[86–89].

By using phthalocyanines with a central magnetic atom, its spin can form an ordered magnetic network, encaged by the organic macrocycle which acts also for anchoring the magnetic ion to the surface in a self organized structure, thus avoid the typical clustering of metals[90]. The large number of parameters regulating the interaction of molecular adsorbate with surfaces makes it challenging to study and develop methods to control these system.

Due to the promising properties of graphene and the already effective applications of metal-organic molecules, combining these field is highly attractive for both the protagonists. The strong coupling between molecules and metal surfaces often results in a modification of the intrinsic electronic properties of the molecules or even the quenching of its magnetic response. Furthermore, the electronic properties of graphene are sensitive to local perturbations, such as surface charges and adsorbed gas molecules[62,91]. The grafting of functional groups or organic molecules in a controllable way has been proposed as a feasible reproducible solution to control the carrier concentration and band gap at the Dirac point[92].

An important advantage in the molecular self-assembling process is given by graphene grown on transition metal surface: the moiré pattern generated by the slight lattice mismatch between the carbon layer and the underlying metal offers an unique template for molecular nanoarchitectures. Iron-phthalocyanine

molecules self-assemble on the moiré pattern of a graphene sheet grown on the Ru(0001) surface, forming an ordered superstructure (Kagome lattice) matching the underlying superlattice[93], as reported in Fig. (1.12). After this first experiment in 2009, other works have studied the interaction of MPcs with epitaxial graphene on Ru(0001) and Pt(111)[94–96] by STM or on graphene/Ni(111)[97]. Differences in the absorption geometry arise, depending on the central metal atom of the MPc molecule.

However, STM experiments alone cannot investigate the nature of the interaction. Furthermore, graphene grown on ruthenium is highly interacting, as reflected in the strong modified electronic structure of graphene and a marked corrugation. Graphene on platinum, on the opposite, due to the very week hybridization with the substrate does not present a well defined moiré superstructure. An optimum compromise between corrugation and interaction is given by the graphene/Ir(111) system.

By studying the adsorption of different transition metal-phthalocyanines (TM = Fe, Co, Cu) on epitaxial graphene grown on Ir(111) we aim to:

- grow and characterize the graphene layer on Ir(111) surface by controlling the graphene-substrate interaction;
- study the growth morphology of MPcs single layers on the nano-patterned moiré superstructure;
- characterize and control the electronic and related magnetic properties of MPcs single layers changing the central metal atom of the molecule;
- investigate the adsorption mechanism of the MPcs molecules through the interaction strength between molecule and substrate.

The very low concentration of surface adsorbed molecules and the intrinsic surface nature of graphene, narrow the field to very high surface-sensible investigation techniques. Ultra-violet photoemission spectroscopy and low energy electron diffraction are valid tools in surface science to get information on the density of filled states of surface adsorbed species and on the structural configuration. The availability of high intensity synchrotron radiation facilities allows the investigation of unfilled states through X-ray absorption, while X-ray magnetic circular

dichroism can give quantitative information on the magnetization of surface supported nanostructures. Finally, temperature programmed experiments can give important information on their adsorption energy.

Chapter 2

Experimental techniques and apparatus

This Chapter is devoted to the experimental techniques and to the description of the experimental apparatus used for the characterization of the systems subject of this work. An important part of the measurements has been taken during synchrotron beamtimes, so a brief description of the synchrotron facilities and beamlines is provided, in particular the ID08 beamline of the European Synchrotron Radiation Facility (ESRF) in Grenoble and the SuperESCA beamline of ELETTRA in Trieste.

Complementary techniques have been used to investigate the nature of the interaction in the materials involved, from an electronic and structural point of view. X-ray absorption, photoemission with both UV and X-ray photons and low-energy electron diffraction (LEED) were intensively used. Angular-resolved photoemission spectroscopy, in particular, is a fundamental method used to probe the electronic structure of two-dimensional systems. Furthermore, temperature-programmed experiments have revealed to be a powerful tool to investigate the strength of the interaction. Preliminary investigation of the magnetic properties through X-ray magnetic circular dichroism (XMCD) is presented in the Appendix, at the end of the Thesis.

In order to avoid surface contamination, a high control of the sample environment in which experiments are performed is required. Standard equipments employed in surface physics are thus endowed with pumping systems able to en-

sure ultra high vacuum (UHV) conditions, down to pressures in the low 10^{-10} mbar range. They generally consist in two distinct chambers: a preparation chamber where the sample is cleaned and the molecular film deposited, and a measurement chamber, where sample characterization operations take place. The basic physical mechanisms underlying each technique will be discussed, focusing the attention on the relevant information which may be extracted from the data analysis.

An essential part of this work was devoted to design, set up, and progressively improve the LoTUS (Low Temperature Ultra-violet Spectroscopy) experimental apparatus in Rome, in order to achieve the experimental realization *in situ* of graphene.

2.1 Synchrotron radiation

Synchrotron radiation occurs when a charge moving at relativistic speed follows a curved trajectory. It was theoretically calculated by Ivanenko and Pomeranchuk in the Soviet Union in 1944 (theoretical work then started even in the U.S., obviously independently) and it was first considered as a waste product, limiting the energy obtainable in storage rings used for high-energy physics (the first betatrons, magnetic-induction electron accelerators). Synchrotron radiation was directly observed, literally, since it was visible light that was seen, in 1947 at the General Electric Research Laboratory in Schenectady (New York), by chance, and then characterized. However the first access to the radiation for an experimental program occurs only in 1961 and until 80's the accesses were limited and parasite to high-energy physics dedicated facilities. Due to the high potentiality of synchrotron radiation demonstrated during years, in the 80's a second generation of synchrotron facilities was started to be built, whose storage rings were designed and dedicated to the production of synchrotron radiation as a very important research tool for investigating the matter in a multidisciplinary field.

The European Synchrotron Radiation Facility (ESRF) in Grenoble with a 6 GeV storage ring and ELETTRA in Trieste, 2 GeV, are the two facilities where most of the data of this Thesis were taken. They belong to the third generation of storage rings, operating since the first half of '90s. Third generation synchrotrons are optimized for brightness, with long straight sections for insertion devices that

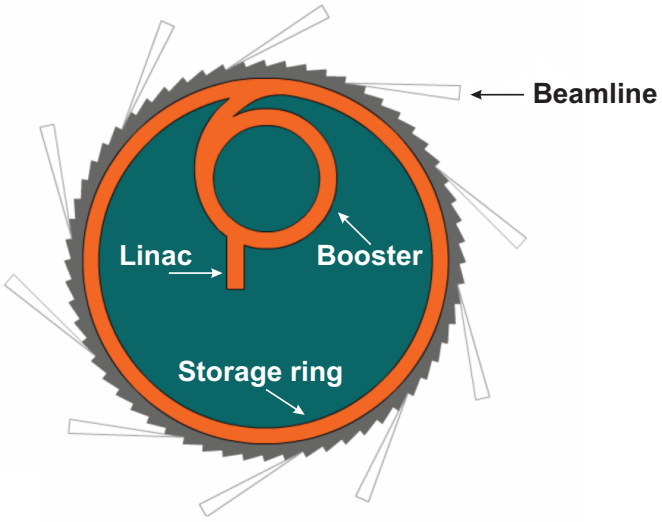

Figure 2.1: Schema of a synchrotron radiation light source.

permit achieving even higher brightness and a considerable degree of spatial coherence.

Generally, a synchrotron facility consists of a linear accelerator (LINAC) used as a pre-injector, a cyclic accelerator (booster), where particles are accelerated to relativistic speed, used as an injector, and a storage ring where the circulating particles are kept at the operating energy, as schematically pictured in Fig. (2.1). The storage ring is made by straight sections and arcs. The bending magnets form the curved sections were the source of radiation delivered to the beamlines in the second generation synchrotrons. The radiation with high spectral flux and brilliance in a wide range of energies produced by the third generation synchrotron light sources is due to the insertion devices inserted in the straight sections of the storage ring, namely undulators and wigglers.

In the present work the synchrotron facility is mainly regarded as a source of polarized light of continuum spectrum. This allows XAS measurements, where a tunable photon source is necessary and high-resolution PES measurements since the energy of the photons can be chosen according to different cross-sections for specific core levels.

SuperESCA @Elettra

SuperESCA was the first beamline operating at Elettra since 1993, it is primarily designed for soft X-ray photoemission experiments on surfaces. In order to achieve high energy resolution keeping at the same time a high photon flux, the light produced by the insertion device is collected and focused into the monochromator, the dispersed light coming out is finally re-focused on the sample in the experimental chamber. The photon energy is tunable in the range 90-1800 eV, with the maximum of the monochromator resolving power ($E/\Delta E \sim 10^4$) at 400 eV and a photon flux of $\sim 10^{12}$ photon/s[98].

As in general all the UHV chambers, the SuperESCA end-station consists of two UHV chambers separated by a gate valve: a preparation chamber, designed for sample preparation, and a main chamber, made of μ-metal for optimum shielding, avoiding the influence of magnetic fields that could distort the experimental results. It is equipped with a 150 mm hemispherical electron energy analyser.

ID08 @ESRF

ID08 is an intense source of polarized soft x-rays that is principally used to probe magnetism in a diverse range of systems with x-ray magneto-optical techniques and to study the electronic structure of materials using x-ray and photoelectron emission techniques. The photon energy is tunable in the range 400-1500 eV, with the maximum of the monochromator resolving power ($E/\Delta E \sim 10^3$) at 850 eV[99], making it ideal for studying the magnetic and electronic properties of transition metals and rare earths. The helical undulator provides a 100% circular/linear beam polarization. The low temperature superconducting magnet allows application of x-ray magnetic circular dichroism (XMCD) technique to many different aspects of new magnetic phenomena (magnetism at the nanoscale, interface spin polarization, isolated atoms on surfaces). The magnetic field can be swept from $+5$ T to -5 T in the direction of the x-rays beam. The minumum temperature on the sample is around 7 K.

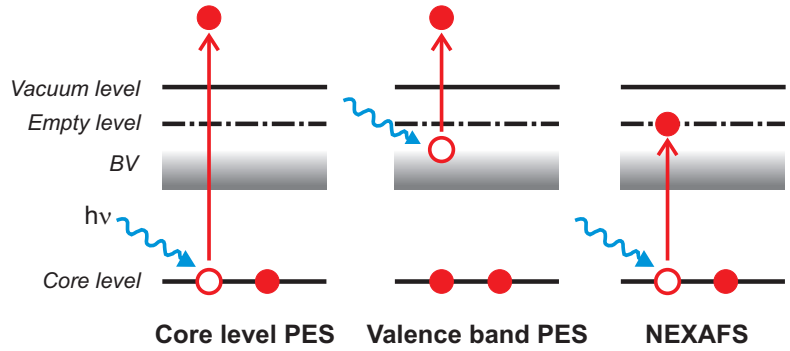

Figure 2.2: A schematic view of the spectroscopic techniques utilised in this work. Left and central panel represent the photoemission from a core level and from valence band, respectively, to the continuum. Right panel represent the near edge absorption given by the transition of a core electron to an empty bound level of the system.

2.2 Spectroscopic techniques

Spectroscopy in general is the study of the effects of the interaction of electromagnetic radiation (probe) with matter (target). It includes a variety of techniques that provide complementary information about physical and chemical properties of the matter, as its geometrical and electronical structure. The techniques utilised in this work are presented in a schematic one-electron picture in Fig. (2.2): photoelectron spectroscopy (with X-ray and UV photons) and X-ray absorption spectroscopy, more detailed description will follow in the next sections.

Due to the small penetration depth of electrons in the range of 10 to 1000 eV (see the universal curve in Fig. (2.3)) these techniques are extremely surface sensitive and thus effective to investigate the electronic properties of very thin layer of adsorbate.

All of the above mentioned spectroscopic techniques are described in the framework of the modelization of the radiation-matter interaction: the probability of transitions P_{if} and their related intensities are provided by the Fermi's golden rule

$$P_{if} \propto \sum_f | < f|\widehat{H}_{int}|i > |^2 \delta(E_f - E_i - h\nu) \qquad (2.1)$$

The transition rate depends on the strength of the coupling between the

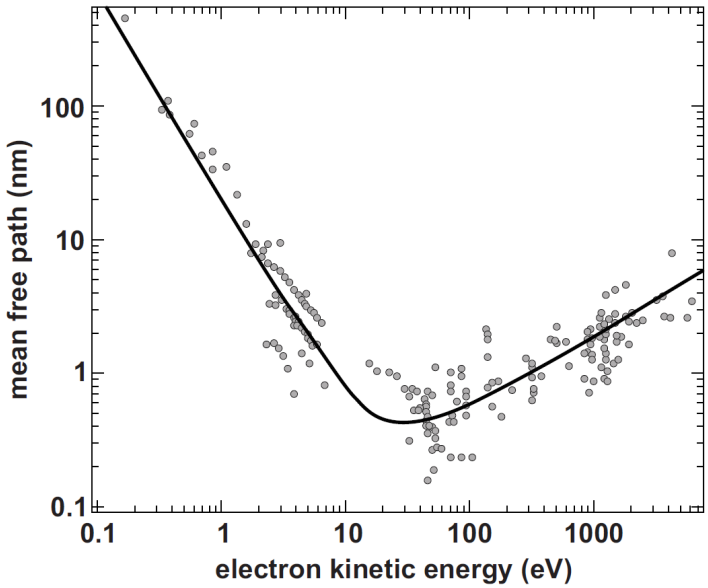

Figure 2.3: Universal curve: electron mean free path as a function of the kinetic energy for different materials[100].

initial state and final state of the system and the density of the final state. The delta function gives the condition of conservation of the energy (the final state must be equal to the difference between the photon energy $h\nu$ and the initial state energy). E_i (E_f) is the energy of the multi-electron system in the initial (final) state $|i>$ ($|f>$): as shown in Fig. (2.2), the final states are different for the spectroscopic techniques used in this thesis. A photoemission process can takes place either from a core level or from the valence band of the system; the final state can be described by the free photoelectron and the remaining ionized atom or molecule. In the photoabsorption the excitation takes place from a core level to a free bound state of the system, the final state is then an overall neutral atom or molecule with an excited electron.

$\widehat{H}_{int}$ is the interaction operator between the electron and the photon and, within the semi-classical approximation, is given by

$$\widehat{H}_{int} = \frac{e}{mc}\mathbf{A}\cdot\mathbf{p}, \tag{2.2}$$

where only the linear term in the perturbation field is considered.

Within the dipole approximation (the wavelength of the light used for a one-

electron excitation has to be much larger than the radius of the atomic or molecular excited shell, hence $\exp i\mathbf{k}\cdot\mathbf{r} \approx 1$, valid in the energy range of soft X-rays) and the one-electron assumption (that allows to write the initial state as a core wavefunction and the final state as a free electron wavefunction, not considering all the other electrons in the transition process), the absorption cross section σ, defined as the probability amplitude between initial and final state, P_{if} (Eq. (2.1)) divided by the incident photon flux I_0, becomes:

$$\sigma = \frac{4\pi^2\hbar^2}{m^2}\frac{e^2}{\hbar c}\frac{1}{\hbar\omega} \mid< f \mid \mathbf{e}\cdot\mathbf{p} \mid i >\mid^2 \rho_f(E)\delta(E_f - E_i - h\nu), \tag{2.3}$$

where $\rho_f(E)$ is the density of unoccupied final states.

2.2.1 Photoelectron spectroscopy

In PES when photons with sufficiently high energy hit a sample, electrons (called photoelectrons) are ejected from the sample. This process is called photoelectric effect, described by Albert Einstein in 1905[101]. The conservation of energy implies that by knowing the monochromatic photon energy ($h\nu$) and by measuring the kinetic energy of the photoemitted electron (E_{kin}) the binding energy (E_B) of the electron can be calculated by

$$E_B = h\nu - E_{kin} - \phi, \tag{2.4}$$

where ϕ is the work function (the energy difference between the vacuum level and the Fermi level).

Depending on the photon energy, different kinds of initial electronic states can be probed. In particular when using ultra-violet photons (5-100 eV), electrons from the valence bands are sorted and if the polar angle is resolved, the technique is called Angular Resolved PhotoEmission Spectroscopy (ARPES), very important for the investigation of the dispersion relation of the valence band electrons, allowing to study different symmetry directions along the Surface Brillouin Zone. Instead, with X-ray photons (soft regime 100-1000 eV, or hard $>$ 1000 eV), one has access to many core levels; core level PES (or XPS) is a chemical specific technique since all elements in the periodic table have energetically well separated core levels, which will give distinct peaks in a core level PES spectrum. This

means that the energy position of a peak is element specific.

Three steps model

In the framework of the single particle picture, a typical approach is to decompose the photoemission current as the product of three independent contributions, three steps model:

1. the excitation of the electron due to the absorption of a photon with energy $h\nu$, from the initial state E_B to a final state $E_B+h\nu$;
2. the transmission of the electron through the bulk, towards the surface;
3. the emission of the electron from the surface.

1. Excitation

The first contribution holds all the information on the electronic structure of the material, since it is given by the sum over all transition probabilities (see Eq. (2.1)), weighted by the probability that the initial state is occupied and that final state is empty, through the Fermi distribution function. We obtain an expression for the photocurrent as follows:

$$I \propto \sum_{i,f} f(E_i)(1-f(E_f)) \mid M_{if} \mid^2 \delta(E_f-E_i-h\nu)\delta(E_{kin}-(E_f-\phi))\delta(\mathbf{k_f}-\mathbf{k_i}-\mathbf{G}), \tag{2.5}$$

where the matrix element M_{if} is the same of Eq. (2.1). The Dirac functions account for the three conservation laws of:

- the energy in the excitation process inside the crystal,
- the energy between the excited state and the free electron,
- the momentum.

2. Transmission

Not all the excited electrons reach the surface without suffering any collision which causes the lost of the electronic information (secondary electrons). To consider only the primary electrons, we define the coefficient $d(E_f, \mathbf{k})$ as

$$d(E_f, \mathbf{k}) \simeq \frac{\alpha\lambda}{1+\alpha\lambda} < 1, \tag{2.6}$$

where α is the optical absorption coefficient and λ the electron mean free path.

3. Emission

In the third step we have to consider the scattering of the photoelectron, due to the surface potential. The only electrons that can escape are those having a kinetic energy component perpendicular to the surface larger than the barrier $E_{vac} = E_F + \phi$ (E_{vac} is the vacuum level, E_F the Fermi level and ϕ the work function). Since outside the crystal the electron can be described as a plane wave, we obtain that the momentum component perpendicular to the sample surface out of the sample must obey to the following relation:

$$k_\perp^{ext} = \frac{1}{\hbar}\sqrt{2mE_{kin}}\cos\theta, \tag{2.7}$$

where θ is the polar emission angle. Thus we can define a transmission coefficient $T(E_f, \mathbf{k})$:

$$T(E_f, \mathbf{k}) = \frac{1}{2}\sqrt{1 - \frac{E_F - \phi}{E_f}}\delta(\mathbf{k_i^{\parallel}} + \mathbf{G}^{\parallel} - \mathbf{k_{ext}^{\parallel}}), \tag{2.8}$$

this expression is valid if $E_f > E_F + \phi$ (otherwise is 0) and it is multiplied by a delta function which accounts for the conservation of the momentum component parallel to the surface, since there is no potential discontinuity in this direction.

The photoelectrons are then characterized by their kinetic energy E_{kin} and the polar emission angle θ. The quantity measured by the spectrometer is the current of photoemitted electrons $I(E_{kin}, \theta)$ which determines the energy distribution curve (EDC). As we have seen, the parallel momentum component is conserved during the process and can be expressed as

$$k^{\parallel} = \frac{1}{\hbar}\sqrt{2mE_{kin}}\sin\theta; \tag{2.9}$$

it is therefore possible to map the full band dispersion, by resolving the emission angle θ (ARPES).

Many-body representation

In the simple but effective model described so far all the interaction effects between electrons have been neglected. The final state of the system is in fact described by the emitted (free) photoelectron and the remaining N-1 electrons. According to the *Koopmans' theorem* the remaining electrons are frozen, with the same initial and final state. Within this model the binding energy of the photoelectron would be expressed by only one line in the PE spectrum at an energy E_B called Koopmans' energy, according to Eq. (2.4).

These effects can be classified into two contributions: extrinsic and intrinsic. The first is due to the interaction between the photoelectron and the remaining electrons, giving rise to the secondary electrons; the second concerns the interaction between the photohole created by the emitted photoelectron and the remaining electrons.

We want now to consider the intrinsic contribution, hence to write the final state wavefunction as the product of the wavefunction of the single electron and that of a system with N-1 electrons. In this way we consider the photoemission process as instantaneous (the so called *sudden approximation*), thus the photoelectron does not interact with other electrons during its emission through the surface. In this view the photoemission current becomes:

$$I \propto \sum_{if} \mid M_{if} \mid^2 \sum_{m} \mid m_{im} \mid^2 \delta(E_i^N + h\nu - E_m^{N-1} - E_{kin}), \tag{2.10}$$

where $M_{if} =< \Phi_i^{\mathbf{k}} \mid \widehat{H}_{int} \mid \Phi_f^{\mathbf{k}} >$ is the matrix elements between the single particle states and $m_{im} =< \Psi_m^{N-1} \mid \Psi_i^{N-1} >$ is the overlapping between the N-1 electrons states. This last term takes into account the relaxation of the system after the emission of the photoelectron, hence the many-body interaction with the photohole. The relaxation effects due to the reaction of the ionized system to the new potential of the core hole will affect the value of the binding energy of the photoemitted electron, in fact they are responsible of the shake-up or shake-off satellites in core level photoemission spectra: every non vanishing overlap in m_{im} will contribute to the photoemission spectra with structures at energy position corresponding to their eigenvalues (higher binding energies than the mainline). The shake-up can be regarded as a final state excitation when a

valence electron is excited to a bound state, whereas a shake-off transition is an excitation of a valence electron into a state above the vacuum level.

In the case of relaxation it is convenient to use the Green functions formalism to further describe the photoemission process. With the second quantization formalism, the N-1 particles wave function can be written as:

$$\mid \Psi_{i,m}^{N-1} >= \widehat{c_{\mathbf{k}}} \mid \Psi_{i,m}^{N} > \tag{2.11}$$

where $\widehat{c_{\mathbf{k}}}$ is the destruction operator of a $\mathbf{k}$ momentum electron. The single particle Green function are then written as:

$$G(\epsilon, \mathbf{k}) = \sum_m \frac{|< \Psi_m^{N-1} \mid \widehat{c_{\mathbf{k}}} \mid \Psi_i^N >|^2}{\epsilon - E_m^{N-1} + E_i^N - i\eta} + \sum_m \frac{|< \Psi_m^{N+1} \mid \widehat{c_{\mathbf{k}}}^\dagger \mid \Psi_i^N >|^2}{\epsilon - E_m^{N+1} + E_i^N + i\eta} \tag{2.12}$$

whit $\eta \to 0^+$. In the calculation of the photoemission current, is considered only the first term of Eq. (2.12), because the second term accounts for inverse photoemission.

Making use of the properties of Green functions, we can write the single particle spectral function:

$$\begin{aligned} A(\epsilon, \mathbf{k}) &= -\frac{1}{\pi} \Im[G(\epsilon, \mathbf{k})] \\ &= \sum_m |< \Psi_m^{N-1} \mid \widehat{c_{\mathbf{k}}} \mid \Psi_i^N >|^2 \, \delta(\epsilon + E_m^{N-1} - E_i^N). \end{aligned} \tag{2.13}$$

Comparing to Eq. (2.10), we can re-write the photoemission current in terms of the single particle spectral function as:

$$I \propto \sum_{if} \mid M_{if} \mid^2 A(E_f - h\nu, \mathbf{k}). \tag{2.14}$$

By defining the self-energy $\Sigma(\epsilon, \mathbf{k}) = \Sigma' + i\Sigma''$ the Green function and the spectral function can be written as:

$$\begin{aligned} G(\epsilon, \mathbf{k}) &= \frac{1}{\epsilon - E_{\mathbf{k}} - \Sigma(\epsilon, \mathbf{k})} \\ A(\epsilon, \mathbf{k}) &= -\frac{1}{\pi} \frac{\Sigma''(\epsilon, \mathbf{k})}{[\epsilon - E_{\mathbf{k}} - \Sigma'(\epsilon, \mathbf{k})]^2 + \Sigma''(\epsilon, \mathbf{k})}. \end{aligned} \tag{2.15}$$

The self-energy contains all the information on the many-body interaction of the system (all the intrinsic contributions) and characterizes the lineshape of the photoemission spectra. In particular, $\Sigma(\epsilon, \mathbf{k})$ can be viewed as a sum of different contributions due to electron-electron, electron-phonon, electron-impurity interaction:

$$\Sigma(\epsilon, \mathbf{k}) = \Sigma^{el-el}(\epsilon, \mathbf{k}) + \Sigma^{el-ph}(\epsilon, \mathbf{k}) + \Sigma^{el-imp}(\epsilon, \mathbf{k}) \tag{2.16}$$

When $\Sigma(\epsilon, \mathbf{k}) \simeq \Sigma(\mathbf{k})$, hence fixed energy and the curve is a moment distribution curve (MDC), the photoemission spectra is a Lorentzian curve centred in $E_{\mathbf{k}} + \Sigma'(\mathbf{k})$ and with a full width at half maximum (FWHM) $\Gamma(\mathbf{k}) = 2\Sigma''(\mathbf{k})$. Thus it can be deduced that the real part of the self-energy is linked to a shift of the binding energy measured, while the imaginary part to the life time of the initial state, and thus to the width of the photoemission peak. The real and imaginary part are connected by the Kramers-Krönig relations.

Electron-phonon interaction

The spectral function (Eq. 2.15) allows to study the electron-phonon interaction by considering the self-energy Σ^{el-ph} associated to this process. The electron-phonon coupling expresses the possibility that an electron occupies the photohole taking the energy and the momentum from the interaction with a phonon. In general this interaction depends on the density of phonon states, $F(\epsilon_i, \mathbf{k}, \epsilon')$, multiplied by a coupling constant with electrons, $\alpha(\hbar\omega)$, expressed as the Eliashberg function[102]:

$$\alpha^2(\hbar\omega)F(\epsilon_i, \mathbf{k}, \epsilon') = \sum_{\mathbf{q},\eta,f} \delta(\epsilon_i - \epsilon_f) \mid g^{if}(\mathbf{k}, \mathbf{q}, \eta) \mid^2 \delta(\epsilon' - \epsilon'_{\mathbf{q}}, \eta) \tag{2.17}$$

This equation represents the phonon DOS weighted by the matrix element $g^{if}(\mathbf{k}, \mathbf{q}, \eta)$ associated to the scattering of an electron, with wavevector $\mathbf{k}$ from the state *i* to *f* by a phonon (with wavevector $\mathbf{q}$ and energy ϵ', in the band η).

Within this formalism it is possible to write the imaginary part of the electron-

phonon self-energy as a function of energy and temperature[103]:

$$\Sigma''(\epsilon_i, \mathbf{k}, T) = \pi \int_0^{\hbar\omega_{max}} d\epsilon' \alpha^2(\hbar\omega) F(\epsilon')[1+f(\epsilon+\epsilon')-f(\epsilon-\epsilon')+2n(\epsilon')] \quad (2.18)$$

The mass enhancement parameter λ is an effective parameter resuming this complex effect which indicates the variation of the effective mass near the Fermi level due to the renormalization of the electron dispersion due to the electron-phonon interaction:

$$m^* = m_0(1+\lambda) \quad (2.19)$$

This parameter is linked to the Eliashberg function (we report only the final result, referring to literature for a more detailed discussion[104]) through an equation that offers an useful means of investigation of the electron-phonon interaction:

$$\frac{\partial\Sigma(E, T=0)}{\partial E}|_{E=E_F} = 2\int_0^{\omega_{max}} \frac{\alpha^2 F(E_F, \omega)}{\omega} = -\lambda \quad (2.20)$$

To obtain the mass enhancement parameter it is necessary to know the behaviour with energy of the Eliashberg function, or , alternatively, of the real (or imaginary) part of the self-energy. We will see that this procedure is really simplified in the case of the Dirac cone of the graphene where the dispersion of the band is linear.

Experimental details

Two fundamental radiation sources have been utilised for the measurements presented in this Thesis: synchrotron radiation and UV helium discharge lamp. Moreover, the essential experimental element in a photoemission chamber is the electron analyser, whose purpose is to separate photoelectrons of different kinetic energies and coming out from different emission angles.

The most common geometry is the hemispherical type, as the SCIENTA SES-200 employed during the ARPES measurements performed at the LoTUS Laboratory in Rome. A schematic view is presented in Fig. (2.4). It has an angular acceptance of $\pm 8^\circ$, an angular resolution of about 0.1° and an energy

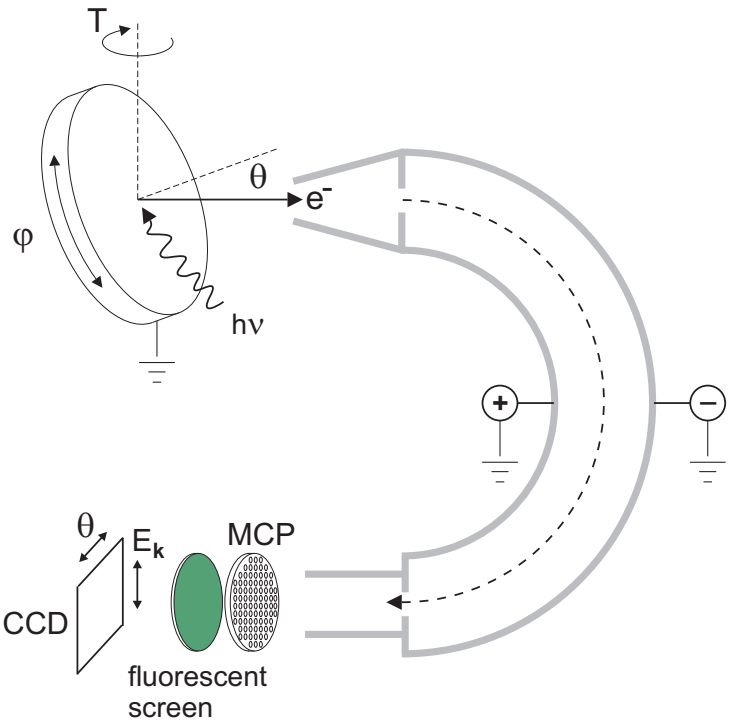

Figure 2.4: Schematic view of the experimental geometry of an ARPES experiments and the electron analyser.

resolution of about 11 meV (actually it depends on various parameters, this corresponds to the best achieved in the measurement here presented). It is essentially composed by three parts:

- an electrostatic lens system,
- the hemispherical analyser,
- the detector.

The electrostatic lens collect the photoelectrons and transfer them at the entrance of the hemispherical analyser. Before entry in the analyser the photoelectrons are slow down or accelerate until a fixed energy (*Pass Energy*). Between the lens and the analyser, a system of slits is installed. Slits and Pass Energy define the energy and angle resolution of the analyser, better for thin slits and small Pass Energy, to the detriment of the intensity.

The hemispherical analyser selects the electrons as a function of their energy. It is constituted by two concentric hemispherical electrodes, among them a potential difference is established. The electrons with an energy equal to the pass energy can traverse the analyser with the correct bend radius. The energy selection of electrons is made by varying the potential between the two shells.

Electrons are finally detected by a bidimensional electron multiplier, channeltron and multi-channelplate (MCP) electron multipliers, which ensures a gain of the order of 10^7. The detection system consists in a fluorescent screen and a CCD camera which registers the image produced by the impact of electrons on the screen. In the angular mode, one obtains the photoelectrons intensity as a function of the energy *and* the emission angle.

2.2.2 X-ray absorption spectroscopy

XAS is a technique to probe unoccupied valence states in presence of a core hole. It is an element-specific technique due to the unique binding energy of the core electron of the different elements. When the photon energy is scanned just before the absorption edge jump, core electrons will be excited to unoccupied states of the valence band, giving rise to sharp peaks (Near-Edge X-ray Absorption Fine Structure, NEXAFS). When the photon energy is higher than

the binding energy of the respective core-level, the photoelectron is excited to a continuum of states, and the smoother absorption structures are affected by the scattering environment (Extended X-ray Absorption Fine Structure, EXAFS). We are interested in the first process.

The intensity of the transition is cross-section dependent and the transitions are governed by the dipole selection rules, thus only the dipole allowed transitions ($\Delta l = \pm 1$) are contributing to the spectra, according to Eq. (2.3).

In this work we will study the absorption from an initial 1*s* state (K-shell excitation), whose final state is a *p* orbital and $L_{2,3}$ excitations, from a 2*p* orbital to a *d* or *s* orbital final state.

K-shell excitations

First NEXAFS experiments were performed on "low-Z molecules" [105], organic molecules containing important atomic building blocks (H, C, N, O, F) to determine their electronic and crystallographic structure when bonded to a surface. This choice was due to their natural abundance and to the high directionality of the covalent bonds between these elements. Furthermore the bond length depends on the hybridization.

The XAS technique has the advantage to be site-specific, selecting an atom species through its K-edge, and furthermore it can give the precise orientation of molecules on surfaces, by using linearly polarized radiation. We will concentrate on this last point, following Stöhr[106].

The unfilled orbitals measured by NEXAFS are very sensitive to the chemical state of the probed atom. For example, the energy separation between the π and σ-resonances in the spectra of linear and planar molecules is inversely proportional to the strength of chemical bonding. Meanwhile, shoulders and other fine structures appearing in the pre-edge region contain information not only on the chemical bonds within the molecule or solid cluster but also on the adsorbate-substrate interaction.

The calculation of the detailed resonance positions and intensities of molecular K-shell excitation spectra requires the knowledge of $\mid i >$ and $\mid f >$ state wavefunctions by solving Schrödinger equation. However we can consider some symmetry classifications that provide a one-to-one correspondence between res-

onances and molecular orbitals: for a K-shell excitation the initial 1*s* state is always spherically symmetric (σ symmetry). Final states allowed should have *p*-orbital component with either σ or π symmetry. Molecular orbitals have strong directional character linked to the molecular geometry. Within the Linear Combination of Atomic Orbitals (LCAO) expansion, we can write the initial and final states as

$$\begin{aligned} \mid i > &= R_{1s}(r) \\ \mid f > &= a \mid 2s > + b \mid 2p_x > + c \mid 2p_y > + d \mid 2p_z > \\ &= aR_{2s}(r) + R_{2p}(r)(b\sin\theta\cos\phi + c\sin\theta\sin\phi + d\cos\theta) \end{aligned} \tag{2.21}$$

where *a*, *b*, *c*, *d*, are the weight of the atomic orbitals and *R* the radial atomic wavefunction. Thus a maximum of the amplitude of the final state orbital is reached in the direction $\mathbf{O}=b\mathbf{e}_x+c\mathbf{e}_y+d\mathbf{e}_z$ determined by the superimposition of the three *p* orbitals. The three unit vectors are along the axes of the coordinate system.

Expressing the position vector in spherical coordinates, $\mathbf{r}=r(\sin\theta\cos\phi\ \mathbf{e}_x+\sin\theta\sin\phi\ \mathbf{e}_y+\cos\theta\ \mathbf{e}_z)$, and applying the dipole matrix element, we obtain:

$$I \propto |< f \mid \mathbf{e}\cdot\mathbf{r} \mid i >|^2 \propto |\ \mathbf{e}\cdot\mathbf{O}\ |^2 \propto \cos^2\delta, \tag{2.22}$$

where *I* is the intensity of the transitions, proportional to the probability P_{if}, δ is the angle between the direction $\mathbf{e}$ of the electric field and the direction $\mathbf{O}$ of largest amplitude of the final state. For oriented molecules and polarized X-rays, the intensities of resonances would thus exhibit strong and different angular dependence.

Elliptically polarized synchrotron radiation, can be viewed as a combination of two orthogonal linearly polarized waves, by defining a polarization factor *P* as

$$P = \frac{|\ \mathbf{E}^{\parallel}\ |^2}{|\ \mathbf{E}^{\parallel}\ |^2 + |\ \mathbf{E}^{\perp}\ |^2}, \tag{2.23}$$

where we considered X-ray propagating along z-axis and the x- and y-axis, with unit vectors $\mathbf{e}^{\parallel}$ and $\mathbf{e}^{\perp}$ lying in the horizontal and vertical planes, respectively.

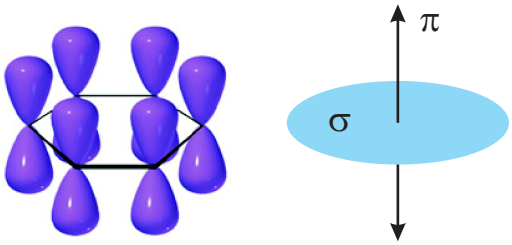

Figure 2.5: Left) Schema of an aromatic ring, the lobes represent the π* orbitals. Right) Direction of the orbitals: the π* orbital points in a specific direction while the σ* orbital spans a plane.

Then the transition probability becomes:

$$I \propto P \mid< f \mid \mathbf{e}^{\parallel} \cdot \mathbf{p} \mid i >\mid^2 + (1-P) \mid< f \mid \mathbf{e}^{\perp} \cdot \mathbf{p} \mid i >\mid^2 \tag{2.24}$$

In the case of molecules with orbitals pointing to a specific direction, as the case of an aromatic ring, such as benzene (C_6H_6), present in the phthalocyanine molecule, the atoms are arranged in a plane and thus the σ* system is characterized by this plane. While the π* orbitals can be represented by vectors perpendicular to the plane, as depicted in Fig. (2.5). In this case we can simplify the previous relations for a final state with vector and planar symmetry:

$$\begin{aligned} \mid \mathbf{e}\cdot < f \mid \mathbf{p} \mid i >\mid_v^2 &\propto I_v = \cos^2\delta \\ \mid \mathbf{e}\cdot < f \mid \mathbf{p} \mid i >\mid_p^2 &\propto I_p = \sin^2\epsilon, \end{aligned} \tag{2.25}$$

where δ and ϵ are the angles between **E** and the vector **O** or the normal of the plane, respectively.

Hence, concentrating on one orbital symmetry (vector case), we can rewrite Eq. (2.24) as:

$$I_v \propto P I_v^{\parallel} + (1-P) I_v^{\perp} \tag{2.26}$$

expressing the angle δ between $\mathbf{E}^{\parallel}$ and **O** along the orbital, as a function of the angles θ (between $\mathbf{E}^{\parallel}$ and the surface normal **n**), α and ϕ (polar and azimuthal angle of **O**, respectively) and considering the effect of the threefold symmetry of the graphene surface, we can neglect the azimuthal dependence and definitely

obtain

$$I_v^{\parallel} = \cos^2\theta\cos^2\alpha + \frac{1}{2}\sin^2\theta\sin^2\alpha = \frac{1}{3}[1 + \frac{1}{2}(3\cos^2\theta - 1)(3\cos^2\alpha - 1)$$
$$I_v^{\perp} = \frac{1}{2}\sin^2\alpha \tag{2.27}$$

The first experiment to determine the molecular orientation on a surface was conducted on the CO and NO molecules adsorbed on Ni(100) by Stöhr *et al.*[105], determining a standing up geometry in both cases.

$L_{2,3}$-shell excitations

The initial state of the $L_{2,3}$ absorption is a $2p$ orbital, therefore, for dipole selection rule the final state should be a $3d$ or a $4s$, however at the edge the spectra are dominated by the $p \rightarrow d$ channel which largely dominates the absorption process by 95%[107]. In this way we can investigate transition metal atom elements probing their valence d states, the $p \rightarrow d$ excitations have in fact energies in the soft X-ray regime.

The two different edges L_2 and L_3 originate from the spin-orbit splitting of the $2p$ core level: the L_2 starts from the $2p_{1/2}$, while the L_3 from the $2p_{3/2}$.

Differently from the K-shell excitation, where the single particle model could be applied since the density of final states reflects the actual empty DOS of $2p$ orbitals, for the $L_{2,3}$-shell a multiplet splitting theory should be considered[108]. With these limitations, it is not possible to univocally identify the absorption features of the $L_{2,3}$ edge. However the polarization dependence of absorption features is helpful to identify contributions from orbital with different symmetry.

Detection methods

X-ray absorption is an intrinsic synchrotron technique, since it needs a continuum of photon energies in energy range of X-rays and a highly collimated flux in order to detect absorption signal from a single molecular layer on the surface of a bulk material.

The intensity of photoelectrons, primary excitation channel, is the most direct method for measuring the absorption coefficient. But in this way we loose all

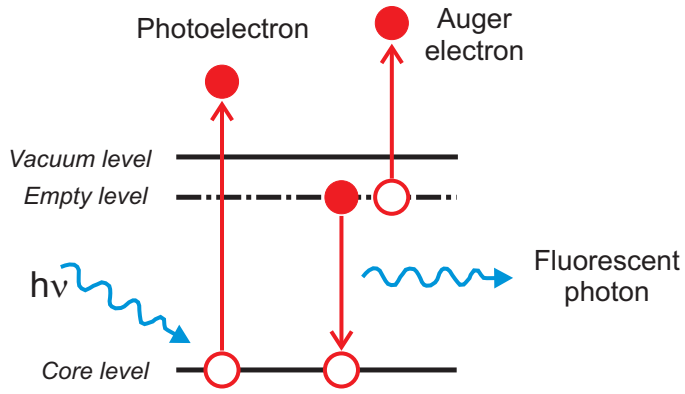

Figure 2.6: Schema of the processes after photon absorption: the primary channel is the production of phototelectrons, the secondary channel consists of Auger and fluorescent decays.

information about the bound state excitation. A secondary process of core hole annihilation is the emission of an Auger electron or a fluorescent photon from the system, as depicted in Fig. (2.6). In particular, for "low-Z molecules" the Auger decay is faster than the fluorescent decay.

Three ways for detecting electron decay are possible: Auger electron yield, partial electron yield and total electron yield. In total yield all electrons (not only Auger electrons, but also photoelectrons) that hit the detector are registered. In partial yield, a retarding voltage in front of the XAS detector is set in order to cutoff low kinetic energy electrons. Therefore, the PEY mode is more surface sensitive than the TEY mode. In Auger yield a hemispherical analyzer is used in an energy window (with a high and a low kinetic energy cut-off) defined by the energy of the Auger electrons expected for the defined transitions.

2.3 Temperature-programmed experiments

Thermal desorption experiments were originally devoted to the study of the desorption of gas and small diatomic molecules[109,110], recently this experimental investigation has been extended to large molecules[111–113], widening the field of applications to more complex systems.

2.3.1 Temperature-programmed fast XPS

Temperature programmed high-energy resolution fast X-ray photoelectron spectroscopy (TP-XPS) technique is usually exploited to follow in situ and in real time the kinetic of a surface reaction, looking at the modification of the surface composition during a chemical reaction[110].

Real-time X-ray photoelectron spectroscopy has been developed in recent years together with the third generation synchrotron facilities, which allowed an increasing of the time resolution of XPS experiments, thanks to the high brilliance of the soft X-ray radiation produced, which yields an increase of the photon flux of almost three orders of magnitude with respect to conventional anode-based sources, with much higher energy resolution ($<$50 meV)[109]. This is a peculiar strong point of the SuperESCA Beamline at ELETTRA[110].

This technique allows to investigate the mechanism of molecular adsorption, possible dependences on the surface temperature or presence of site-specific adsorption in function of coverage and has been exploited to study the interaction of CO with metal surfaces[109,110], or to follow the interaction of ethylene with Ir(111) during the formation of graphene[114].

Furthermore, temperature programmed real-time XPS, is an excellent probe of the molecular desorption processes, a cross-complementary study to Thermal Desorption Spectrometry (TDS): since the intensity variation of TP-XPS core level spectra is correlate to the coverage of the investigated specie on the surface, it provides information on how many molecules are still bound to the substrate, instead TDS tell us how many molecules are leaving.

2.3.2 Thermal Desorption Spectrometry

The heating in a suitably programmed way in vacuum of a solid sample, on which gases or molecules have been previously adsorbed, results in a spectrum of pressure changes. Recording these changes is a process called *Thermal Desorption Spectrometry* (TDS).

Thanks to the works of G. Ehrlich[115] and afterwards P. A. Redhead[116] and G. Carter[117], independently, the thermal desorption spectra could be analysed to yield data on the surface population in various adsorbed phases and to deduce the parameters of their desorption kinetics.

Before entering in deep in the argument, a brief description of the theory at the basis of this process will be given. The principle behind this technique is that the adsorbed molecule desorbs when the thermal energy of the molecule exceeds the activation energy associated with the bond between the adsorbate and the surface. In the case of physisorption the interaction between the adsorbed particle and the adsorbent is usually presented in the form of a van der Waals-like potential curve, in which the activation energy is the depth of the potential well. Treating the desorption process as a kinetic phenomenon leads to write an equilibrium relation between the surface and the gas phase concentrations of an adsorbent molecule, M:

$$[M]_s \leftrightharpoons [M]_g, \tag{2.28}$$

thus the desorption rate of adsorbed molecules from the surface is given by:

$$r_{des} = -\frac{dM}{dt} = k_d M^n, \tag{2.29}$$

where n denotes the order of desorption kinetics (typically 0, 1 or 2) and k_d is the so called reaction rate constant which, in general, follows an Arrhenius-type behaviour

$$k_d = \nu \exp\left(-\frac{E_d}{k_B T}\right), \tag{2.30}$$

where E_d is the activation energy, k_B is the Boltzmann constant, T the temperature and ν is a pre-exponential frequency factor [s^{-1}] associated with the change in the character of particle motion as particles transfer from the adsorbed to the free state and it is of the order of magnitude of the frequency vibration of the adsorbed molecule; in the case of physisorbing molecules, is typically assumed to be $\simeq 10^{13}$ s^{-1}. However this common accepted value has been contested and for large molecules have been showed that can be substantially larger[111–113].

In general both ν and E_d are coverage and temperature dependent. Within these assumptions, the resulting rate law is usually referred to the Polanyi-Wigner equation[118]:

$$r_{des} = -\frac{dM}{dt} = \nu M^n \exp\left(-\frac{E_d}{k_B T}\right). \tag{2.31}$$

During a TDS experiment the substrate temperature is increased linearly in time,

with a constant heating rate $\beta = dT/dt$, hence

$$T = T_0 + \beta t \tag{2.32}$$

In general one must consider the case of re-adsorption of molecules on the surface, that complicates the equation; however, in our case, and in general for experiments performed in UHV condition, the pumping speed is high enough to avoid readsorption to take place. So the ion current intensity acquired by the mass spectrometer is proportional to the desorption rate r_{des}, in a differential equation with respect to the temperature:

$$I(T) \propto \frac{\nu M^n}{\beta} \exp\left(-\frac{E_d}{k_B T}\right). \tag{2.33}$$

There are two main terms in Eq. (2.33): at low temperatures ($E_d \gg k_B T$) the exponential term is vanishingly small and there is no desorption signal, $I(T) \sim 0$. The exponential term rapidly increases when the temperature approaches the value of E_d/k_B; now the intensity of the desorption signal goes to a maximum and then drops back to zero. At the same time, consequently, the coverage M will reduce, quenching the contribution of the exponential. The product of this two contributions, the shaded area of Fig. (2.7), is an approximate representation of the desorption signal; the area behind the TD peak is proportional to the initial coverage.

Redhead has shown that, for first-order desorption ($n = 1$), the Polanyi-Wigner equation (2.31) can be solved for E_d providing[116]

$$E_d = K_B T_{max} \left[\ln \frac{\nu T_{max}}{\beta} - \ln \frac{E_d}{K_B T_{max}}\right] \tag{2.34}$$

and then simplified approximating the quantity $\ln(E_d/K_B T_{max}) = 3.64$, small compared to the first therm in brackets; this approximation is valid only if ν is known, assuming the ν=10^{13}s^{-1}, in fact plots of E_d vs. T_{max} are almost linear ($E_d \approx 0.003 T_{max}$), with T_{max} the temperature of the desorption peak.

The shape of a TD spectrum depends also on the kinetic order:

- $n = 0$ is a process where there is a complete desorption at once. The peak position (relative to T_{max}) increase by increasing the initial coverage;

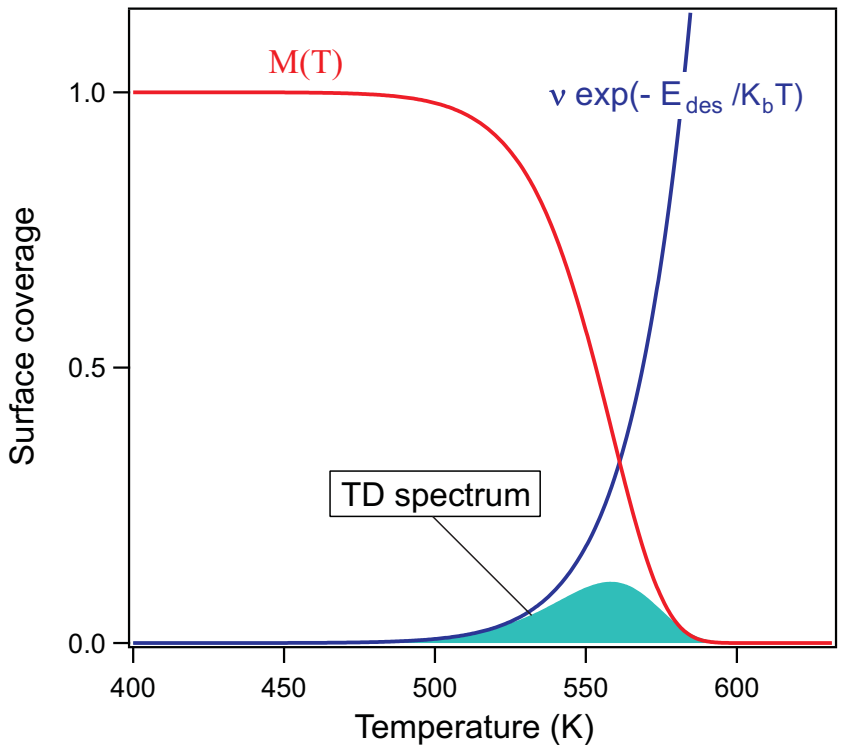

Figure 2.7: Simulation of the coverage curve $M(T)$ and the exponential term in Eq. (2.33). The shaded area correspond to the desorption spectrum. Simulation performed by C. Struzzi during her Master's Thesis[119].

- $n = 1$ is a non dissociative desorption (physisorption), without multiple process of readsorption. The peak does not change in temperature with coverage and the curve is asymmetric about the maximum T_{max};

- $n = 2$ is a process with possible recombinations between desorbed molecules and substrate. The shape of the spectrum is symmetric and the temperature at which the maximum rate of desorption occurs shifts to lower values as surface coverage increases.

Many other methods have been studied over years, with less assumptions, but they go beyond the scope of the analysis of the experiments proposed in this thesis.

Furthermore only in recent years the TDS technique has been applied to the study of large molecules adsorbed on surfaces[111–113], while at the beginning it was devoted to the study of dimers and gases[109,110]. Even the dispute on the correct value of the frequency factor ν is out of the scope of this work, since we are mainly interested in a comparison between similar molecules. Furthermore we use always the same heating rate and the same kind of molecules, so data are self-consistent even if probably affected by a systematic error in the estimation of the activation energy due to an uncertainty in the factor ν.

Experimental aspects

During a thermal programmed desorption experiment, three experimental aspects are to be considered:

- temperature measurement,

- temperature control,

- detection of the desorbing species.

The first two tasks are carry out by means of a programmable power supply system (*EUTRON*) interfaced with a temperature controller (*National Instruments* 9211) that reads the voltage of the thermocouple and regulates the heating power. This is indispensable since only thermal desorption spectra taken with a constant heating rate β (β=0.3 K/s in our experiments) can be quantitatively

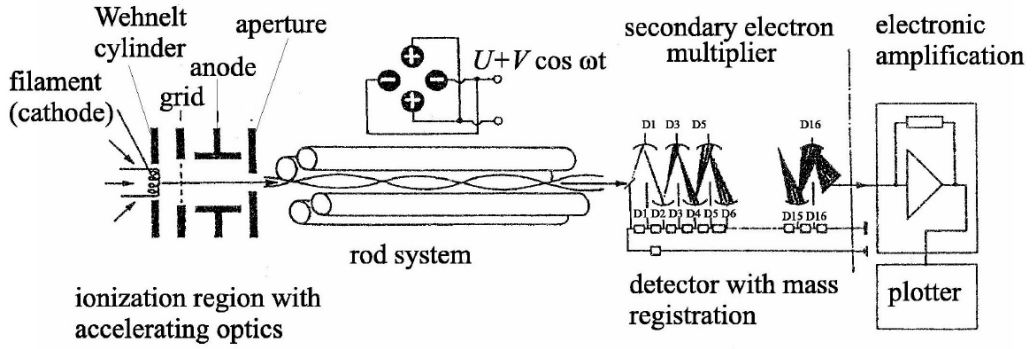

Figure 2.8: Parts of a quadrupole mass spectrometer.

analysed by the method described before. The temperature is measured using a K-type (chromel-alumel) thermocouple mounted to the side of the sample. The sample is based on the head of a manipulator heated resistively thorough a tungsten filament, capable to reach temperature of up to approximately 700°C.

The use of a mass spectrometer allows the determination of partial gas pressures, where the flux intensity of desorbing molecules is proportional to the ion current recorded by the mass spectrometer. Data acquisition software is controlled by LabVIEW and NiDAQ (National Instruments).

A quadrupole mass spectrometer consists of three components, as reported in Fig. (2.8):

- the ion source with electron impact ioniser and ion extraction optics,
- the actual quadrupole analyser consisting of four cylindrically rods,
- the ion detector (electron multiplier).

A quadrupole mass spectrometer first ionizes the gas molecules so that they can be accelerated into the quadrupole region, which is used to measure the mass to charge ratio (m/Ze) of the molecule. The ionization is achieved by extracting electrons by thermal emission from an electrically heated tungsten filament. A radio frequency potential is applied to a set of four rods, which creates a quadrupole field that is used to select ions with a specific mass to charge ratio (doubly ionised particles thus appear in the spectrum at half their molecular mass). The opposite rods are electrically connected and a voltage $U + V\cos\omega t$ is applied to both rod pairs. This voltage causes a vibration of

the ions passing through the quadrupole. The ratio $U/V = \lambda$ is constant during the measurement. The following equation is valid for each ion in the quadrupole field:

$$\frac{m}{e} = \lambda \frac{V}{\omega^2}. \tag{2.35}$$

Only those ions whose masses and charge fulfil the filter condition can pass through the quadrupole and reach the collector. Other ions vibrate unstably, land on the surface of the rods where they are charge neutralized and are filtered out. By changing the ratio U/V, it is possible to detect different masses (or ratios m/Ze). The ions are detected via the detection of their charges; they hit a metallic collector cone (Farady cup) and the transferred charge is recorded using an electron amplifier. For low ion currents, a secondary electron multipliers (channeltron) is used. The ion-current created is directly proportional to the partial pressure of the corresponding gas component.

There can be multiple (m/e) for a particular molecule due both to multiple ionizations and to *cracking of molecules*, that is breaking the molecule into fragments by the mass spectrometer itself. In this case the ionization does not occur by electron capture. Instead, positive ions are produced. As the electron passes close to the molecule, the negative charge repels and distorts the electron cloud, this causes a transfer of kinetic energy from the moving electron to the electron cloud of the molecule[120]. Cracking patterns are well documented and are unique for each molecule.

The iron-phthalocyanine molecule has an atomic mass unit (amu) of 568, too large for our mass spectrometer which can scan masses up to 300 amu. In this case, the cracking is helpful: in Fig. (2.9), is reported the cracking pattern for the gas phase of FePc as tabulated in the NIST (*National Institute of Standards and Technology*) Chemistry WebBook[121] and in Fig. (2.10) the mass spectrum, pression (P [mbar]) versus mass (m [amu]), recorded by our instrument during the evaporation of the FePc molecule (i.e. in function of the evaporator current, I [A]). In this spectrum we can identify some of the cracking fingerprint of the molecule, as, for example masses 50, 76, 101, 128, 147 originating from benzene and pyrrole components of the FePc molecules (C_4H_2, C_6H_4, $N_2C_8H_4$ ecc...). Even if in Fig. (2.9) the signal coming from masses 156, 184 and 284 appears to be intense, these are not revealed by our instrument, due to the low sensibility

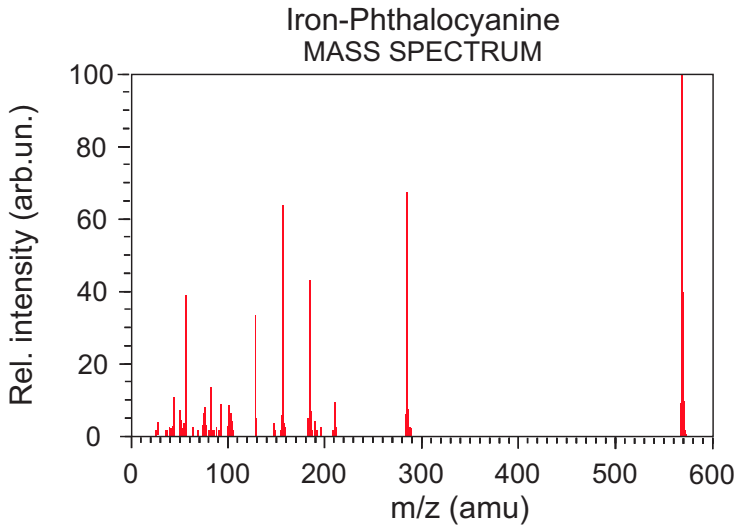

Figure 2.9: FePc mass spectrum of mass to charge ratio cracking patterns. Adapted from NIST[121].

to higher masses. While the other signals (1, 18, 28, 44 respectively H, H_2O, CO, CO_2) are due to residual gas in the vacuum chamber due to degas of the filament.

2.4 Low-energy electron diffraction

Low-energy electron diffraction (LEED) is a standard technique in surface physics for the determination of the surface structure of ordered materials by bombardment with a collimated beam of electrons and observation of diffracted electrons as spots on a fluorescent screen.

By the principle of wave-particle duality, the beam of electrons may be equally regarded as as succession of electron waves incident normally on the sample. These waves will be scattered by regions of high localised electron density, i.e. the surface atoms, which can therefore be considered to act as point scatterers. The wavelength of the electrons is given by the de Broglie relation:

$$\lambda = \frac{h}{p} = \frac{h}{\sqrt{2mE_k}}. \tag{2.36}$$

Since we are interested to microscopic structure of solids, electron wavelengths

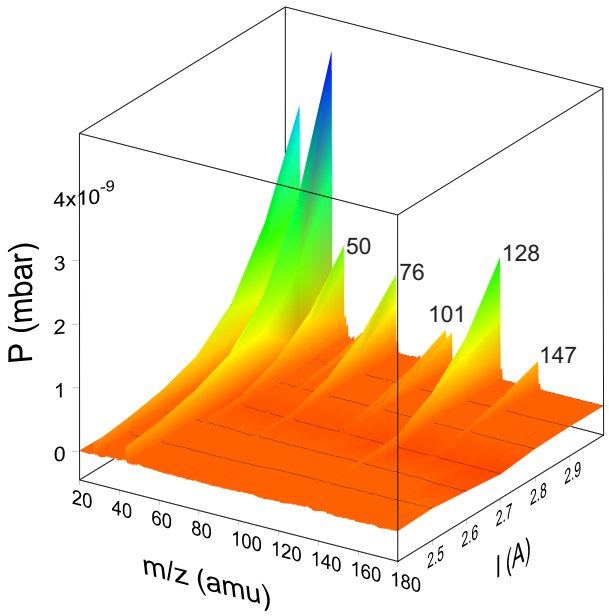

Figure 2.10: FePc evaporation: mass spectrum (pressure vs. mass) as a function of the current of the FePc evaporator.

must be chosen of the order of a lattice constant (≈ 1 Å), thus requiring energies in the range 20-200 eV. To study surfaces, low-energy electrons are better than X-rays, due to their small penetration in the solid, in fact the electron mean free path turns out to be minimal (5-10 Å) in this energy range (see Fig. (2.3)). This effective attenuation means that only a few atomic layers are sampled by the electron beam.

In analogy to optical grating, there will be constructive interference for reflected waves only in certain directions, described by the Bragg's law:

$$n\lambda_e = d_{h',k'} \sin\gamma, \tag{2.37}$$

where λ_e is the wavelength of incoming electrons, n the diffraction index, $d_{h',k'}$ the atomic rows distance. If the lattice constant increases, the constructive-scattering angle decreases; this is the reason of the reciprocity for the real and the reciprocal lattice. In parallel, by describing the electrons as waves with their wavevector $\mathbf{k}$, the phase difference between waves scattered by centres separated by a distance $\mathbf{a}$, is $\exp(-i\mathbf{\Delta k}\cdot\mathbf{a})$, where $\mathbf{\Delta k} = \mathbf{k} - \mathbf{k}'$ is the scattering wavevector, the difference between incoming and outgoing wavevector. Thus the Bragg's law (2.37) can be reinterpreted as the Laue conditions:

$$\mathbf{a}\cdot\mathbf{\Delta k} = n2\pi, \tag{2.38}$$

Reminding the definition of reciprocal lattice as the set of wavevectors $\mathbf{G}$ generating waves with the periodicity of a given direct lattice $\mathbf{R}$, so is valid $\exp(i\mathbf{G}\cdot\mathbf{R})$; therefore Eq. (2.38) is verified when $\mathbf{\Delta k} = \mathbf{G}$, that is the diffraction intensities will have a maximum for those directions identified by a reciprocal lattice vector (here we are dealing with the parallel component of momentum, due to the symmetry breaking in the orthogonal direction with respect to the surface, as in the case of photoemission, while the orthogonal component is given by the energy conservation law).

A geometrical interpretation of Eq. (2.38) is provided by the Ewald construction and allows the determination of the diffraction pattern from a given surface: each reciprocal lattice point is associated with a line drawn perpendicular to the surface plane, the electron wavevector $\mathbf{k_i}$ centred in the point (0,0) defines the sphere's radius; the intersection points between the sphere and the lines sat-

isfy the momentum and energy conservation laws and determine the diffraction spots. Thus, the more the energy of the incoming electron beam, the more the reciprocal lattice surface becomes accessible.

In the kinematic theory electrons are elastically scattered only once by the surface, thus neglecting multiple diffractions. This is a simple description but well suited to give information on the geometric structure of the surface, even if for low-energy electrons multiple scattering phenomena are highly probable with respect to X-rays. In this approximation, the incident electron is represented by a plane wave, while the scattered as a spherical wave; by considering an ordered lattice, the electron wave function becomes

$$\psi \propto \underbrace{\sum_{nm} \exp^{i\mathbf{\Delta k}\cdot\mathbf{R_{nm}}}}_{G} \underbrace{\sum_{j} f_j(\mathbf{k},\mathbf{k'}) \exp^{i\mathbf{\Delta k}\cdot\mathbf{d_j}}}_{F} \tag{2.39}$$

in common with all the diffraction techniques, there are indicated the factor G, amplitude of the diffracted beam, and the factor F, the atomic form factor. The first term was already discussed in this paragraph and defines the maxima of intensity, the second term, determines a modulation of this intensity which goes beyond the purpose of the analysis proposed in this thesis.

2.4.1 Experimental apparatus

In Fig. (2.11) is schematized a common LEED experimental apparatus. The main components are:

- electron gun: it is composed by a filament (cathode), which emits electrons when directly heated by a current flow. A following electrostatic lens system and a drift tube provide the acceleration energy and the shaping and focusing of the electron beam. The exit drift tube and the sample are both at ground potential, in order to not affect the electron trajectories. Usual emission current is of the order of μA. The beam size is ≈1 mm.

- Detection system: the fluorescent screen is preceded by 4-grid optics system; the first and the last grid are at the same potential of the sample and the electron gun, the two central grids (*suppressors)* are negatively biased

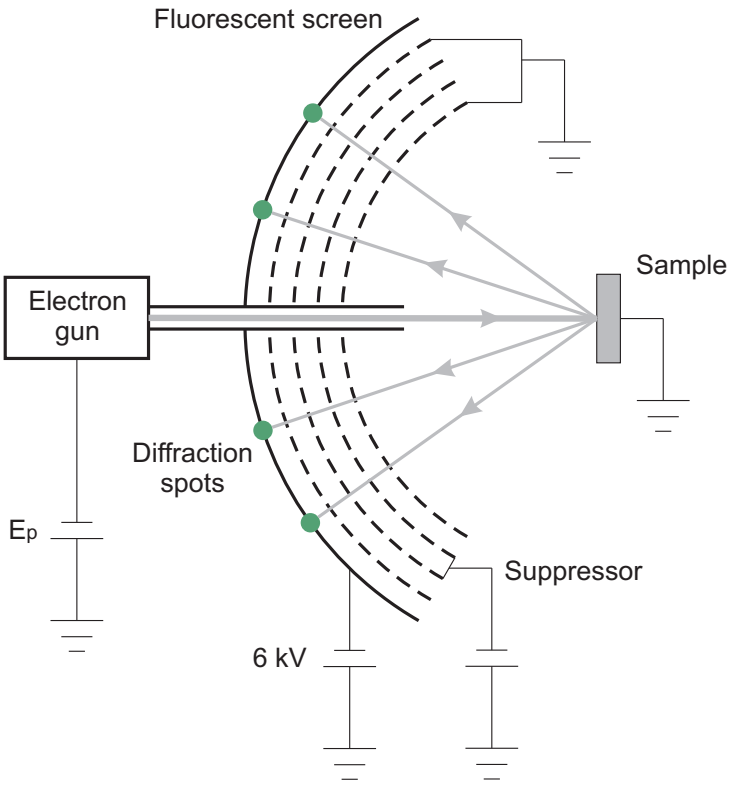

Figure 2.11: Standard experimental set up for a typical 4-grid LEED system.

(a few eV), in order to prevent the background illumination produced by inelastically scattered secondary electrons. By a positive high voltage of 6 keV, electrons are finally accelerated to the screen, where diffraction spots become visible and corresponds to the directions given by the lines of the Ewald sphere.

2.5 In situ preparation of graphene on Ir(111)

The Ir sample is cleaned with an usual procedures:

- subsequent cycles of Ar^+ sputtering (E = 2 keV),
- annealing at 1470 K,
- oxygen treatments to remove carbon impurities (T=570-970 K, P=1×10^{-7} mbar)
- hydrogen treatments to remove residual oxygen (T=370-670 K, P=5×10^{-8} mbar)

This procedure ensures a clean Ir(111) surface with a sharp hexagonal LEED pattern. Actually the oxygen and subsequent hydrogen treatments are not strictly necessary if the purpose is the graphene growth, since the eventual carbon impurities on the Ir surface will then take part in the graphene formation.

For graphene growth, two ingredients are necessary: a carbon source and high temperature (this last necessary also for the cleaning of the Ir sample). As carbon source are commonly used carbon-containing molecules such as hydrocarbons; the most commonly used is ethylene (C_2H_4)[122], which is known to have a sticking coefficient near unity on the Ir(111) surface[123], thus the formation of graphene is self-completing and no carbon multilayers can form. This fact allows the formation of large domains of graphene, up to hundreds of nm, as probed by STM experiments[46]. Ethylene is dosed at room temperature in a background pressure of 2×10^{-7} mbar for 60 seconds, this ensures the saturation of the surface. Then the annealing up to $\approx$ 1500 K of the substrate covered to saturation leads to complete decomposition of hydrocarbon, which is completed after 700 K[114,124].

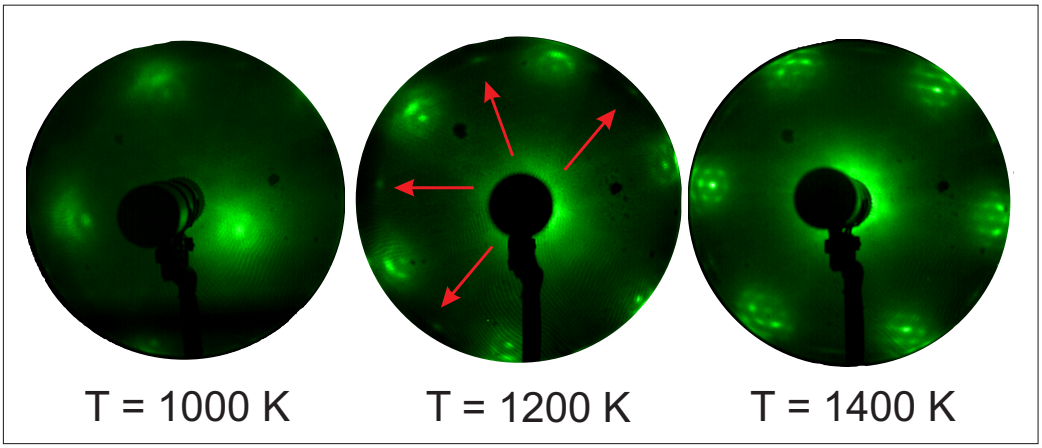

Figure 2.12: LEED patterns in function of the maximum flash temperature while growing graphene on Ir(111). In the central panel, red arrows indicate the R30° spots.

The procedure of dosing-annealing is repeated several time, assuring a complete covering of the iridium surface[125].

This procedure is known as temperature-programmed growth (TPG), another procedure which give similar results is the chemical vapor deposition (CVD) where the gas is dosed in an unique cycle on the hot sample surface.

The annealing temperature is important for the alignment of the graphene sheet with respect to the Ir(111) surface[126]. In Fig. (2.12) we report three LEED patterns of as many graphene growths at different annealing temperatures. We can note that only above 1400 K we obtain a sharp moiré pattern (for a detailed description of the LEED structure of graphene/Ir, see next Chapter), with an oriented R0° phase. In the intermediate LEED pattern, a spot is visible in between the principal spots, indicated with red arrow, this is due to rotated graphene domains (R30°)[126], for low temperature growing the intensity of the moiré pattern and the sharpness of the carbon-related spots are strongly reduced, indicating a disordered and non complete graphene layer.

Furthermore we demonstrated [I] that a graphene prepared ex-situ can be perfectly recovered in UHV by subsequent annealing up to 900 K. Both graphene and iridium electronic states remains unaltered by the contact with air [I,II,127].

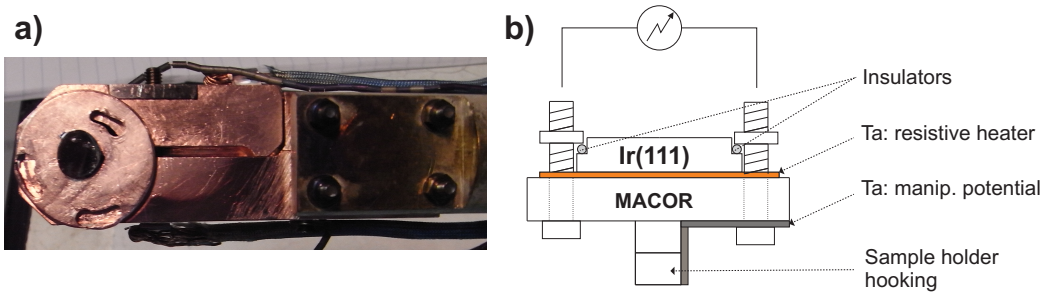

Figure 2.13: a) Photography of the original manipulator head and sample holder on copper. The sample holder is screwed in the manipulator head, the screw control the azimuthal orientation. b) Schema of the first new resistive heater.

2.5.1 LoTUS Lab. upgrading

Beyond the scientific aspects of this Thesis, the PhD has been devoted also to the design and realization of a new system to allow the growth of graphene *in situ* at the LoTUS Laboratory in Rome.

As we have seen in the previous paragraph, two main ingredients are essential for graphene growing: a carbon source and high temperature. The first task has been achieved by equipping the UHV preparation chamber of the LoTUS Lab. with a gas line system with a leak-valve for ethylene dosing.

However, the great part of the experimental work has concerned the fulfilment of the second task: to achieve high temperatures. The original manipulator of the UHV system at LoTUS is provided with a resistive heater which allows to reach a maximum temperature of about 900 K. The sample is mounted on the manipulator head, which is on copper, as showed in the phtography of Fig. (2.13 a). This conformation is not suitable for the *in situ* preparation of graphene for at least two reasons: the maximum temperature is too low (about 1500 K are needed) and in any case the copper head cannot reach as high temperature without melting. So a completely different home-made heating mechanism must be designed.

A further complication is that the azimuthal rotation of the sample on the manipulator head have to be conserved, this is an indispensable requirement for ARPES mapping along high symmetry directions, thus excluding the "easier" solution of a fixed sample configuration heated by electron bombardment from behind.

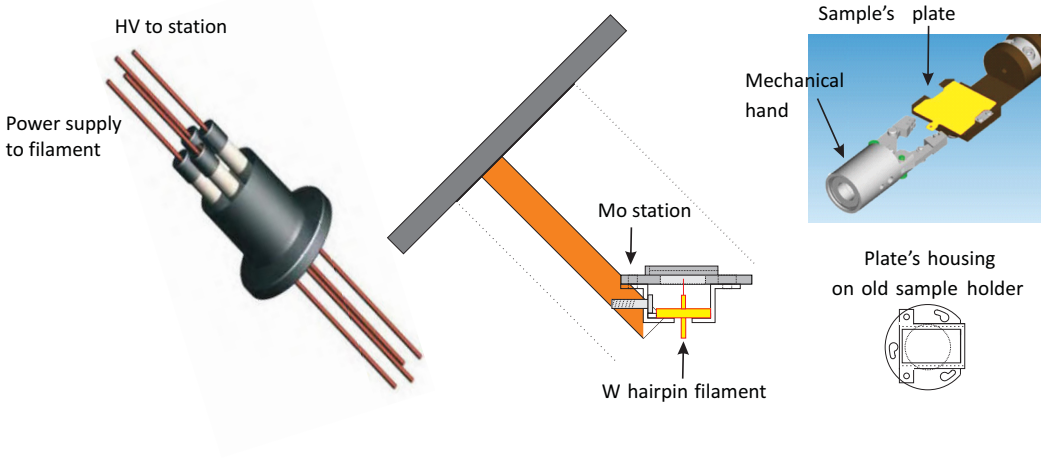

Figure 2.14: New heating system and sample housing: all the main components are indicated. See more description in the text.

On the other way, to buy a new commercial manipulator head integrated with electron bombardment heating and available degrees of freedom, it would have been a cost too high to face.

A first attempt was a new resistive stage integrated in the manipulator head thermically separated by a properly designed ceramic support (MACOR). The sample is mounted directly on a thin tantalum sheet (25 μm-thick) where a current of about 25 A is furnished by a separated electrical feedtrough put in contact whit the tantalum sheet. A schema is depicted in Fig. (2.13 b). This technique allowed the first realization of graphene in the LoTUS Lab., without a drastic change of the original configuration. However the low stability of the system has motived the project of a new system.

The basic idea of the new project was to separate the heating station from the manipulator head in order to be free to use an electron-bombardment system, more stable and easy to use. So we designed a separated electron-bombardment heating stage mounted on a four-pins electrical feedtrough, as depicted in Fig. (2.14). The stage is made of molybdenum and it is fixed to two of the four pins. It provides housing to a hairpin tungsten filament (the yellow element in the figure) mounted on a round ceramic base which isolated it from the hosting structure. Two kapton insulated copper wires are used to connect the filament's contacts to the other two pins of the feedtrough, while the pins where the Mo

stage is mounted are used to polarize it with V≈2 kV, in order to accelerate the electron emitted by the filament towards the sample.

The sample is mounted on a suitable designed tantalum plate with an opening corresponding to the back of the sample, and to the tip of the filament, when placed in the heating stage, thus allowing a direct bombardment of electrons from the filament to the sample. A mechanical hand, like the one in Fig. (2.14), is utilised to move the plate inside the preparation chamber. A guide-rail housing for the plate is used on the heating stage and has been designed for the old manipulator head. In this way the separation of the heating stage from the manipulator has allowed to maintain the old manipulator only with a little modification of the old sample holder.

Even if tests are still running with small improvements, this new system has proved a better stability and control with respect to the previous one, and it is more "user-friendly", allowing a fast and easy reaching of the temperature desired.

2.6 Molecule's evaporator

The MPc molecules was deposited by molecular beam epitaxy in highly controlled UHV conditions. Molecular beam epitaxy is attained by sublimating MPc powders (supplied by Sigma Aldrich) contained in a quartz crucible resistively heated with tungsten (or tantalum) coils by current flowing. The sublimation temparature of MPcs is around 400-500°C[128]. A typical evaporator is a common electrical feedthrough mountend on a CF40 flange directly in the preparation chamber. At the head of two conductive pins are integrated the coils which hosts the quartz crucible.

Before the evaporation of molecules onto the sample, a procedure of degas is followed, by slowly heating the molecules until they reach the sublimation current (usually of the order of 2.5-3.5 A, depending on the way the evaporator is built up), in order to clean them from impurities due to their contact with air and to reach evaporation in the low 10^{-9} mbar range; this procedure may take even a week.

Evaporation rate on the sample surface was determined using a quartz microbalance and the nominal evaporation rate actually employed was $\approx$ 1Å/min.

Chapter 3

Characterization of graphene on Ir(111)

This chapter is entirely dedicated to the characterization of graphene grown on Ir(111). We start studying its structure through the diffraction of low-energy electrons (LEED) which shows the characteristic moiré pattern due to the lattice mismatch between the iridium and the carbon lattice. This super-periodic structure is one of the characteristics that makes supported graphene, and in particular graphene epitaxially grown on transition metal substrates, appealing for adsorbate deposition, exploiting the moiré as a pattern for ordered nano-architectures. By exploiting synchrotron-based X-ray techniques (X-ray absorption and X-ray photoelectron spectroscopy) we characterized our sample, highlighting the difference among graphene prepared on other substrates. Finally, by angular resolved photoemission spectroscopy performed in the LoTUS Laboratory in Rome, we concentrate on the Dirac cone region of the surface Brillouin zone.

The control of the graphene-substrate interaction is a first fundamental step in the definition of a good template for molecules adsorption. In this sense, ARPES is a fundamental method to single-out the basic parameters identifying graphene electronic structure.

3.1 Moiré superstructure

Graphene honeycomb lattice has been described in Section (1.1.1). Also the (111) surface of iridium *fcc* crystal is described as a bidimensional hexagonal lattice, however these two structures differ for the real-space periodicity: 2.461 Å for a single carbon layer in graphite and 2.715 Å in Ir(111). The superimposition of two similar structures with a slightly different periodicity leads to the formation of a third lattice with larger periodicity: this is the moiré effect. In everyday life we can have to do with this effect, for example, taking a photo with a digital camera of a TV screen: an interference pattern arises due to the different resolutions of these two instruments, and by zooming the photo we can even see the fringes moving.

In physics, this superstructure can be described by a reciprocal lattice vector, $\mathbf{k_m}$, given by the difference between the two constituting reciprocal lattice vectors, in this case graphene $\mathbf{k_g}$ and iridium $\mathbf{k_{Ir}}$:

$$\mathbf{k_m} = \mathbf{k_g} - \mathbf{k_{Ir}}. \tag{3.1}$$

By STM measurements[46,129], it has been observed that epitaxial graphene grows on Ir(111) preferentially with the $[11\bar{2}0]$-direction perfectly aligned with the $[1\bar{1}0]$-direction of the Ir substrate. In this case the moiré pattern can be described by a scalar equation:

$$\frac{2\pi}{a_m} = \frac{2\pi}{a_g} - \frac{2\pi}{a_{Ir}}, \tag{3.2}$$

where a_m, a_g and a_{Ir} are the real-space repeat distance of the moiré superstructure, the graphene overlayer and the Ir(111) substrate, respectively.

We performed a LEED analysis on a clean graphene/Ir(111) sample, after the air-transport among different laboratories and an annealing procedure constituted by several subsequent annealing cycles at increasing temperatures up to about 900 K. The LEED pattern of the clean graphene/Ir(111) layer Fig. (3.1 a) is characterized by six pair of spots arranged in a hexagonal structure [I]: inner spots are due to the Ir(111) surface and outer spots are associated to the graphene C_g lattice, whose surface lattice constant is smaller than the Ir one, in very good agreement with previous observations performed on in-situ prepared samples[46].

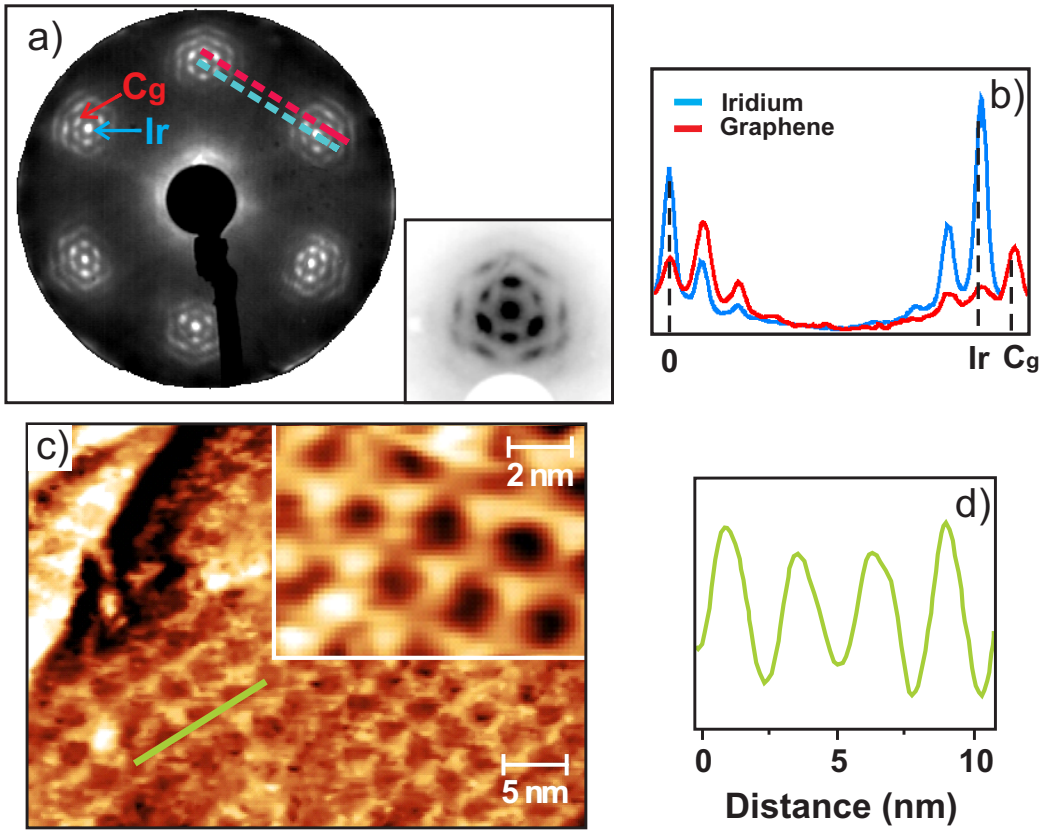

Figure 3.1: LEED patterns taken with the sample kept at liquid nitrogen temperature (*a)* E_p=142 eV and inset E_p=70 eV, with the sample tilted to show the (0,0) spot (with inverted colours) of the graphene single-layer on Ir(111), showing the typical moiré pattern; *b)* line-profile scan across the main spots of *a)*; *c)* STM image taken at low-T at ID08 beamline (ESRF); *d*) line-profile scan across the green line of *c*).

The diffraction pattern is characterized by several circles of satellite spots surrounding the Ir and C_g, indicating the presence of a highly-ordered superstructure with a large periodicity (in the real space): the moiré pattern, enhanced in the inset of Fig. (3.1 a) where the diffraction pattern of the central (0,0) spot at lower energy (70 eV) is shown by tilting the sample. This moiré superstructure is due to multiple scattering events, originating from the superposition of two regular lattices (iridium and graphene) with a slight mismatch between them, as stated before. The absence of intermediate spots in between the visible hexagon, is a sign of non rotated (R=0°) graphene domain, thus oriented as the Ir(111) substrate.

The spot profile shown in Fig. (3.1 b) (averaging over several images taken at different energies) allows the determination of the spot distance ratio (C_g to Ir) resulting 1.10±0.01 [I]. Taking into consideration the Ir(111) surface lattice as reference (2.715 Å), we can evaluate the surface lattice vector of graphene, resulting 2.47±0.03 Å (9% smaller than the Ir one), in agreement with the value of the carbon distance in graphite (2.461 Å)[130]. This leads to a moiré lattice with a periodicity of 27.7 ± 3.5 Å.

A more detailed analysis can be done regarding directly the moiré spots, thanks also to a better statistics available. By measuring the distance of the moiré maxima, using again Ir(111) surface as a reference, we obtain a more precise value of the periodicity of the superstructure, 26.1±0.5 Å and of the carbon repeat distance, 2.459±0.005 Å. These results are in good agreement with similar analysis on the same system and consistent with STM results[46].

The fact that the ratio between graphene (and iridium) basis vector and moiré is not an integer, $r_g/m = 10.6 \pm 0.2$ and $r_{Ir}/m = 9.6 \pm 0.2$, affects the diffraction intensity of the moiré-related spots: only the first one or two orders of satellite spots are visible, sign of an incommensurate superstructure.

In Fig. (3.1 c) we present STM measurements performed at the beamline ID08 of ESRF (as a side activity): the moiré superstructure of graphene on Ir(111) is evident, the line profile in Fig. (3.1 d) is a confirmation of the ∼2.5 nm moiré periodicity.

The different periodicity of the two generating lattices, implies a different possible arrangement of the carbon atoms with respect to the iridium atoms within a moiré unit cell, identifying three peculiar regions[131]:

- *fcc* region: an Ir fcc site is in the centre of the honeycomb ring;
- *hcp* region: an Ir hcp site is in the centre of the honeycomb ring;
- *atop* region: an Ir atom lies in the centre of the honeycomb ring.

While *fcc* and *hcp* have similar atomic configurations, the *atop* region differs having no carbon atoms directly positioned above an Ir atom. These differences are at the origin of the typical STM images (see Fig. ((3.1 c)) which show an alternation of bright and dark spots, these latter correspond to *atop* regions. The presence of substrate atoms directly below C atoms in *hcp* and *fcc* regions creates energy minima where the hybridization with the substrate is favoured. This chemical inhomogeneity, reflects also in the geometrical corrugation: the chemical bonds between carbon and metal atoms reduce the height of the layer on top of the Ir surface plane from $\approx$ 3.8 Å to $\approx$ 3.2 Å, calculated by density functional theory (DFT)[132]. *Hcp* and *fcc* regions will be then preferred site for adsorption, as confirmed by experiments[93].

3.2 Carbon 1s absorption edge

The carbon K-edge of graphene/Ir(111), taken with linearly polarized radiation is reported in Fig. (3.2): it presents three main absorption structures: the main peak at 285.5 eV corresponds to C $1s \rightarrow \pi$* transitions, while the structures at 291.8 eV and 292.8 eV are due to the threshold of the transitions towards the σ_1* and σ_2* orbitals, respectively. Higher energy structures can be individuated at 297.1 eV, 301.1 eV, 304.8 eV and 308.0 eV, mainly related to transition towards unoccupied high energy σ bands at the M point, as deduced by a direct comparison with the unoccupied-band structure. All these structures are present in the HOPG spectra[133]: the overall shape is very similar, thus indicating a lack of strong chemical bonding of graphene to Ir(111), however strong enough to force the overlayer in registry with the substrate, as confirmed by the presence of moiré spots in the LEED pattern (Section (3.1)).

As it concerns the fine structure of the data, small changes occur and their assignment is highly debated in the literature. A pre-threshold shoulder at about 284.4 eV can be detectable. In Fig. (3.3, left panel) we deconvolved the threshold

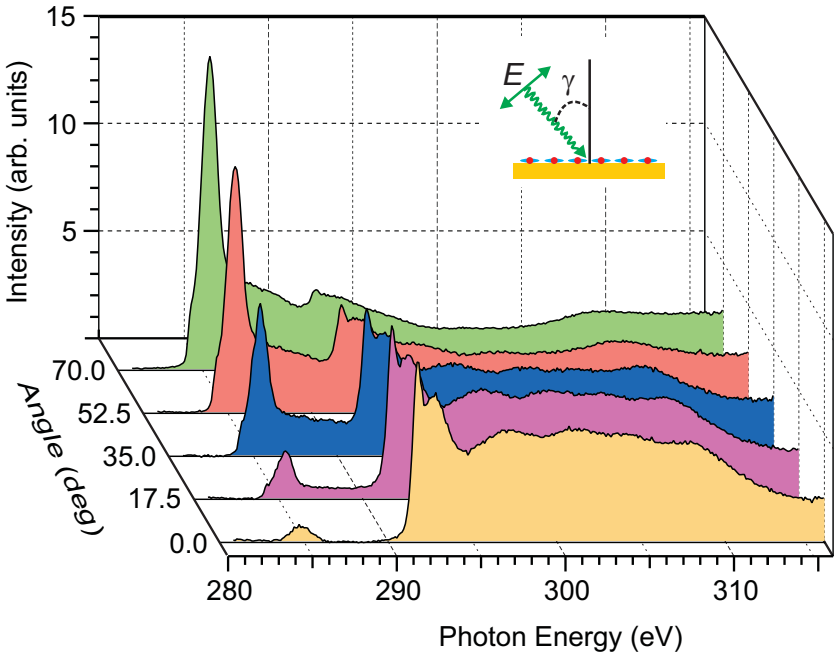

Figure 3.2: Angular dependent X-ray absorption spectra across the carbon K-edge of graphene/Ir(111) with linearly polarized radiation. γ is the angle between the incident photon and the surface normal, as sketched in the inset. The higly dichroic signal reflects the strong anisotropy of the σ and π orbitals resulting from the two-dimensional nature of the graphene sheet.

with a step-function background and two Gaussian peaks corresponding to the pre-edge state (dark gray) and the π* state (light gray), located at 284.45 eV and 285.50 eV and with FWHM of 0.6 eV and 1.2 eV, respectively.

Similar structure has been observed by NEXAFS in graphene nanoribbons grown on Pt(111)[134,135] and attributed to their edge geometry: grains with zigzag-shaped edge regions show the presence of a localized edge state just above the Fermi level, whereas the armchair edge does not exhibit this feature[136]. Another similar feature is reported for graphene of considerable size (10μm) prepared by micromechanical cleavage of HOPG on SiO_2 substrates, by Pacilé *et al.*[137,138] and for graphene epitaxially grown on Pt(111)[42]. Since, even epitaxial growth of graphene on Ir(111) leads to large graphene areas[46], for these samples the edge contribution is negligible. An explication to our observation comes from the DOS of the single layer graphene calculated in the local-density approximation by Trickey *et al.*[139] and reported in Fig. (3.3 b), which shows a peculiar unoccupied density of states of the single carbon layer, just before the π* resonance. A modification of the band structure in the vicinity of the Fermi level, which can produce this kind of pre-edge features, is also expected in presence of orbital mixing with the substrate[41,42].

The assignation of π* and σ* peaks can be explained by a polarization-dependent study. The C K-edge absorption spectra of graphene show pronounced changes as the angle γ between the electrical vector of light and the normal to the surface plane is varied, reflecting the symmetry of the final state (σ* or π*), as evident in Fig. (3.2), where a sequence of five spectra taken at different angles is presented. The two-dimensional nature of graphene (and graphite as well) results in a strong directionality of the orbitals: σ orbitals lie within the basal plane, while π orbitals are directed perpendicular to the basal plane. Both σ and π bands have their replica on the unoccupied side of the DOS, σ* and π* states, respectively. By using tunable polarized synchrotron light, it is possible to excite final state of a specific symmetry from K-shell initial state, depending on the orientation of the incident photon polarization vector with respect to the basal plane. When the $\mathbf{E}$ vector lies within the basal plane, σ final state are selected, when the $\mathbf{E}$ vector is perpendicular to the plane, states of π symmetry are excited, according to the dipole selection rules.

For electric dipole transitions excited by linearly polarized radiation, the in-

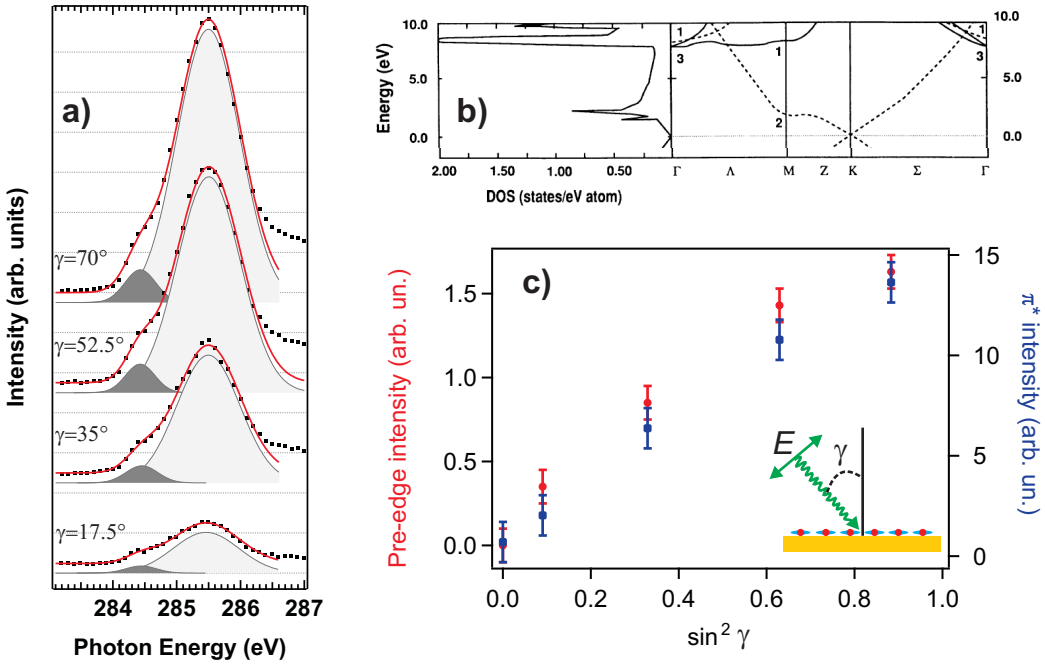

Figure 3.3: *a)* Zoom on the edge peak of the NEXAFS spectra of Fig. (3.2), experimental data (black dots) and fit (continuous red line) with two Gaussian (shadowed peak) for different incidence angle γ. *b)* Bare Kohn-Sham energy bands (right) and density of states (left), solid/dashed curve: σ/π bands, for the unoccupied side. Adapted from ref.[139]. *c)* Intensities of the pre-edge peak (red dots) and the main peak (blue dots) plotted in different scale: their common linear behaviour as a function of $\sin^2\gamma$ confirms their π* character.

tensity varies as $\cos^2\delta$, where δ is the angle between the radiation polarization and the vector orbital (see Sec. (2.2.2)). The peak intensity was obtained by the deconvolution shown in Fig. (3.3 a). The linearity of the data as a function of $\sin^2\gamma$ (γ is the angle between the incident photon and the surface normal) shown in Fig. (3.3 c), confirms the assignment of both peaks to $1s \rightarrow \pi$* transitions. This is not surprising for the peak at 285.5 eV, instead it is a confirmation that the pre-edge peak is originated by the split of the π* band, together with the fact that the ratio between this two peak is constant ($\approx$ 1:10).

The non-vanishing signal, before the σ* threshold, in the in-plane spectrum (Fig. (3.2)) should be forbidden by selection rules in this geometry. Actually the position of this residual peak is not in correspondence to the π* peak at 285.5 eV. It is probably due mainly to carbon impurities often present on the mirrors and to the roughness of graphene on Ir(111), hence to the moiré corrugation. However the carbon impurities on the mirrors will not affect the pre-edge peak at other angles since they will not have an angular dependence, as instead reported here and consistent with a splitting of the π* band.

The definitely highly dichroic C K-edge signal, due to the intrinsic nature of the electronic levels in graphene, with in-plane σ* states and out-of-plane π* levels, confirms the high-quality well defined single-layer preparation on Ir(111).

Another debated energy region is that between the π* and σ_1* resonances, where a weak shoulder at about 289.1 eV can be identified and attributed to an interlayer state of graphite, predicted for single-layer systems[11,140], experimentally observed in graphene[137,138], and recently theoretically explained as the lowest-energy member of image potential states present even in single-layer graphene[141]. However, in the same region possible contaminations of COOH and/or C-H species at surface would give σ* transitions[142], so the *interlayer state* experimental observation was questioned[143]. However, in our case, no sign of contamination has been detected by an eventual chemical shift of the C 1*s* spectra, very sensible to any modification of the chemical environment, as reported in the following paragraph.

Furthermore, the pre-edge shoulder and the absence of a double main C 1*s* $\rightarrow \pi$* peak demonstrate that there is a weak interaction of the graphene sheet with the Ir(111) surface, similar to the case of Pt(111)[42]. In fact, for graphene grown on other transition metal surfaces with less occupied *d* bands, such as Rh,

Ru or Ni, there is a broadening of the first C 1*s* $\rightarrow \pi$* peak and the emerging of new hybridization-induced gap states due to high p_z (graphene)-*d* (substrate) orbital hybridization which indicates a strong interaction[41,144,145], also reflected in the σ* resonances. Even the main absorption resonance for graphene prepared on semiconductors presents a much wider peak structure[146].

3.3 Core levels photoemission

In this paragraph, we describe the two main characteristic core level for graphene/Ir(111) system: C 1*s* and Ir $4f_{7/2}$. The XPS were collected at the SuperESCA beamline at normal emission with a photon energy of 400 eV and 136 eV, respectively.

3.3.1 C 1s

The C 1*s* structure of single-layer graphene, presented in Fig. (3.4 left panel), is characterized by a narrow peak at 284.12 eV binding-energy (BE). After a Shirley background subtraction, the fit was performed with a Gaussian curve (due to the phonon and instrumental broadening) convoluted with a Doniach-Šunjić line profile[147], characterized by a Lorentzian width (due to the finite core-hole lifetime) and a slight asymmetry parameter α=0.10 (due to the creation of electron-hole excitations near the Fermi level), this last parameter is an index of a metallic behaviour of the material. The full-width at half-maximum (FWHM) was found to be 0.27 eV. These results are in agreement with previous determination on graphene/Ir(111)[41,132,148,149].

The arrangement of the carbon atoms with respect to the iridium surface atoms within a moiré unit cell, described in the previous paragraph, actually affects the C 1*s* core level. A linear correlation between the graphene-Ir(111) distance and the C 1*s* core level binding energy has been calculated[132]. The experimental spectrum is thus made of the contribution of all the 200 carbon atoms of a moiré unit cell, in different domains and adsorption sites. Hence the shape and the FWHM of the C 1*s* core level is determined by the morphology of the graphene sheet and so will depend on the substrate where the carbon layer is grown.

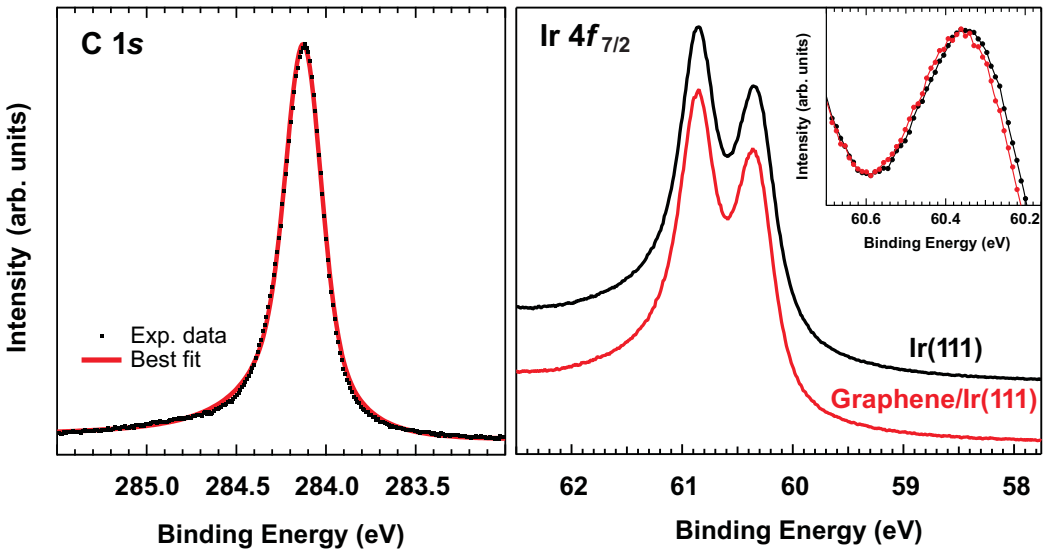

Figure 3.4: X-ray Photoelectron Spectroscopy (XPS) data of the C 1*s* (left) and Ir $4f_{7/2}$ (right).

In the case of graphene grown on Pt(111) and Ir(111), the C 1*s* core level is characterized by a single peak, narrower on Pt than on Ir, sign of lower corrugation and orbital mixing[41]. The higher corrugation and interaction of graphene grown on Rh(111) and Ru(0001), hence the higher differences between carbon atoms in the moiré unit cell with respect to Ir(111), splits the C 1*s* line in two distinct components generated by carbon atoms farther from the metallic surface (lower binding energy) and by those closer to the substrate, more strongly bonded (higher binding energy)[41].

3.3.2 Ir $4f_{7/2}$

The Ir $4f_7/2$ core-level of the Ir(111) surface, Fig. (3.4 right panel, black line), is characterized by a double peak attributed to a bulk and a surface component, with binding energies of 60.855 and 60.310 eV, respectively, hence separated by 545 meV. This surface core-level shift (SCLS) is typical for a large variety of 5*d* transition metal surfaces and originates by the electronic charge redistribution resulting from the breaking of the translational symmetry and the reduced coordination at the surface, which moves the surface component to a lower binding energy[150].

The growing of the graphene layer results in a substantially unaffected Ir $4f_7/2$ core-level as evident in Fig. (3.4 right panel, red line). A very small change in the SCLS between the bulk and the surface components occurs, resulting in a SCLS = 533±5 meV. This indicates the almost non-interacting nature of the quasi-free standing graphene layer, in agreement with the literature[127,148]. In fact the lineshape of this core-levels is known to be highly sensitive to adsorbate and impurities on the surface[114,151], as for other transition metal surfaces[152].

3.4 Band structure

In Fig. (3.5) is reported the overall dispersion of the bands of graphene/Ir(111) obtained by performing scans throughout the surface Brillouin zone (SBZ) using UV photons from an Helium discharge source. In the upper panel we show the band map at photon energy of 21.2 eV (HeI) along the $\Gamma - M$ and the $\Gamma - K$ high symmetry directions of the SBZ. Due to the geometry of the experiment, a 30° rotation of the sample azimuthal angle is necessary to select these two directions, as depicted in the inset. In the bottom panel we show the ARPES map taken at 40.8 eV of photon energy (HeII) along the $\Gamma - K - M$ direction, performed at once by scanning the polar angle (by manipulator rotation). Due to the higher photon energy a wider momentum scan is achievable.

The dominant feature of the spectra is the π band, which has a bottom energy in Γ ($k_{\parallel}$=0 Å^{-1}) at 8.4 eV, a saddle point in M ($k_{\parallel}$=1.475 Å^{-1}, along the $\Gamma - M$ direction and $k_{\parallel}$=2.555 Å^{-1}, along the $\Gamma - K - M$ direction) at 2.7 eV and the well known linear dispersion at the K point (1.703 Å^{-1}). The red dashed line in Fig. (3.5, bottom panel) corresponds to first nearest-neighbour tight binding approximation[16–18] of the π band performed to better reproduce the behaviour around Γ and M. The fitting formula

$$E(\mathbf{k}) = \frac{\epsilon_{2p} + t\sqrt{f(\mathbf{k})}}{1 + s_0\sqrt{f(\mathbf{k})}}, \tag{3.3}$$

with

$$f(\mathbf{k}) = 3 + 2\cos(\sqrt{3}k_y a) + 4\cos(\frac{\sqrt{3}}{2}k_y a)\cos(\frac{3}{2}k_x a), \tag{3.4}$$

takes into account a possible shift in energy of the Dirac cone, through ϵ_{2p},

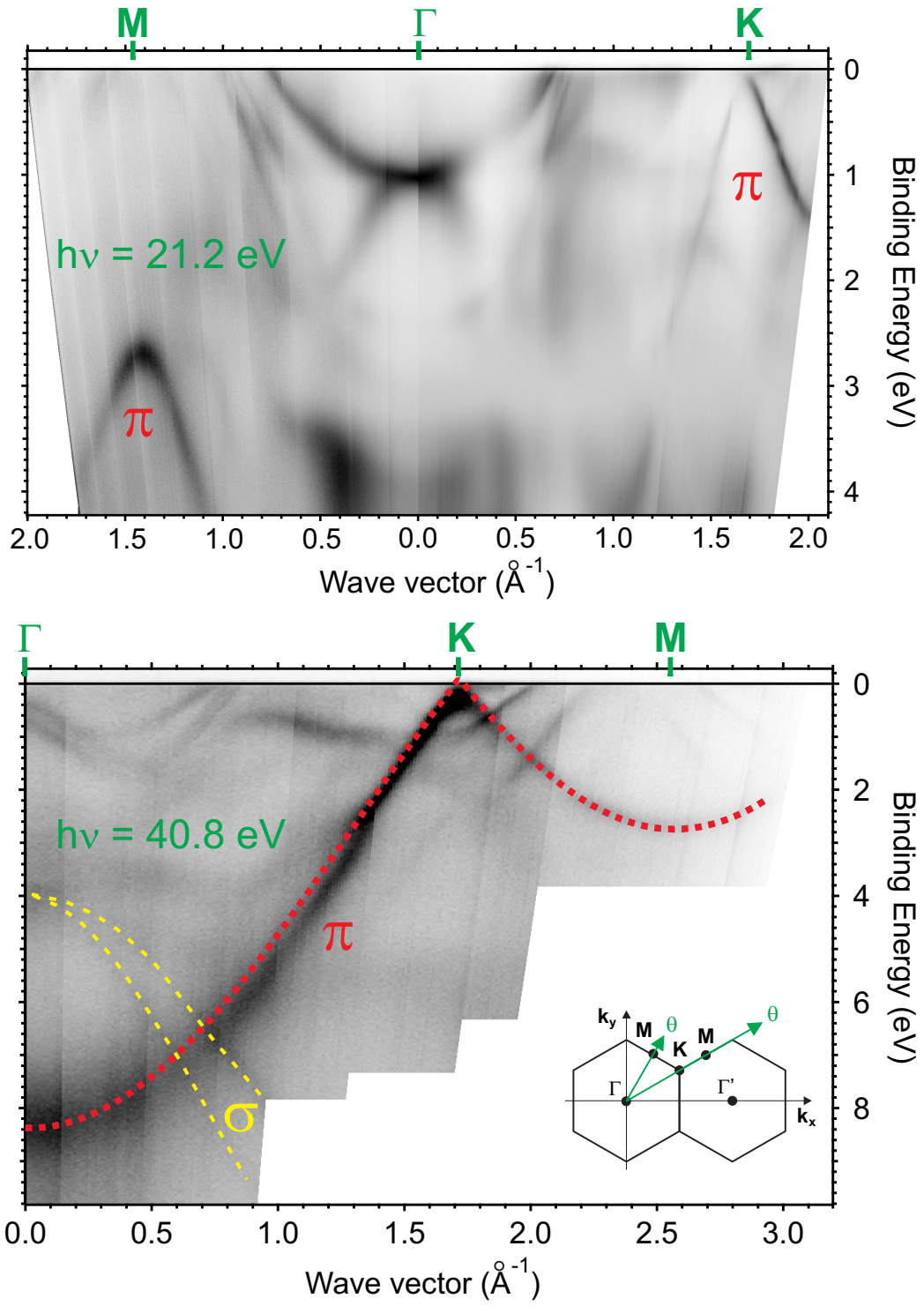

Figure 3.5: ARPES maps. Inset indicates how the ARPES scanning was performed. *Top)* MΓ-ΓK direction with HeI photon. *Bottom)* ΓKM direction with HeII photon showing the dispersion of the π band. Dashed red line shows the tight-binding calculation fit, discussed in the text.

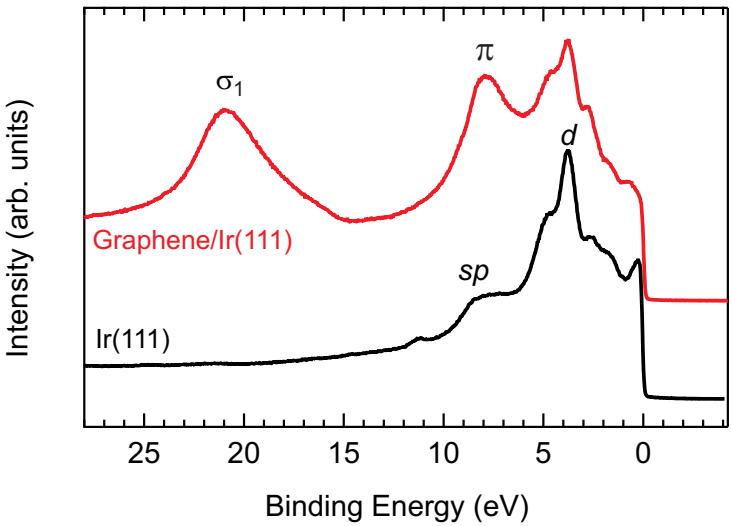

Figure 3.6: Valence-band photoelectron spectroscopy data for clean Ir(111) surface and graphene covered. $\pm 8^\circ$ angle-integrated data taken at normal emission, with hν=130 eV photon energy. The spectra are vertically stacked for clarity. The main feature of the spectra are indicated: sp and d band for Ir, σ_1 and π for graphene.

and an asymmetry with respect to the Fermi level, through s_0. a=1.42Å is the carbon-carbon distance in the graphene lattice. The resulting parameters (t=-2.85±0.05 eV, s_0=0.003±0.005 and ϵ_{2p}=0.10±0.02 eV) are in agreement with previous determination on the same system[125] and roughly correspond to a Fermi velocity v_F ≈9.2·10^5 m/s. We will study the Dirac cone more in detail in the next paragraph.

The other feature of graphene, the σ band has a low photoemission cross section and it is difficult to follow, however in the HeII spectrum (Fig. 3.5, bottom panel) it is possible to see the two σ_2 and σ_3 bands downward dispersing, degenerate at the Γ point at 3.9 eV (highlighted by yellow dashed line).

The third σ band is the deepest in binding energy and it is possible to observe it only with higher photon energy. The overall valence band structure angle-integrated ($\pm 8^\circ$) around normal emission (Γ) of bare Ir(111) and graphene/Ir at normal emission at high photon energy (130 eV) are compared in Fig. (3.6). Due to the angular integration, we are regarding a section around Γ of ≈ ±0.8 Å^{-1} at the Fermi level, in this way the peaks appear broadened, in particular if they are strongly dispersing. The bare Ir(111) spectrum is characterized principally by the *sp*-bulk band at 8.15 eV and the *d*-bulk band at 3.75 eV and many small features

at small energies, towards the Fermi level. The graphene layer preserves the overall characteristics of the underlying Ir bands, confirming the weak interaction between this two materials. Fingerprint of graphene are the main π and σ_1 bands at about 8 and 22 eV, respectively. The first one, together with the $\sigma_{2,3}$ bands at about 4 eV, as determined before, are accidentally degenerate with Ir bulk bands.

3.4.1 Dirac Cone

In Fig. (3.7 a,b) we report ARPES spectra corresponding to a high-resolution zoom of the graphene band map centred at the K point of SBZ of graphene ($k_\parallel$=1.703 Å^{-1}) taken at low temperature (L-N_2, T $\approx$ 80 K) with HeI and HeII photon energy, respectively. We can immediately recognize the expected linear dispersion of the Dirac cone.

The highly anisotropic intensity of the two branches of the Dirac cone, $\Gamma - K$ and $K - M$, is due to an interference effects of photoelectrons emitted by the two sublattices (A and B) generating the graphene honeycomb lattice[153–157], usually described in term of spinor wave functions, where the "pseudospin" indicates the sublattice. This pseudospin is responsible for graphene's many intriguing electronic properties: Berry phase of π[158], half-integer quantum Hall effect[58], Klein tunneling[23].

The anisotropy is enhanced along the $\Gamma - K - M$ direction, which corresponds to our experimental geometry (see inset in Fig. (3.5)), and in the ideal case one branch should completely disappear (*dark corridor*). We measure an intensity drop on the low-intense branch of 80%: this is a confirmation of the weakly interacting nature of graphene/Ir, which does not breaks the A-B symmetry. Recent polarization-dependent ARPES experiments have revealed that the position of the dark corridor depends on the polarization and energy of the incident photons[157,159–161].

A further confirmation of the high-quality graphene layer epitaxially grown on Ir(111) surface comes from the position of the Dirac point (that is the crossing of the two branches): by plotting the maxima of the electron distribution curve (EDC, Fig. (3.7 c)) we perform a linear fit of the two branches of the cone, their intersection at $k_\parallel$=1.703 Å^{-1} results $\approx$ 80 meV above the Fermi level,

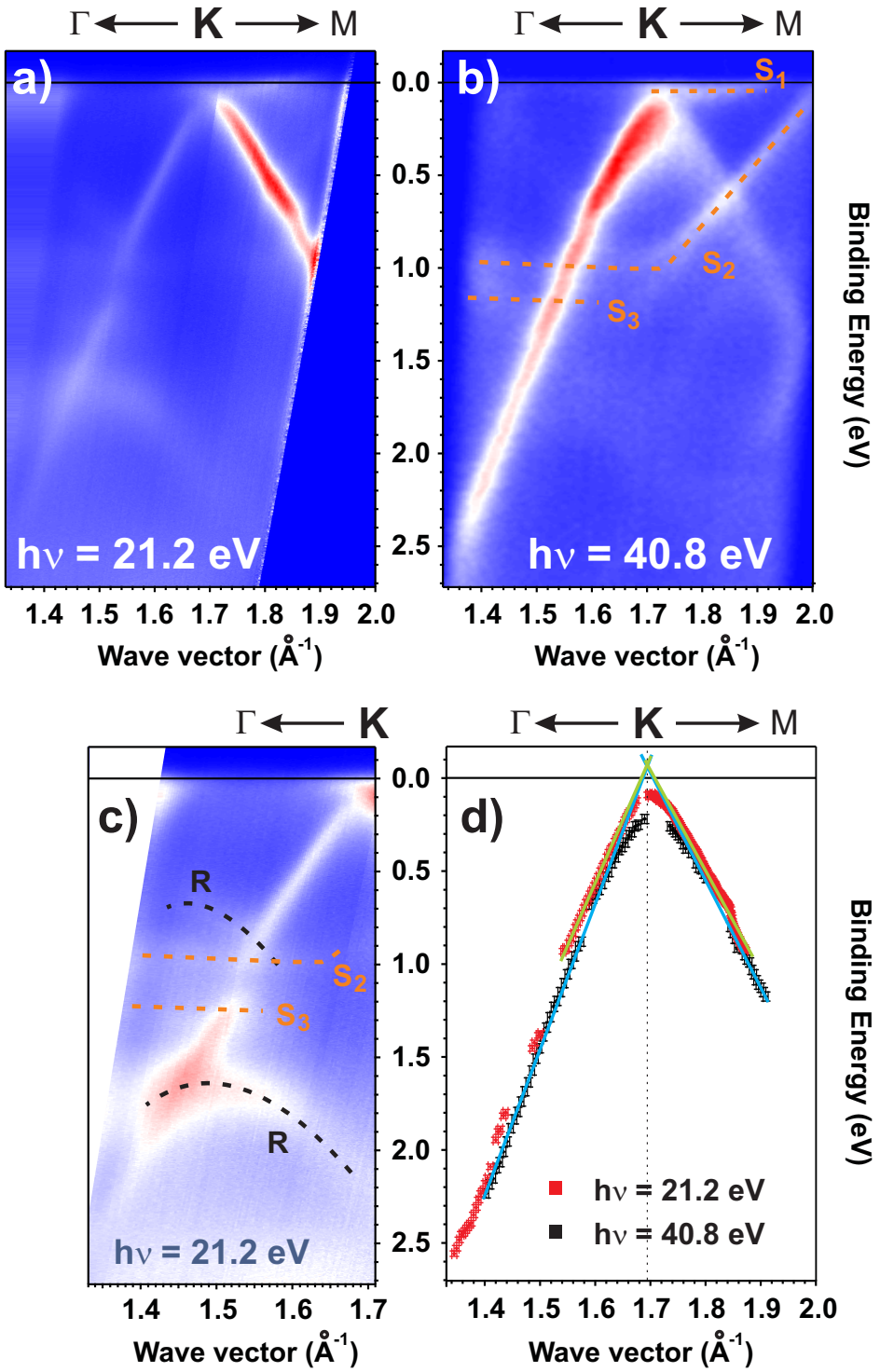

Figure 3.7: *Top)* HeI (left) and HeII (right) HR-ARUPS spectra centred at $k_{\|}$=1.70Å, the K point of the SBZ and scanned across the ΓKM direction. *Bottom)* (left) zoom on the ΓK branch of the Dirac cone taken with HeI photon, the surface states of iridium (S_2 and S_3) and two replicas of the Dirac cone (R) are marked in red. (Right) maxima of the Energy Distribution Curves (EDC) relative to the two top spectra, red dots HeI and black dots HeII. Linear fit of the branches are also reported.

Photon Energy	$v_{\Gamma K}$ (m/s)	v_{KM} (m/s)
21.2 eV	(9.0±0.5)·10^5	(8.0±0.3)·10^5
40.8 eV	(11.6±0.5)·10^5	(8.4±0.9)·10^5

Table 3.1: Fermi velocity extrapolated by linear fitting of the two branches of the Dirac cone.

causing a slightly p-doping of the graphene sheet ^{II}, in agreement with previous observations[40,162,163]. We remind that among the class of supported graphene, the epitaxial grown on iridium lead to a better quasi-free standing graphene than other substrates (see Section (1.1.2)).

Besides, the Ir(111) surface is one of the best surfaces for graphene growing also because the Dirac cone lies in a region coinciding with an energy gap in the Ir(111) electronic structure, hence almost free from bulk or surface states of the substrate[164]. Iridium surface state are however present but, due to the different cross section of carbon 2*p* states which is almost six times reduced in HeII with respect to HeI photon energy, they are more easily detectable in Fig. (3.7b). Therefore, due to different cross section, HeI spectrum better shows some of the most important characteristics of the corrugated graphene sheet: minigaps and Dirac cone replicas. As we can see in the zoom panel in Fig. (3.7c) minigaps arise along the linear branches of the Dirac cone, in particular at $\approx$ 1.0 eV BE in the $\Gamma - K$ branch and 0.7 eV in the $K - M$. These have been intensely studied and attributed to intersections with the Dirac cone replicas generated by the moiré superpotential which creates a series of mini-Brillouin zones (mBZ) centred around each K point, associate to the hexagonal lattice generated by the moiré basis vectors. Thus at the K points of this mBZ there will be replicas of the Dirac cone marked with R in Fig. (3.7 c), in according with literature[40,125].

By the linear fit of the two branches of the cone it is possible to estimate their slope (Fig. (3.7 d)), that is the quasiparticle velocity due to the relativistic behaviour of low energy electrons at the K point of the SBZ of graphene. The Fermi velocity so obtained are resumed in Tab. (3.1). The deviation from linearity near the Fermi level, observed in particular in the HeII spectrum, generates a kink at 0.7 eV BE, and it is attributed to the Ir 5*d* surface state S_1 which hybridizes with the graphene π band[162].

The asymmetry in the slope observed between the two branches is still con-

troversial, it may be attributed to the slight C-π/Ir-d hybridization[162] but it may also depend on the symmetry breaking of the two graphene sublattices due to the interaction with Ir substrate responsible of the moiré superpotential or even to the vicinity of the M point (in our experimental geometry).

3.4.2 Electron-phonon interaction

To evaluate the effects of possible electron-phonon interaction in graphene, we analysed the experimental data to extract information by means of two associated effects: the mass enhancement parameter and the FWHM of the Lorentzian Moment Distribution Curves (MDC).

In Section (2.2.1) we reported that these effects are related to the knowledge of the Eliashberg function, Eq. (2.17), and to the imaginary part of the self-energy, Eq. (2.18). By considering the relation that links the the bare dispersion $\epsilon(k)$ to the renormalized dispersion $E(k)$, $E(k) = \epsilon(k) + \Sigma(k, E)$, where k is the modulus of the momentum in a particular direction of the reciprocal space. In the case of graphene, the estimation of the parameter is highly simplified by the peculiar linear dispersion of the bands at the K point of the SBZ. Therefore the contribution due to the electron-phonon interaction manifest itself as a change of slope of the linear behaviour, hence a kink. By calling v_b the group velocity associated to the bare dispersion and v_{ph} to the renormalized, both near the Fermi level, we immediately obtain:

$$\lambda = \frac{v_b}{v_{ph}} - 1, \tag{3.5}$$

being the slope of the linear $E(k)$ dispersion proportional to the group velocity ($E = \hbar k v_g$). Thus the extraction of the mass enhancement parameter that a priori needs a detailed knowledge of the behaviour of the Eliashberg function with energy, is here simply obtained by the ratio between the two slopes of the Dirac cone.

On the same system (graphene/Ir) the electron-phonon coupling has been already evaluated, but after doping with potassium atoms[165]. This is necessary in order to avoid the inconvenience of the iridium surface state just below the Fermi level, the state S_1 in Fig. (3.7). However we report an analysis in agreement

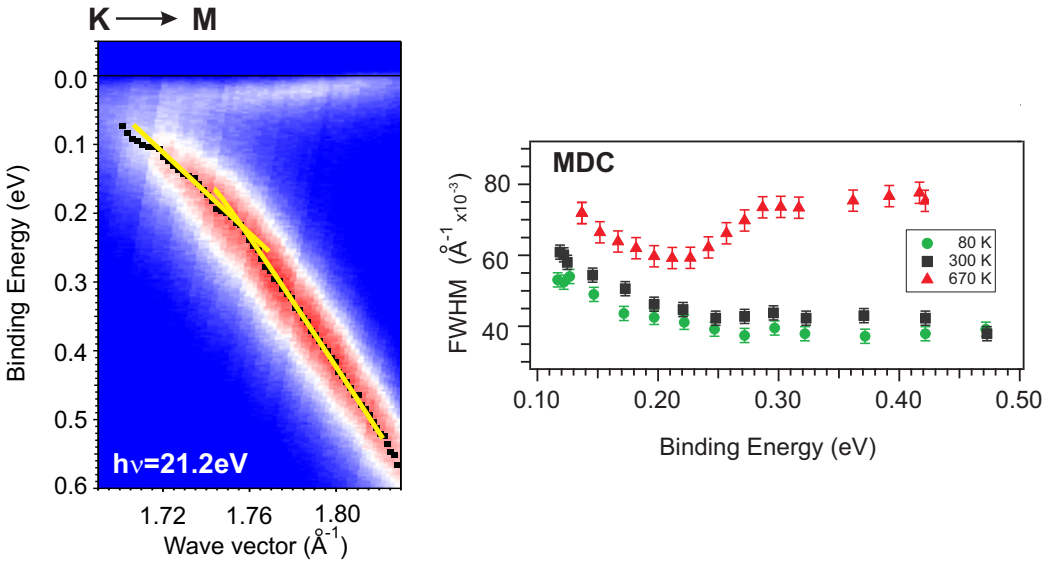

Figure 3.8

with Bianchi *et al.*[165] without doping the graphene.

The maximum energy expected for phonons in graphene is ≈ 200 meV[166]. We conducted our analysis on the high resolution cone acquired with HeI photon ($h\nu = 21.8\ eV$) at LN_2-temperature (≈ 80 K). Furthermore, due to the very high Debye temperature of graphene (above 1000 K[167,168], it is possible to extrapolate information even at non-zero temperature (where the mass enhancement parameter is rigorously defined).

In Fig. (3.8 left panel) we show the highly intense branch of the Dirac cone along the direction K-M whit the superimposition of the peak position in MDC cuts: we can note a change in the slope at about 0.2 eV BE, corresponding to a mass enhancement parameter $\lambda = 0.3 \pm 0.1$; the large error is due to the difficulty in the estimation of the low-energy slope due to the presence of the Ir surface state. This result is however in agreement with previous determination[165,169].

A further analysis that can be conducted concerns the behaviour of the FWHM of the MDC curves in function of the temperature, this is linked to the imaginary part of the self-energy Σ''. At zero-temperature, where only the phonon emission is allowed, and not the absorption, the behaviour expected is an increase of the FWHM until an energies close to the Debye energy. For T≠0 also phonon absorption is possible, thus an overall increase in the value of the

FWHM happens.

The result of the fits conducted for three temperatures (80 K, 300 K and 670 K) is shown in Fig. (3.8 right panel). Due to the presence of the Ir surface state, we analysed only data for BE higher than 0.1 eV, the effects of this state is however still evident, in fact the FWHM value is decreasing at the beginning, on the contrary of what expected. The excited phonons at RT (300 K) are negligible, while at 670 K the phonon absorption is more evident and only at this temperature we can see the expected decrease in the FWHM starting from the Debye energy at about 260 meV.

These results are another confirmation of the high quality of the graphene sample and an easy support to analyse electron-phonon coupling in systems with a linear band dispersion near the Fermi level.

3.5 Conclusions

The Ir(111) has revealed a good substrate for minimizing the graphene-substrate interaction, while maintaining a structural constraint, thus leading to a quasi-free standing graphene single-layer. The small mismatch between the graphene and the (111) surface lattice produces a highly-ordered hexagonal modulated moiré superstructure with a high degree of structural order with a 2.5 nm hexagonal periodicity. As a consequence of the small interaction, a slight hole doping is observed. The moiré structure can thus be exploited as a template to fabricate unique bidimensional molecular networks.

Furthermore, we demonstrated an extremely high stability and low degree of degradation of supported graphene even after air-transport among laboratories, whose high-quality recovering after the first preparation can be perfectly achieved by medium-temperature (up to about 900 K) annealing cycles in ultra-high-vacuum.

Chapter 4

MPcs on graphene: growth morphology and interaction

In this Chapter we investigate the adsorption of metal-phthalocyanines on graphene by means of absorption and photoemission spectroscopy. We will clarify the role of the graphene as a buffer layer and the influence of the metal-phthalocyanine adsorption on the graphene band parameters, concentrating on the electronic structure of the molecular macrocycles. Comparing the thin film absorption and photoemission spectra with the single layer it is possible to investigate the interaction of the macrocycles-located states with the substrate. The adsorption geometry of the single layer and the growth of subsequent layers depends on the balance between the molecule-molecule and the molecule-substrate interaction.

4.1 Nucleation and growth of thin films

Epitaxial growth of thin films on a solid surface, e.g. a semiconductor or a metallic surface, is one of the important techniques in semiconductor technology. Many studies have been done in recent decades for better understanding the growth mechanism and related conditions[170,171].

Generally, three kinds of crystal growth morphology on surfaces are classified[172] and here illustrated schematically in Fig. (4.1):

- Volmer-Weber mode is an island growth in which the interaction between

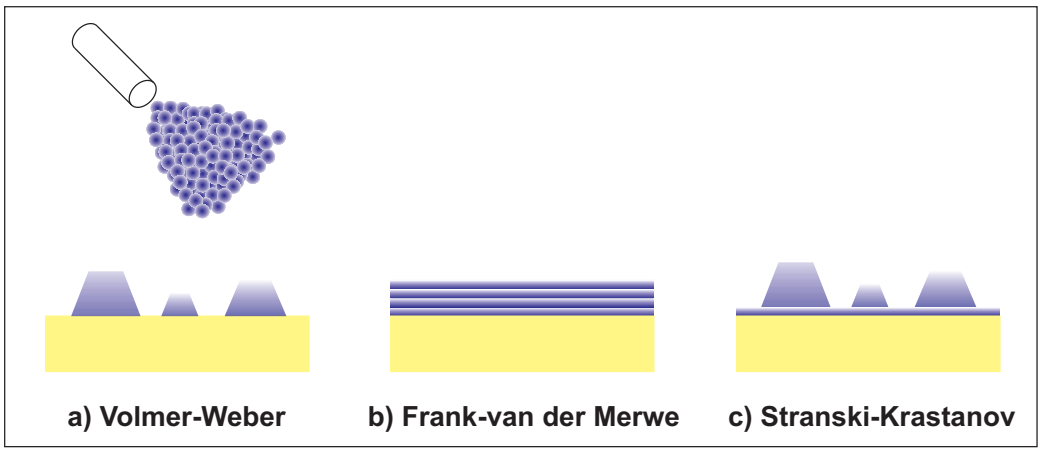

Figure 4.1: A schematic of the three possible growth modes: a) Volmer-Weber, islands; b) Frank-van der Merwe, layer-by-layer; c) Stranski-Krastanov, layer-plus-islands.

the adsorbing molecules is higher than that with the substrate which plays here mainly an inert role; thus the molecules are free to diffuse on the substrate surface nucleating in small clusters and then grow into three-dimensional islands.

- Frank-van der Merwe mode is the opposite to the previous one, in this case the interaction with the substrate is strong enough to prevent the molecules to diffuse, limiting the clustering and favouring in this way an uniform layer-by-layer two-dimensional growth.

- Stranski-Krastanov mode is an interesting intermediated case; after the completion of the first monolayer (or more), whose structure is strongly influenced by the underlying substrate, subsequent layer growth is unfavourable and islands start to nucleate on top of this intermediate layer (layer plus islands), in this case the role played by the substrate is intriguing.

It has to be underlined that one of the parameters which plays the difference among them is the relative interaction between molecules and substrate by one side and between the molecules themselves, and the role of the substrate for ordering the molecular adsorption: these are the keys arguments of this Chapter and, in general, of this Thesis.

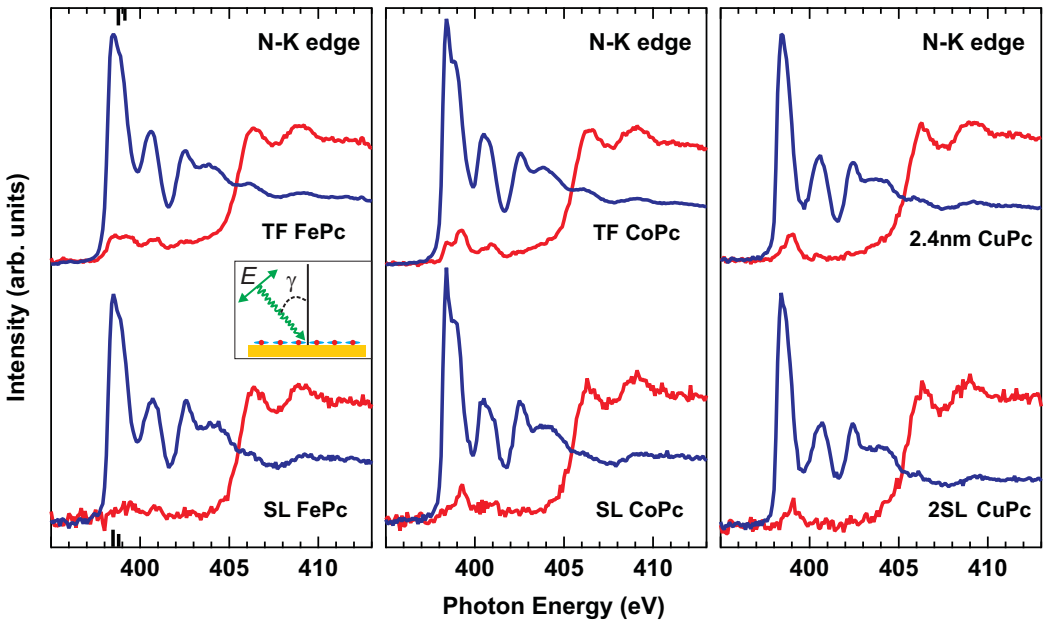

Figure 4.2: Angular dependent NEXAFS across the N K-edge for FePc (SL and TF), CoPc (SL and TF), CuPc ($\approx$ 2 SL and 2.4 nm) adsorbed on graphene/Ir(111). Red curves correspond to γ=0° and blue curves correspond to γ=70°, where γ is the angle between the incident photon and the surface normal, as reported in the sketch in the inset.

4.2 K-shell absorption edge

Information on the adsorption properties of MPcs on graphene can be obtained by the absorption spectroscopy at the relevant edges. The analysis of K-shell absorption edge of carbon and nitrogen can give information on the interaction of the molecular macrocycles with the substrate.

Both C and N K-edges are taken with linearly polarized radiation, in condition of in-plane and almost out-of-plane excitation. The linear polarization dichroism, gives a probe on the spatial orientation of the empty orbitals with respect to the impinging photon polarization, thus it is useful to determine the molecular orientation and hence the growth morphology on the surface.

4.2.1 Nitrogen K-edge

In Fig. (4.2) the nitrogen K-edge data for the SL and TF* of FePc and CoPc and $\approx$ 2 layes and 2.4 nm of CuPc grown on graphene are presented.

*For a thin film (TF), we consider in this thesis a 5 nm-thick film, unless otherwise specified.

Due to small differences between them, the absorption features can be discussed together.

The N K-edge absorption fine structure presents a first resonance at about 398.4 eV photon energy, constituted by two close structures due to photoexcitation from the 1*s* level of the N_1-isoindole and N_2-azomethine nitrogen atoms in the pyrrole ring to the LUMO of π*-symmetry. The higher-energy structures at 400.6, 402.5, and 404.0 eV photon energy are due to transitions to higher-lying unoccupied states mainly involving the pyrrole ring[173], in agreement with the attribution given for FePc and CoPc planar TF prepared on other substrates[174]. The in-plane excited spectra are characterized by broader features at 406.4 eV and 409.0 eV related to $1s \rightarrow \sigma$* molecular orbitals transitions.

As it concerns the N K edge lineshape, it does not present any significant change between the SL and the TF spectra, indicating the unperturbed distribution of resonance states in the macrocycles, confirming a negligible interaction with the underlying graphene and iridium surfaces. In the next Chapter we will see that the adsorption of a SL of FePc on the bare Ir(111) surface influences the absorption lineshape, indicating an FePc/Ir interaction.

The black ticks in the energy axes represent the BE position of the N $1s$ core-levels measured by photoelectron spectroscopy (see Section (4.4)), whose BE is higher than the corresponding absorption peak photon energy, indicating an excitonic effect in the molecular layer, which is still present for the FePc-SL on graphene.

4.2.2 Carbon K-edge

In Fig. (4.3) the carbon K-edge data for the SL and TF of FePc, CoPc and CuPc. With the same assumptions made for the N K-edge, we will discuss of them altogether.

At low molecular coverage the spectra are dominated by the strong C K-edge signal coming from the graphene carbon atoms, already discussed in Section (3.2). This spectrum is reported as shaded area superimposed to the data of the SL to better single out the differences and the new signals coming out.

At the completion of the first molecular SL, the well defined σ structures of graphene at 291.8 eV and 292.8 eV are lowered and less defined, while new higher

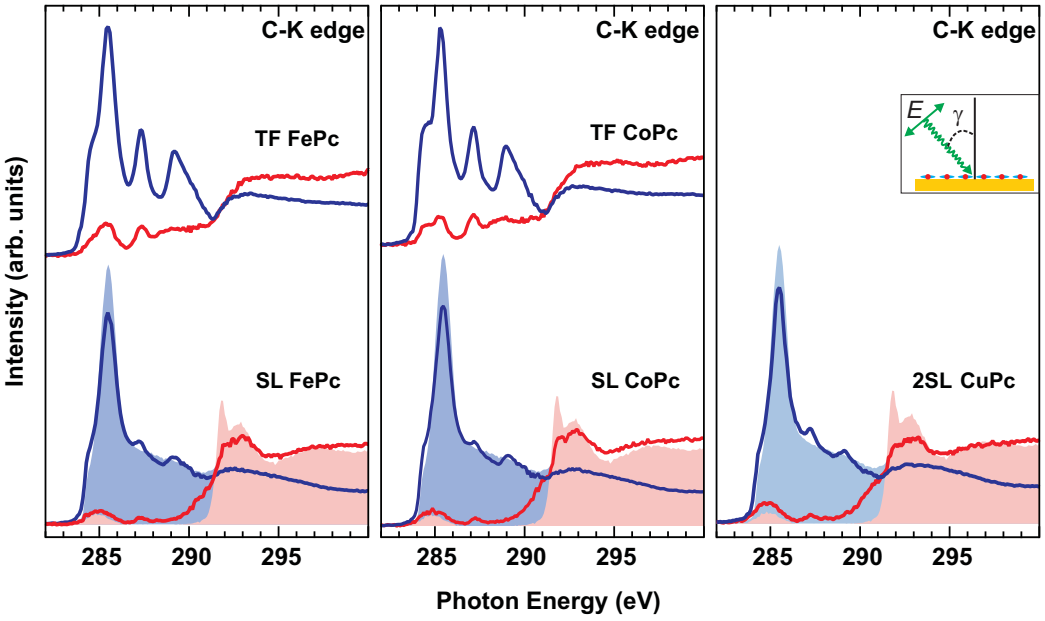

Figure 4.3: Angle dependent NEXAFS across the C K-edge for FePc (SL and TF), CoPc (SL and TF), CuPc ($\approx$ 2SL) adsorbed on graphene/Ir(111). Red curves correspond to γ=0° and blue curves correspond to γ=70°, where γ is the angle between the incident photon and the surface normal, as reported in the sketch in the inset. Shadowed and superimposed to each SL spectra is reported the C K-edge absorption spectrum of clean graphene of Fig. (3.2) at the respective angles.

energy features emerge on the out-of-plane excited spectra at 287.3 eV, 289.2 eV and 290.5 eV which evolve and become dominant only when the molecular TF is formed. Since the first unoccupied levels in the MPc molecule is formed by π* states mainly delocalized on the pyrrole macrocycles containing both C and N atoms, they are available for transitions from both the C and the N 1*s* initial states, thus both K-edges present similar structures and line shapes at the MPc thin-film stage, when the graphene contribution to the C K-edge is negligible. This is in general due also to the charge delocalization of molecular orbitals on the π-conjugated ligand macrocycle. Thus the discussion made for the N K-edge leaves to the same conclusions for the C K-edge of a MPc TF: as in the case of nitrogen K-edge, the first two features at the edge ($\approx$ 284.6 eV and 285.4 eV) can be respectively attributed to the excitation from the 1*s* core shell of the benzene and pyrrole carbon (C_B and C_P) to the π* character LUMO states, here the chemical shift is higher and we are able to see two distinct peaks.

Due to the difficulty caused by the presence of the strong graphene signal, in this case the binding energy of the molecular carbon peaks was not reported.

In conclusion, the empty states localized on the ligand macrocycle seems not strongly influenced by the interaction with the substrate.

4.3 MPcs on graphene: growth morphology

In this paragraph we will go deep into details with the adsorption of a SL of FePc on graphene. We show in Fig. (4.4) the LEED pattern before and after RT deposition of the first SL-FePc on the graphene/Ir(111) template. The C_g- and Ir- related spots arranged in the concentric circles of the hexagonal structure are still present, indicating persistence of the moiré superstructure after FePc deposition. There is a smooth background superimposed to the spot pattern, probably caused by some disordered molecules. The inner and outer spots characteristic of the superstructure maintain their distribution and relative distances, thus demonstrating that the first SL adsorption of FePc does not destroy or modify the moiré periodicity.

As we report in the first Chapter, recent STM experiments on the moiré template obtained for graphene/Ru showed formation of ordered structures of FePc molecules lying into graphene depressions[93,96], with the formation of a

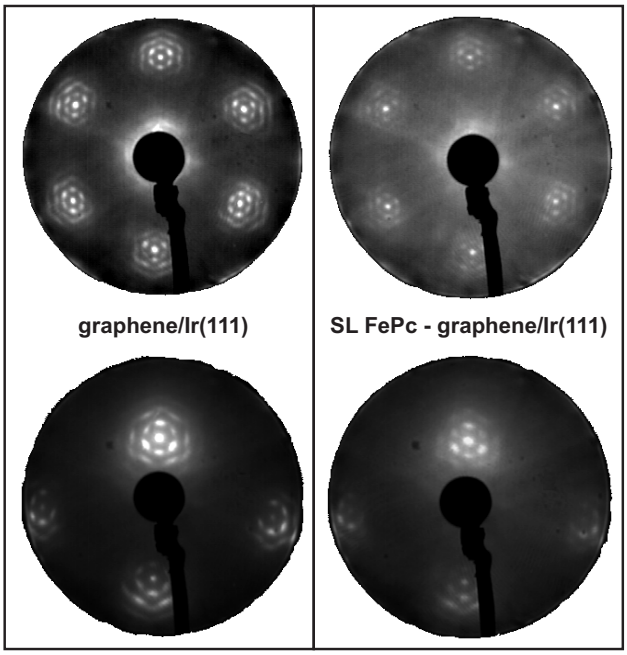

Figure 4.4: (*Left panel*): LEED pattern of the graphene single-layer on Ir(111), showing the typical moiré pattern. Top) $E_p = 142$ eV, and bottom) $E_p = 70$ eV with the surface sample non orthogonal to the beam to show the (0,0) spot. (*Right panel*): LEED pattern of the single-layer FePc/graphene/Ir(111) interface. Top) $E_p = 141$ eV, and bottom) $E_p = 70$ eV with the surface sample non orthogonal to the beam to show the (0,0) spot. LEED patterns taken with the sample kept at liquid nitrogen temperature.

supramolecular kagome lattice. A larger corrugation has been detected on graphene grown on top of Ru(0001) as compared to Ir(111), as discussed in Sec. (1.1.2), in fact very recent studies on CoPc/graphene/Ir(111)[175,176] determine both close-packed single layer adsorption, hence driven by molecular-molecular interaction, and the moiré driven formation of kagome supramolecular lattice. This subtle balance is determined by coverage and temperature.

In order that FePc molecules adopts an analogous configuration on the graphene/Ir(111) template, a requirement needed is that the molecules lay flat on the moiré superstructure.

4.3.1 Molecular orientation

In order to determine the FePc angular orientation on the graphene surface, we performed an angular resolved NEXAFS experiment across the N K-edge on the FePc-SL on graphene/Ir(111), by changing the angle between the electric field vector and the surface plane [I], as shown in Fig.(4.5). In particular, NEXAFS data have been taken exploiting the symmetry properties of the π^* and σ^* levels assessed by the electrons photoexcited from the N 1*s* core-levels, by using linearly polarized radiation, with the electric field vector either parallel or quasi-normal to the crystal surface plane. There is a clear dichroic signal: the dichroism at the N K-edge, with distinct polarization dependence on the π^* and σ^* resonances, is a clear evidence of a planar orientation of the FePc molecules at the SL and for the molecular film.

Within the dipole approximation, the integral intensity I(π^*) depends on the orientation of the electrical field vector **E** of the incident photon beam with respect to the transition dipole moment vector **T**[106]. In the aromatic molecules like FePc, the π^* states can be treated like vectors normal to the aromatic ring planes, and I(π^*) as a function of the linearly polarized radiation can be written as I(π^*) $\propto \cos^2\delta$, where δ is the angle between the radiation polarization and the vector orbital. According to our experimental geometry, this can be written as[106]

$$I(\pi^*) = A[P \cdot I^{\parallel} + (1 - P) \cdot I^{\perp}], \tag{4.1}$$

where A describes the angle-integrated cross section, $P = 90\%$ is the estimated fraction of linear polarization at the SuperESCA undulator, $I^{\parallel}$ and $I^{\perp}$ are two

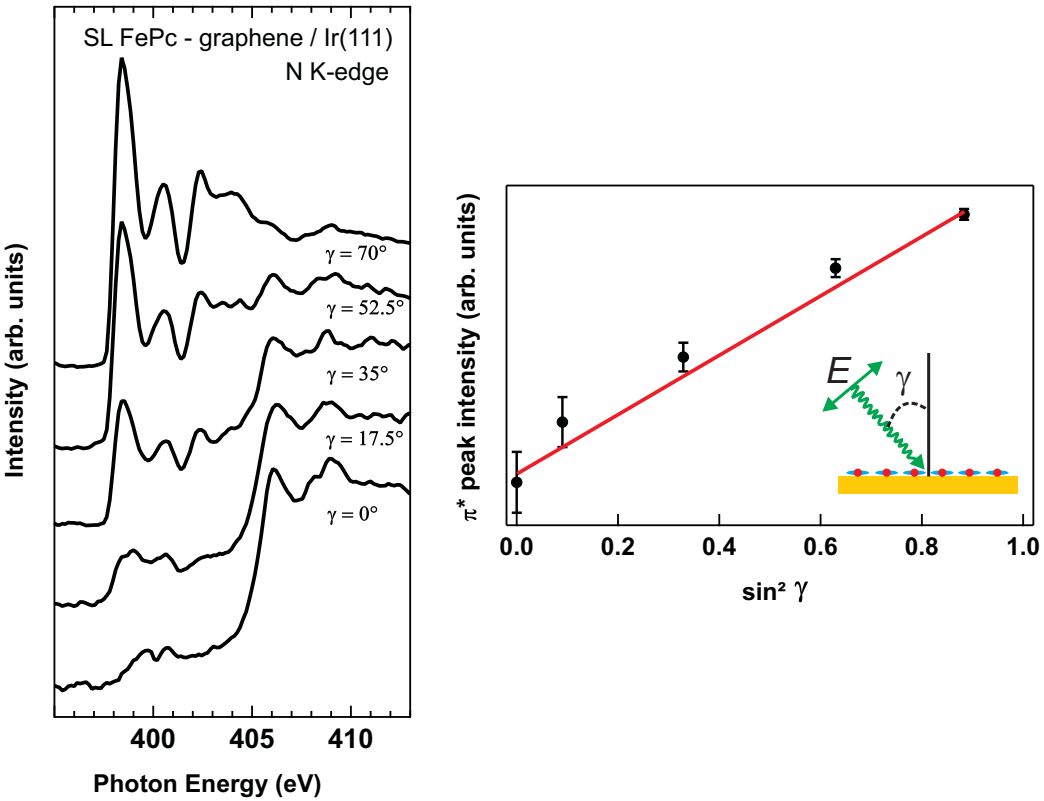

Figure 4.5: *Left)* NEXAFS at the N K-edge for the SL-FePc/graphene/Ir(111) system. Data taken at different incidence angles γ, as specified in the sketch within the figure. *Right)* Normalized π* resonance intensity, as a function of the square sine of the angle γ. The line corresponds to a leastsquares fit according to Eq. (4.1), giving a tilt angle $(8 \pm 10)^\circ$ between the molecular axis and the surface normal, demonstrating that the FePc molecules are flat on the graphene surface.

angle-dependent quantities function of the angle α between dipole moment **T** and the surface normal; γ is the angle of incidence, and ϕ is the azimuthal orientation of the molecular orbital vector **T** with respect to the direction of incidence of the radiation. For the graphene substrate of threefold symmetry, the azimuthal dependence averages to a constant, and the expressions for the angular-dependent intensities reduce to[106]:

$$I^{\parallel} = cos^2\delta cos^2\alpha + \frac{1}{2}sin^2\delta sin^2\alpha$$

and

$$I^{\perp} = \frac{1}{2}sin^2\alpha.$$

The main peaks in the π^* region have been fitted with pseudo-Voigt functions, after subtraction of an integral function approaching the atomic background at high photon energy. In the least squares fitting procedure, all relevant parameters except the integrated intensity of each component have been kept fixed upon polarization angle variation. The result of the fit shown in Fig. (4.5 right panel), taking into account the overall experimental and fitting errors, gives an angle of $(8\pm10)^\circ$ of the FePc molecule with respect to the graphene plane. Thus, we definitely obtain flat-lying FePc molecules onto the moiré superstructure formed by graphene/Ir(111)^I.

Even if not studied in such details, the higly dichroic NEXAFS signal of CoPc and CuPc (see Fig.4.2) suggests the same conclusion for these other two metal-phthalocyanines grown on the same substrate.

This result is in agreement with recent experiments of MPcs adsorption on graphene grown on different substrates[92,93,96,97,175,176] and with previous experiments of FePc[177], CuPc[178] and NiPc[179] adsorption on highly-oriented pyrolitic-graphite (HOPG). Although in principle one could expect an analogous adsorption process, since graphene is a single sheet of graphite, we have to consider the morphology of the substrate, as we will deepen in the next Chapter. The conclusion that MPcs adsorb flat onto graphene on Ir(111) is important in establishing the almost free-standing nature of the graphene sheet, despite its corrugation. We also notice that several metal-phthalocyanines adsorb in a flat-lying configuration on single crystalline Au and Ag surfaces[173,180–184], where a strong bonding takes place.

4.4 Core level photoemission

Core-level spectroscopy can unravel the element-specific interaction of the molecule with graphene and the underlying metal. The contribution due to the macrocycles ligands of FePc, CoPc and CuPc has been deduced from the C and N 1*s* core-level photoemission signals, while the influence on the metallic substrate from the Ir 4*f* core-levels. The spectra were collected at the SuperESCA beamline at a photon energy of 400 eV (C), 500 eV (N) and 136 eV (Ir) at normal emission.

Ir 4f$_{7/2}$

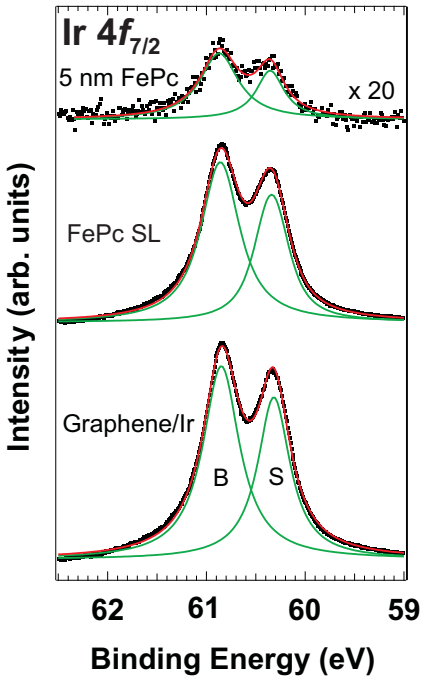

Figure 4.6: XPS data of the Ir $4f_{7/2}$ core levels for (from bottom to top) clean graphene/Ir(111), SL and TF-FePc/graphene/Ir(111) system. Experimental data (dotted lines) with Shirley background subtracted and peaks resulting from a least-square fitting procedure (continuous lines).

As already discussed in Sec. (3.3), the Ir $4f_{7/2}$ core-level of the graphene/Ir(111) surface presents two main peaks attributed to a bulk and a surface component, at 60.850 eV and at 60.317 eV BE, and with 0.452 and 0.398 eV full-width at half-maximum (FWHM), respectively, as deduced by a least-square fitting-analysis using quasi-Voigt (gaussian-lorentzian) lineshape, taking into account intrinsic lifetime and experimental resolution. The Ir $4f_{7/2}$ surface core-level shift (SCLS) between the bulk and the surface components for graphene/Ir is of 533$\pm$5 meV.

The adsorption of the first FePc-SL produces a slight decrease of the surface peak intensity with respect to the bulk component by 2.5%, and a further reduction of the SCLS by 14$\pm$5 meV with respect to the clean graphene/Ir surface, thus resulting 519$\pm$5 meV. On the contrary, adsorption of FePc molecules directly on the Ir(111) surface causes a quenching of the $4f_{7/2}$ surface peak, already at low molecular density, see Sec.

(5.3.1). The tiny SCLS modification (ΔSCLS/SCLS=2.6%) upon FePc adsorption is of the same amount of that found when the graphene sheet is prepared on Ir(111) with respect to the bare Ir surface (Sec. (3.3)). This evidence suggests a negligible influence of FePc molecules on the buried graphene/Ir(111) interface, with the graphene sheet basically decoupling the Ir surface from the FePc molecular layer. Eventually, when a 5 nm-thick thin-film of FePc is grown (topmost spectrum), the Ir $4f_{7/2}$ double peak is still visible. Thus, we can assume that the graphene sheet basically decouples the Ir surface from the FePc molecular layer. We observe the same behaviour for the SL of the other metal-phthalocyanines studied (CoPc and CuPc).

Recent high-resolution electron-energy loss-spectroscopy data on MPcs adsorbed on graphene/Ni(111) observed an energy and lineshape variation of the molecular vibrational modes for FePc and CoPc with respect to CuPc, suggesting an interaction of the Fe- and Co-related levels with the Ni states underlying graphene[97]. In the present case we do not have evidence of MPc interaction with the underlying Ir surface, because of the much lower C-Ir interaction with respect to the C-Ni interaction (see Section (1.1.2) in the graphene layer supporting the MPc molecules.

C 1s

The typical photoemission spectrum from the carbon 1*s* core level for a thin film of MPc is characterized by two principal features, corresponding to benzene and pyrrole carbon atoms and by furthere satellite peaks. In Fig. (4.7, left panel, top spectrum) the C 1*s* spectrum of the 5 nm-thick FePc TF is presented. The fit has been performed with five Voigt-profiled components and with a small residual component due to the underlying graphene signal, after subtraction of a Shirley background. The components due to the carbon atoms in the benzene rings (C_B) and in the pyrrole rings (C_P) are at 284.46 and 285.85 eV BE, respectively, with a relative shift of 1.39 eV. The smaller features are associated to their relative shake-up satellites (S_B and S_P), due to the transition from the highest-occupied to the lowest-unoccupied molecular orbital (HOMO-LUMO) at 286.31 and 287.84 eV BE, respectively, and to the excitation of a vibrational mode for carbon atoms belonging to the benzene rings (V_B) at 284.83 eV. The fit

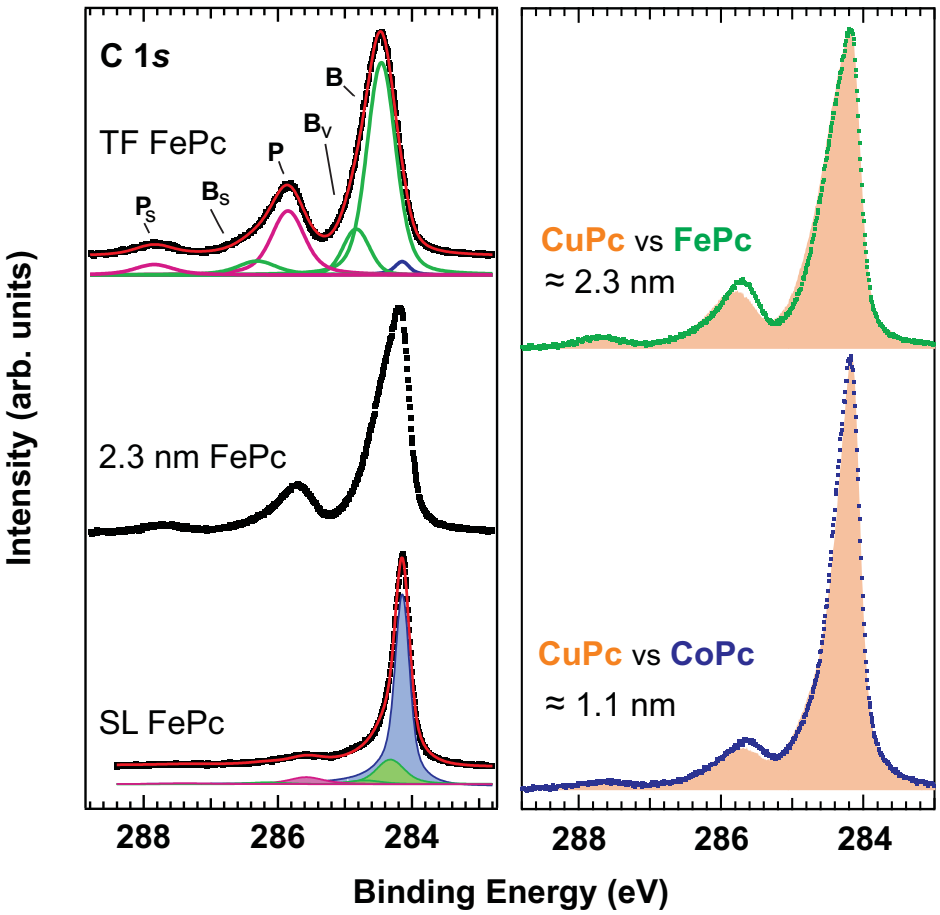

Figure 4.7: X-ray Photoelectron Spectroscopy (XPS) data of the C 1*s* core levels for the MPc/graphene/Ir(111) system. *Left)* spectra at increasing FePc coverage (from bottom to top). Experimental data (dotted lines) and peaks resulting from a least-square fitting procedure (continuous lines). Fitting peaks of C 1*s*: blue for graphene C, green for benzene-related C_B and purple for pyrrole C_P. *Right)* comparisons at different coverage for CuPc (shadowed), CoPc and FePc (dotted) spectra. Spectra vertically stacked for clarity.

procedure is in agreement with previous data[180,185].

At the FePc SL coverage, the core-level lineshape is dominated by the graphene C 1*s* component, superimposed on the molecular components. In the best-fitted C 1*s* spectrum, the graphene component is found at 20±10 meV higher BE value than on the graphene/Ir(111) surface, whereas all the molecular components are shifted to lower binding energies with respect to the thin film by about 0.15 eV. This latter core-level energy shift can be due to concomitant effects which will be discussed later.

In particular, at the SL, the C_B and C_P components appear at 284.32 and 285.58 eV, exhibiting a relative BE shift of 1.26 eV. Within the limits of the experimental uncertainty, the separation between the main peaks and the respective satellites does not change, upon varying the FePc layer thickness. The C_B-C_P BE reduction from the TF to the SL (from 1.39 eV to 1.26 eV) is probably due to a slight molecular deformation[II]. A comparable reduction of the C_B-C_P energy shift observed for FePc adsorbed on highly-oriented pyrolitic-graphite (HOPG)[177] and ascribed to polarization effects. However, the absence of satellite screening in the N (see later) and C 1s core levels suggests a lower influence of the polarization effect. A slight modification in the molecular configuration when FePc is adsorbed on graphene can be the reason of the C_B-C_P energy shift produced by angular deformation of the macrocycles and consequent molecular distortion, as also observed for MPcs adsorbed on semiconductor[186] and metal surfaces[88,187,188].

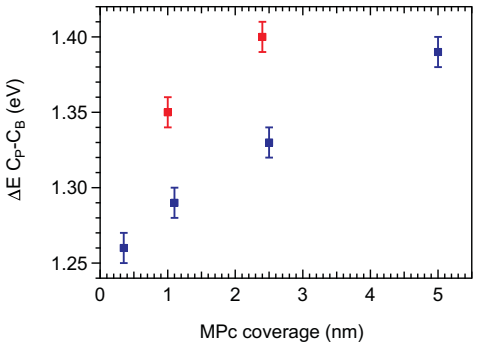

Figure 4.8: Plot of C_B-C_P in function of the coverage of CuPc (red) and FePc (blue) adsorbed on graphene/Ir(111), as deduced from the fitting analysis of C 1*s* spectra. CoPc has the same trend of FePc.

The analysis conducted so far is valid also for the adsorption of CoPc. In fact, FePc and CoPc C 1*s* core level spectra as a function of the molecular coverage have the same lineshapes. Nonetheless subtle differences can be individuated in Fig. (4.7, right panel) where a comparison with CuPc spectra is reported. The most important difference is in the C_B-C_P energy shift, reported in Fig. (4.8):

while FePc and CoPc have the same behaviour, starting from a lower value of the C_B-C_P and then reaching the TF value (1.39 eV) for higher coverages, CuPc shows a minor energy difference, reaching the TF value at lower coverages. Within the view of the molecular deformation at the interface, this result can be viewed as a minor deformation for the CuPc molecule at the SL stage. An alternative view could be that proposed by Grobosch *et al.*[189] who report a reduction of the C_B-C_P energy difference for FePc and MnPc with respect to more 3*d*-filled Pc as Co Ni Cu and ZnPc. The authors attribute this shrinking in the binding energy difference to the higher degree of hybridization of benzene orbitals with the 3*d* like metal orbitals in the less filled MPcs. However this picture does not explain the energy difference as a function of the coverage, but questions the role of the 3*d* central metal atom which will be discussed later. A similar effect on the pyrrole carbon of CuPc molecule has been observed for CuPc adsorbed on the Au(110) surface by Evangelista *et al.*[185] where the binding energy difference between carbon atoms located in benzene and pyrrole rings is 1.4 eV at all adsorption phases. This was attributed to a lack of charge transfer between the molecules and the underlying Au substrate.

Furthermore, C 1*s* core level spectra, due to the superposition of signal coming from the molecule and the graphene surface, are a very good tool to estimate the molecular coverage onto the graphene sheet, by evaluating the intensity ratio of the specific fitting components. In particular, at the SL the graphene peak has an area equal to the 67% of the total fitting area. Since a moiré unit cell is 10×10 larger than the graphene unit cell, which contains two atoms, we have 200 graphene-C atoms within a moiré unit cell. The ratio found for the area corresponds to an equivalent of $\approx$ 98 MPc-C atoms *per* moiré unit cell, since each MPc molecule contains 32 C atoms, hence there are 3 flat molecules covering a moiré unit cell[I]. An uniform coverage of adsorbates should correspond to $\approx$ 4 molecules *per* unit cell, our findings suggests that there are regions of the graphene layer, within a moiré unit cell, that remains uncovered, confirming the STM observations on similar systems[93–96,176].

N 1s

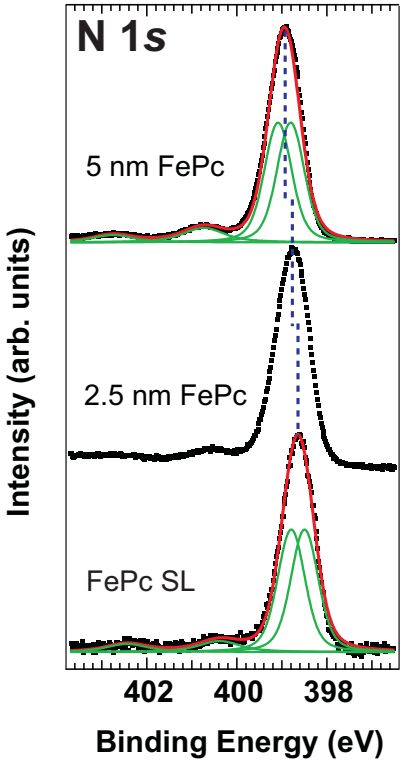

Figure 4.9: XPS data of the N 1*s* core-level at increasing FePc coverage (from bottom to top). Experimental data (black dotted lines) and peaks resulting from a least-square fitting procedure (continuous lines). The dotted line is a guide to eye to follow the shift in energy of the peak's centroid.

In Fig. (4.9) the N 1*s* core level spectra in function of the FePc coverage are reported. We choose to show only FePc because there are no important differences among the three MPcs investigated. The nitrogen 1*s* core level spectrum for the FePc 5 nm-thick TF (top spectrum) is due to the photoexcitation from the two non-equivalent nitrogen atoms (N_1 and N_2) in the pyrrole rings and in the bridge position, associated to the N_1-isoindole and N_2-azomethine atoms. We fit the core-level for the TF with a double peak and with two broad shake-up satellites structures at higher BE, resulting in two main peaks at 398.81 and 399.09 eV BE, and two shake-up satellites at 1.79 eV and 3.80 eV higher BE with respect to the first peak, in agreement with the literature on MPcs[185–187].

As the number of inequivalent nitrogen atoms is the same for both positions, we impose a 1:1 intensity ration between the two main peaks during the fitting procedure. The FWHM is slightly larger (0.72 eV) than the C 1*s* components.

At completion of the first SL FePc on graphene/Ir, the N 1*s* lineshape does not significantly change with respect to the FePc TF, while a broader structure is observed when FePc is adsorbed directly on the Ir(111) surface [II], see Sec.(5.3.1). There is only a continuous energy shift towards lower BE as a function of coverage, by 0.12 eV (SL with respect to 2.5 nm) up to 0.31 eV (SL with respect to 5 nm), also for the shake-up satellites, higher with respect to that observed before for the C 1*s*. This energy shift can be attributed both to a band

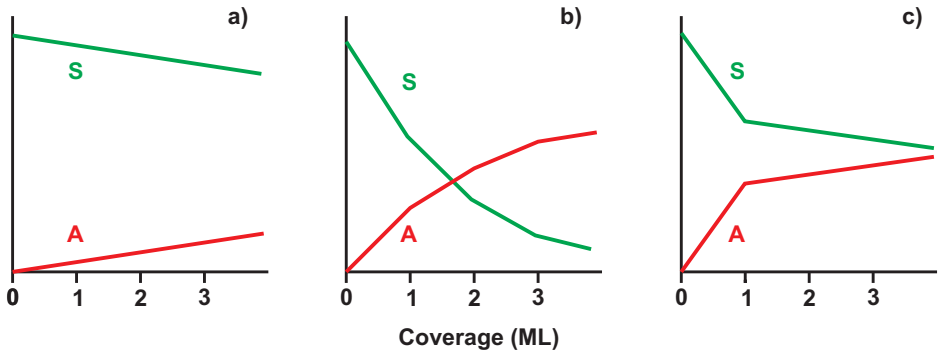

Figure 4.10: Schematic intensity plot in function of coverage from the substrate (S) and the adsorbate (A) for *a)* Volmer-Weber growth mode, 3D islands; *b)* Frank-van der Merve growth mode, 2D layer-by-layer; *c)* Stransky-Krastanov growth mode, layer plus islands.

bending in the thin semiconducting film (in particular for the higher-coverage BE shift), as also observed in the valence band evolution (see later discussion), both to a slight conformational modification of the FePc molecules in direct contact with the substrate, consistent with a picture in which the pyrrole rings stay closer to the substrate than the benzene macrocycles at the single-layer.

4.4.1 Growth model

At the beginning of this Chapter we described the three kind of epitaxial growth morphology on surfaces: namely, Volmer-Weber (island), Frank-van der Merwe (layer-by-layer) and Stranski-Krastanov (layer plus island). XPS and Auger Electron Spectroscopy (AES) techniques have long been used to analyse these nucleation modes[172,190,191]. Typical examples plots of XPS or AES adsorbate (A) and substrate (S) intensity versus the amount of adsorbate deposited are shown in Fig. (4.10) for the three common growth modes[192]. In general, V-W growth is characterized by a signal which increases (A) and decreases (S) in a smooth, continuous way. The F-M growth mode typically has a plot with several segments of changing slope, with each break indicating the beginning of a new layer, in both the adsorbate and substrate signals. The plot of S-K growth is ideally characterised by a linear increase up to 1 monolayer followed by a sharp breakpoint, after which the adsorbate intensity increases only slowly, as the islands covering a relatively small part of the substrate are formed. The gradient after the breakpoint is dependent on the island density and shape.

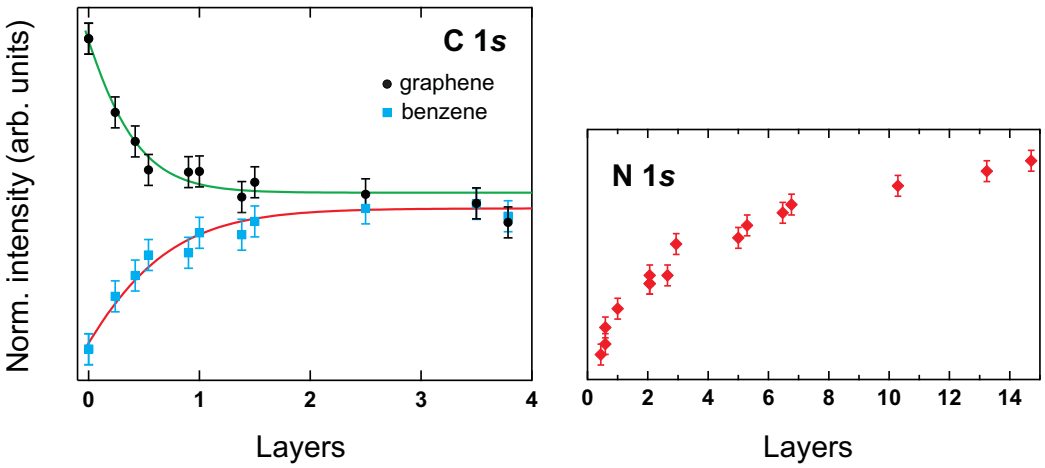

Figure 4.11: *Left)* XPS intensity behaviour of the C 1s components associated to graphene (black) and FePc (blue) with fit-analysis (Stranski-Krastanov growth mode). *Right)* Intensity behaviour of N 1s core-level in a wider range of layers**rifare differenziando co e fe**.

In our case, we established the FePc growth morphology on graphene/Ir(111) by analyzing the C 1*s* and N 1*s* core-level intensity as a function of FePc thickness. The resulting intensity evolution for C-graphene and C-molecule is depicted in Fig. (4.11). The intensity change of the N 1*s* core-level, showed in a wider range, gives an analogous trend (Fig. (4.11)): the evolution is characterized by a linear behaviour till completion of the first SL, followed by a slope change, with subsequent increase of the FePc signals and decrease of the graphene one. By a fit-analysis performed by G. Forte in his Master's Thesis[193] following the model proposed by Ossicini *et al.*[194,195], we identify this behaviour as a layer growth till completion of the single-layer, followed by island uptake, in a Stranski-Krastanov growth mode, with an island coverage of about 16 $\%$ resting on top to the first single-layer^I.

This result is a first clear difference with respect to the FePc growth on HOPG, found to have a three-dimensional island behaviour[196], as we will discuss in the next Chapter.

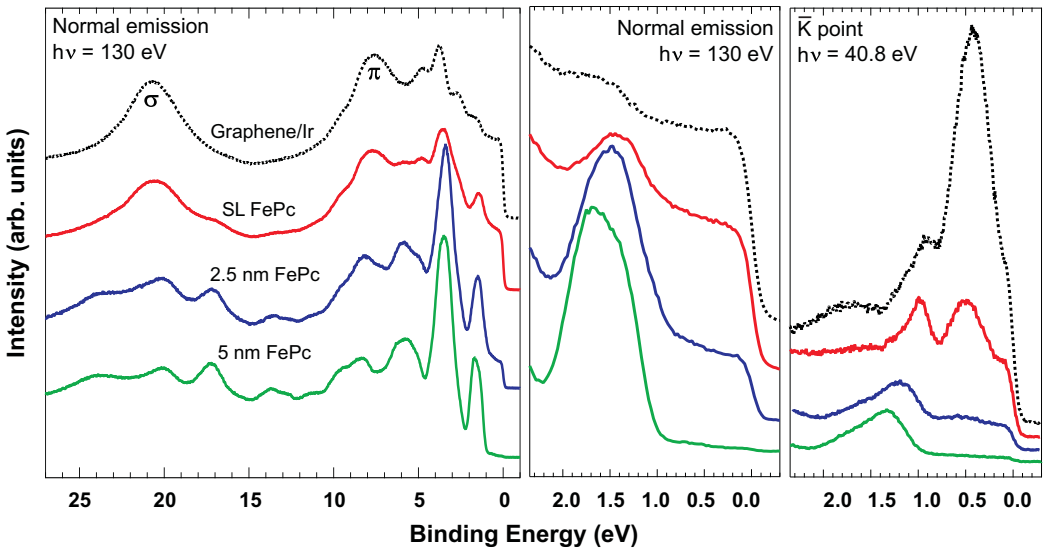

Figure 4.12: Valence-band photoelectron spectroscopy data for FePc/graphene/Ir(111), as a function of FePc coverage (increasing coverage from top to bottom spectra). Left panel: $\pm 8^\circ$ angle-integrated data taken at normal emission, with hν=130 eV photon energy. Central panel: image zoomed on the low binding-energy spectral features. Right panel: $\pm 0.9^\circ$ angle-integrated data taken at the K point of the surface Brillouin zone, with hν=40.8 eV photon energy (data taken with a slight azimuthal rotation, $\approx 1.5^\circ$, with respect to the exact high-symmetry orientation, to better single out the Dirac cone trace). All the spectra are vertically stacked for clarity.

4.5 FePc adsorption on graphene/Ir(111): an ideal doping

All the experimental results discussed so far suggest an almost unperturbed electronic structure of the 2D supramolecular array of FePc molecules assembled on graphene. The study of the evolution of the graphene band parameters upon FePc adsorption can be clarified by ultraviolet and soft x-ray photoelectron spectroscopy. Angle-integrated photoelectron spectroscopy data on the valence band energy region at different photon energies as a function of FePc coverage, are reported in Fig. (4.12).

We report both angle-integrated ($\pm 8^\circ$) data around normal emission (left and central panels) and around the K point ($\pm 0.9^\circ$ of integration) of the surface Brillouin zone, centered on the Dirac cone vertex at 1.70 Å^{-1} (right panel). The clean graphene/Ir valence band at normal emission (left panel) at high photon energy (130 eV), as already discussed in the previous Chapter, is characterized

by the main π and σ bands at about 8 and 22 eV, respectively, and by spectral features due to the underlying Ir(111) surface, in particular the peaks at low BE. In the spectrum of clean graphene/Ir taken at low photon energy (40.8 eV) around the K point of the SBZ (Fig. (4.12), right panel), the main peak centred at about 0.4 eV is due to the angle-integrated Dirac cone, while the shoulder at 0.95 eV is due to the underlying Ir(111) surface state S_2, see Fig. (3.7). Adsorption of the first FePc single-layer induces a general intensity reduction of the graphene-associated states, the centroid of the angle-integrated Dirac cone shifts by 80$\pm$30 meV to higher BE, and a new electronic state appears above 1 eV BE superimposed to the Ir-related bands ^{II} (Fig. (4.12), right panel). At higher molecular density the weak integrated trace of the Dirac cone (Fig. (4.12, right panel)) maintains the -80 meV BE-shift. The FePc 5 nm-thick film eventually presents the typical molecular orbitals in the whole valence band energy region (Fig. (4.12), left panel), with the HOMO at 1.3 eV BE (a_{1u} state of π-symmetry) and the HOMO-1 at 1.6 eV BE (b_{2g} state of d-character), respectively[86,197] indicating the formation of an unperturbed molecular thin-film.

Further details on the graphene band parameters after the FePc single layer adsorption can be achieved by high-resolution angular-resolved ultraviolet photoelectron spectroscopy (HR-ARUPS) valence band data around the K point of the surface Brillouin zone. Photoemission spectra scanned along the ΓKM high symmetry direction are displayed in Fig. (4.13) for clean graphene/Ir (left panels) and for the FePc-SL adsorbed on graphene (right panels). The azimuthal angle has been rotated by $\approx$1.5° with respect to the exact high-symmetry orientation, so that the Dirac cone vertex is slightly lowered in energy and appears just below the Fermi level, allowing to better follow the FePc influence on the electronic states. The energy distribution curves as a function of the polar angle are shown in the upper part of the figure, while the spectral traces of the Dirac cone (energy *vs.* momentum) are reported in the bottom part.

The adsorption of the FePc-SL on graphene causes a slight lowering of the Dirac cone by 80$\pm$30 meV towards higher BE, preserving its high mobility. Thus, since graphene/Ir(111) presents the Dirac vertex at about 100 meV above E_F, its interaction with planar array of FePc molecules makes the underlying graphene sheet closer to ideal graphene. This shift suggests a very tiny charge transfer from FePc to graphene. By assuming that the doping density is proportional to

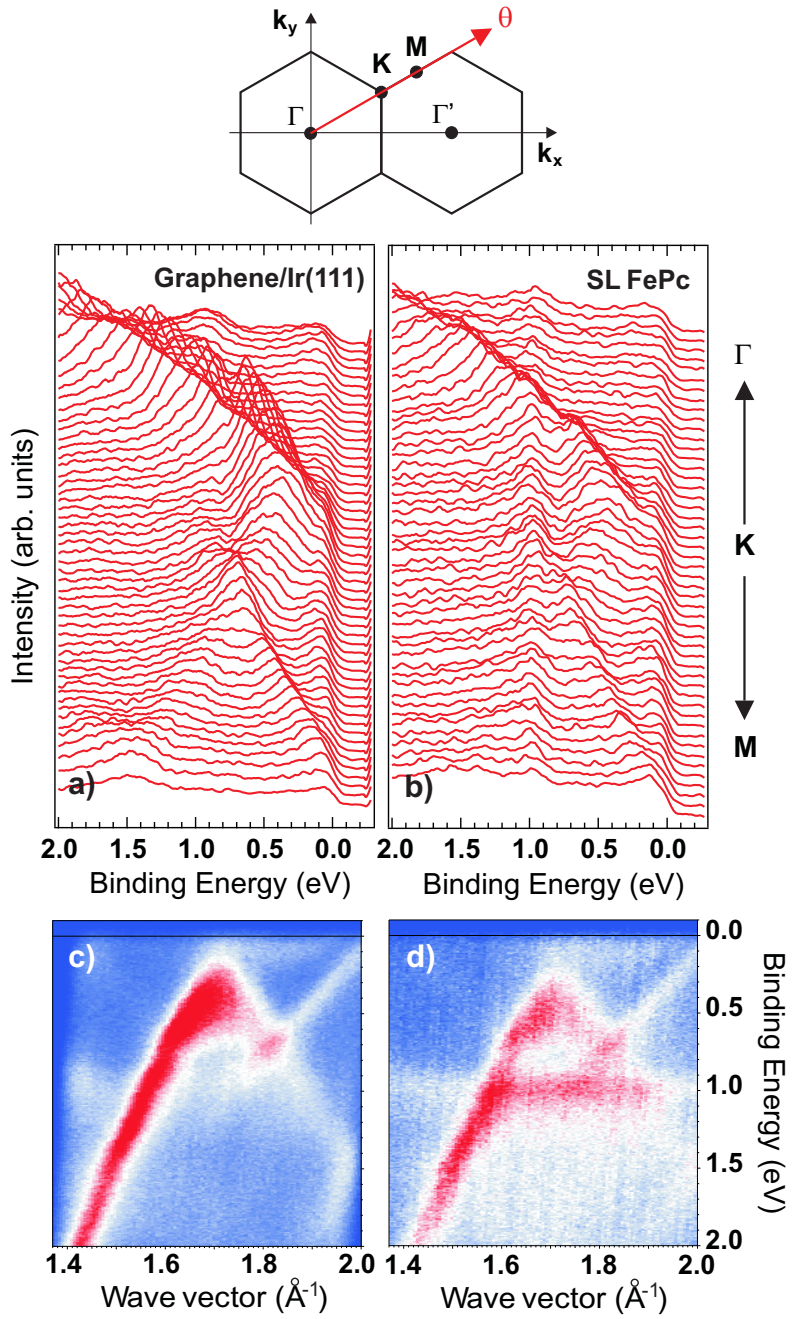

Figure 4.13: HR-ARUPS data taken across the K point of the SBZ along the ΓKM direction, at 40.8 eV photon energy. Sketch of the graphene Brillouin Zone (top image). Energy distribution curves for clean graphene/Ir(111) (a) and for 1 SL FePc adsorbed on graphene/Ir (b); corresponding HR-ARUPS Dirac cone intensity plots for clean graphene (c) and 1 SL FePc/graphene (d). Data taken with ≈1.5° rotated azimuthal angle with respect to the exact high-symmetry orientation, so that the Dirac cone vertex is slightly lowered in energy and appears just below the Fermi level, allowing to better follow the FePc influence on the electronic states.

the amount of dopant molecules[198,199], we estimate about 4×10^{-3} electrons *per* molecule [II].

Doping of graphene by organic molecular charge transfer has been achieved of n-type and p-type for vanadyl-phthalocyanine (VOPc) and tetrafluoro-tetracyano-quinodimethane (F4-TCNQ), respectively, on bilayer graphene grown on silicon dioxide[200,201] and on silicon carbide[202] demonstrating a non destructive way to control the charge carrier in graphene.

4.5.1 Band-bending

In the photoemission data of the FePc/graphene/Ir(111) interface, we have noticed that the BE of the FePc molecular orbitals, measured with respect to the Fermi level, undergoes a common shift by 0.17 eV towards higher BEs, when the nominal film thickness increases from 2.5 nm to 5 nm. This shift in the ultra-thin molecular layer is due to a band bending effect in the subsurface region of the molecular semiconducting thin-film, and this value can be taken into account for explaining the high-coverage C and N 1*s* core-level energy shift. On the other hand, by looking at the HOMO and HOMO-1 BE positions at lower molecular density, still there is an energy shift by less than 0.1 eV between the FePc-SL and the 2.5 nm-thick TF. We do not have evidence of any specific interface HOMO nor of any interface state, at variance with the case of FePc/Au(110), where an actual orbital hybridization takes place[86]. However, the BE at the FePc SL stage may be influenced by a slight macrocycle deformation upon interaction with the moiré pattern of graphene, which also determines the analogous shift in the core-levels of the atoms present in the pyrrole macrocycles (i.e. pyrrole carbon and nitrogen) which is greater than that of the benzene carbon at low coverages.

A resuming energy level diagram is reported in Fig. (4.14). The SL-FePc on graphene/Ir produces an increase of work function by about 0.27 eV, and such a slightly positive variation has been recently observed for other weakly interacting molecules on graphene[95,203]. In the present case, the FePc SL, on one side by inducing a slight n-type doping of the graphene sheet without considerably affecting its mobility, produces a quasi-ideal and supported graphene sheet, on the other side this SL behaves as an ultra-thin slab useful as a planar conduction

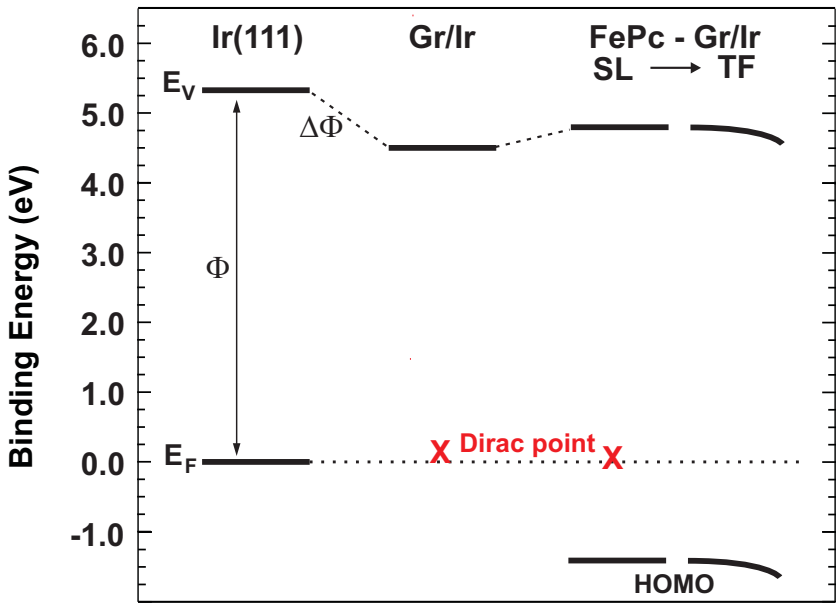

Figure 4.14: Schematic energy level diagram of the FePc/graphene/Ir(111) interface system, as determined through the photoemission measurements.

channel constituting a potential basis for enhancing the adhesion of gate dielectric layers on epitaxial graphene, and for further doping by using substituted MPc molecules. In fact, metal-phthalocyanines constitute a very wide class of square-shaped planar aromatic molecules (more than 70 different molecules have been synthesized so far)[204], and subsequent doping of graphene may be induced through the ultra-thin dielectric MPc layer.

4.6 Conclusions

In this Chapter we characterized the MPc adsorption on the graphene sheet prepared on Ir(111) by absorption spectroscopy, core-level and valence band photoemission. The three different MPcs investigated, FePc, CoPc and CuPc, at first sight behave similarly, as one should expect: they all lie flat onto the graphene sheet (with $(8 \pm 10)^\circ$ angular orientation with respect to the graphene surface, in the case of FePc) up to a multilayer coverage and the growth morphology is consistent with a Stranski-Krastanov growth mode. After the completion of the first layer, a further exposure to MPc molecules gives rise to an island growth; thus at the single layer the influence of the substrate counterbalances the molecule-

molecule interaction. The FePc molecules at the SL arrange in a planar molecular structure, without destroying the moiré periodicity, thus indicating a template-driven supramolecular growth in the first coverage phase. This hypothesis is also supported by the fact that at the SL the ratio between carbon atoms of FePc and that of graphene, as deduced by the C 1*s* core-level's fits, confirms the presence of 3 molecules *per* moiré unit cell, that is less than an uniform coverage ($\approx$ 4 molecules), thus there are regions of the graphene layer which remain uncovered, according to STM observations.

All spectral evidences bring to light a weak MPc/graphene interaction, with a minor molecular macrocycle deformation on the moiré template. However a light electron doping of graphene is induced by FePc adsorption, as revealed by the shift of the C 1*s* graphene core-level and the lowering of the Dirac cone towards higher binding energies, bringing the graphene sheet to a supported quasi-ideal condition.

Small differences emerge among FePc and CoPc by one side and CuPc by the other, as brought to light by the C 1*s* core-level spectra: the different energy shift between the benzene and the pyrrole carbon atoms at the SL and multilayer coverage phase, higher for FePc and CoPc with respect to CuPc suggests a role played by the central metal atom, since it is the only element which differs the three MPcs, while the weak $\pi - \pi$ interaction between the molecular macrocycles and graphene may play a role in establishing the flat-lying orientation.

The array of planar MPc molecules is driven by the underlying moiré superstructure, and constitutes a nanostructure of metal atoms hooked to the graphene surface thanks to the organic macrocycles, decoupled from the metallic substrate, as we will see in the next Chapter where we will investigate the role of the central metal atom in establishing the adsorption mechanism on the graphene moiré substrate.

Chapter 5

A subtle balance between interactions

In this Chapter the role of the central metal atom of MPcs molecules will be definitely brought to light. X-ray absorption spectroscopy across the iron $L_2, 3$ edges allows to understand how the molecular 3*d* orbitals in the D_{4h} symmetry crystal field are modified upon adsorption. A direct consequence of the difference between the 3*d* metal atom in FePc, CoPc and CuPc molecules has been single out by means of temperature-programmed experiments, investigating their adsorption energy on graphene. In this subtle balance between molecule-molecule and molecule-substrate interaction, the role of the substrate will be finally clarified, by comparison with bare iridium and graphite, along with a comparison with literature.

5.1 The role of the 3d central metal atom

In the macrocycle D_{4h} crystal field environment the TM orbital is splitted, as depicted in Fig. (5.1, left panel), into levels with defined symmetries: a b_{2g} singlet (with mainly a $d_{x^2+y^2}$ character), an e_g doublet (d_{xz+zy}), an a_{1g} singlet (d_{z^2}) and a b_{1g} singlet (d_{xy}). The sequence of occupation of these orbitals is far to be trivial and gives rise to the magnetic properties and to the degree of possible hybridization of each MPc.

In particular metal-phthalocyanines with a mostly unfilled 3*d* shell, among

them the $3d^6$ FePc and the $3d^7$ CoPc present a high number of close-lying electronic states, as reported by DFT calculation[197], and moving towards more filled $3d$ shell MPcs, as the $3d^9$ CuPc, the $3d$ metallic character of the molecular orbital is progressively reduced, since electrons become more localized, as reported by many theoretical studies[85,205–208]. Thus, open shell MPcs at the SL-stage are more inclined to interact with supporting substrate, as recently brought to light by observing new interface states and a modification of the empty states associated to the central metal atom in absorption measurements[86,174].

The importance of the central metal atom for MPcs adsorption has been brought to light not only on metal substrates, but recently even on graphene. Dou *et al.*[97] report an electron energy loss study on MPcs adsorbed on graphene/Ni(111) and find a molecule-substrate interaction coupling very different among MPcs with almost filled *d* bands (NiPc, CuPc and ZnPc) and unfilled (FePc and CoPc). In particular, they classify the interaction of the first class as a weak π-π interaction, whereas it is much stronger for the second class and cannot be described by physical adsorption, since they observe a coupling between adsorbate vibrational modes and electronic states. Moreover they observe a decoupling of NiPc, CuPc and ZnPc from Ni(111) when a graphene layer is placed between them, while only benzene rings can be completely decoupled in the case of FePc and CoPc. This different coupling is due to the central metal atom and, by a direct comparison with HOPG, they address this interaction to the Ni(111) substrate. In line with this results Yang *et al.*[96], studied by STM the adsorption of FePc, MnPc, NiPc and H_2Pc on graphene/Ru(0001) and found a similar trend of interaction strength, with the FePc which plays the strongest role among other MPcs. We remind that differences arise between epitaxial graphene grown on different TM substrates and so the results presented so far have to be regarded also taking into consideration the different substrate. We will do this analysis in the next paragraphs, since here we concentrate our attention only to the role of the central metal atom.

The ground state configuration of MPcs has been subject of many theoretical and experimental results, the choice of studying FePc, CoPc and CuPc, resides in the general agreement that these three molecules form a prototypical class of spin 1 (FePc) and spin 1/2 (CoPc and CuPc), carried by different symmetries orbitals: out-of-plane for the first two and totally in-plane for CuPc.

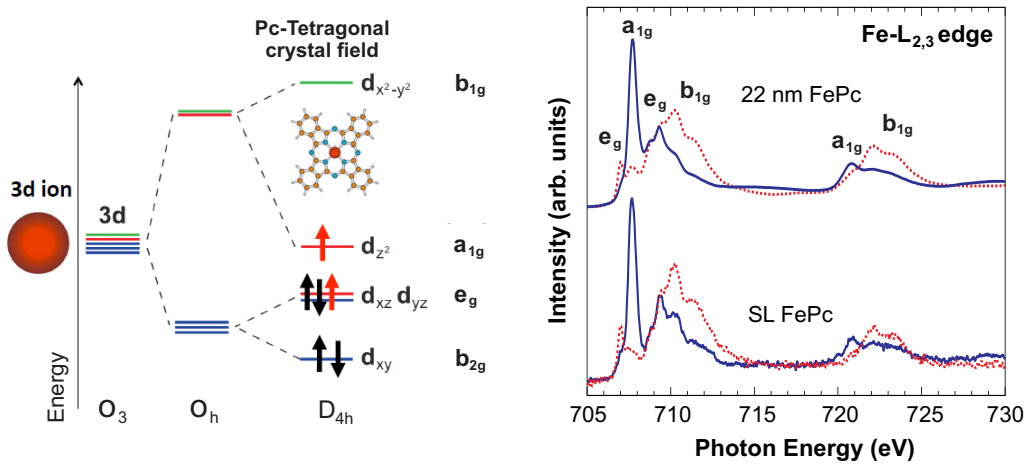

Figure 5.1: Left) Fe 3*d* orbitals in the O_3 symmetry atomic environment, the O_h cubic and D_{4h} square planar crystal field of the FePc molecule. The occupation reflects that of a ^3E_g ground state. Right) Fe-$L_{2,3}$ edges NEXAFS data for SL FePc and 22nm-thick film FePc/graphene/Ir(111). Data taken with linearly polarized radiation, with the electric field vector either parallel (dotted red lines) or almost normal (continuous blue lines) to the crystal surface. The 3*d* orbitals have been labelled according to theoretical and experimental considerations.

We will report experimental results of X-ray absorption of FePc/graphene/Ir(111) system for different molecular coverages. This experiment has been performed at the ID08 beam line of ESRF with the sample at a temperature of 8K using a liquid He cryostat. X-ray magnetic circular dichroism (XMCD) experiment has also been performed and first preliminary results are reported in Appendix.

5.1.1 Fe-$L_{2,3}$ absorption edge

The Fe-$L_{2,3}$ edges correspond to the dipole-permitted transitions exploiting the 2*p* core-electrons to probe the properties of 3*d* empty states. In particular the transitions allowed by the dipole selection rules are:

- L_2: $2p_{1/2} \rightarrow 3d_{3/2}$, 4*s*
- L_3: $2p_{3/2} \rightarrow 3d_{3/2,5/2}$, 4*s*.

The transition towards 4*s* state is however smooth and strongly suppressed with respect to the structured transition toward *d* states.

The Fe-$L_{2,3}$ edges for the FePc/graphene/Ir system as a function of FePc coverage, taken with linearly polarized radiation, are shown in Fig. (5.1 b).

The NEXAFS data for the 22 nm-thick FePc thin-film show a dichroic response associated to the flat-lying configuration, and present a structured absorption near-edge region due to the ligand field splitting of the Fe-related d-levels, in agreement with previous linearly polarized data on flat molecular FePc-TF prepared on different substrates[174,209].

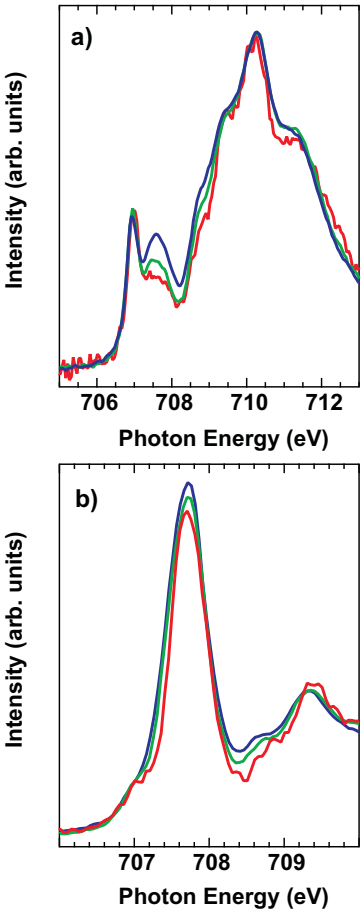

Figure 5.2: Zoom on the L_3 edge with in-plane (a) and out-of-plane (b) for three step of FePc coverage: SL (red), 2 layers (green), 4 layers (blue). Intensities normalized at the step.

Despite the controversial attribution to the actual sequence of resonance states, depending on the use of different exchange-correlation functionals[206,210], the most accepted configuration is the ^3E_g with a succession occupation of the 3*d* orbital as $(d_{xy})^2(d_{xz+zy})^3(d_{z^2})^1(d_{x^2-y^2})^0$, as shown in Fig. (5.1 a). Thus the main absorption features derive from the empty b_{1g} state with $d_{x^2-y^2}$ symmetry, hybridized with the π orbital localized on the N atoms, the partially empty a_{1g} state with d_{z^2} symmetry, and the doublet e_g with d_{zy},d_{xz} symmetry, mainly localized on the central Fe atom.

A direct relationship between a peak and a single molecular state is a bit an over-simplified view, due to the final state multiplet effects, as discussed in Sec. (2.2.2). However, taking into account the sequence of spin-split molecular orbitals[209] and the expected final low spin state ($S = 1$), we can relate the different main absorption features considering the symmetry assessed by electrons excited from the $2p_{3/2}$ or $2p_{1/2}$ initial states, exploiting the high sensitivity of XAS cross section to the relative orientation of polarization vector and final state orbitals: in the out-of-plane configuration, the excited electrons accede to states localized normal to the molecular plane, the main L_3 peak at 707.7 eV photon energy is due to the a_{1g} single empty state,

as evident by its strong polarization-dependence, the higher lying structures at 708.8 and 709.3 eV may be attributed to the e_g states. In the in-plane polarized spectrum, the a_{1g} peak is highly reduced, being its charge-density localized in the direction perpendicular to the molecular plane; the small pre-edge peak at 707.0 eV can be attributed to the e_g state[209], attribution also confirmed by electron energy-loss results[211]; the peaks at 710.3 and 711.5 eV are due to b_{1g}, with exchange splitting of 1.2 eV (confirmed by the analogous features present above the L_2 edge)[174].

The Fe-$L_{2,3}$ NEXAFS data for the FePc-SL on graphene, while maintaining the same dichroic in-plane/out-of-plane response (sign of the flat-lying orientation), present a slightly different lineshape in the near-edge region. In particular, narrower absorption peaks are present in the FePc-SL for both in-plane and out-of-plane spectra in the L_3 energy region (about 10%), with weaker modification across the L_2 edge. Moreover, for the in-plane data at the FePc-SL, a quenched structure is observed in correspondence to the a_{1g} structure (see Fig. 5.2 a), with respect to higher coverage data, more difficult to individuate for the out-of-plane polarization (Fig. 5.2 b) due also to the difficult of background subtraction. At the SL stage, the signal is very small (there is only one iron atom per molecule) over a smooth background and only thanks to the high performances of ID08 beamline it was possible to detect it. Furthermore, this narrowing of the absorption structures at the FePc-SL observed here, was not observed at the nitrogen K-edge, where the SL and the TF spectra can be exactly superimposed, see Sec. (4.2).

A strong intensity reduction and redistribution of absorption spectral density has been observed for the FePc-SL adsorbed on the Au(110) surface[174] where a charge transfer from the underlying metal states to the Fe-related molecular orbitals takes place, with hybridization between the Fe-related d_{z^2}-like orbitals and gold metal states[188], while this strong modification is much less on the Au(111) substrate[212], indicating again that the substrate plays a fundamental role. Similarly, the SL-TF lineshape differences for FePc-SL on graphene are not as high as in the former case of FePc-SL on Au(110), so that not any proper orbital hybridization can be assumed. Theoretical predictions of Fe adsorption on graphene suggest a strong charge transfer with the electronic structure of the filled and empty states strongly altered, and with a reduction of the mag-

netic moment[213]. The Fe central metal atoms of the FePc molecules adsorbed on graphene preserve the multiplet resonance structures, although the slight intensity, lineshape and width variations require further experimental studies, also considering the spin and orbital configuration of FePc after the adsorption.

CoPc with one more electron than FePc has an even more difficult ground state to establish. The dispute concerns the assignment of an orbital to this electron, however, whether assigned to the e_g [214–216] or shared between the a_{1g} and e_g [197,217,218], it leaves a hole in an orbital with an out-of-plane symmetry component. While CuPc, with his single hole assigned without ambiguity to the b_1g state with planar symmetry ($d_{x^2-y^2}$) has the out of plane component almost quenched and thus a different behaviour with respect to FePc and CoPc.

5.2 Adsorption energy of metal-phthalocyanine on graphene/Ir(111)

One of the parameters that could give the strength of the interaction between molecule and substrate is the adsorption energy that is the energy associated to the bond between two materials, in a complementary way it is the energy provided by the temperature (thermal energy) necessary to separate the molecule from the graphene layer.

5.2.1 Thermal stabilization of the FePc SL

Here we focus our attention on the thermal stabilization of the FePc SL adsorption on graphene/Ir(111). In particular, the formation of a stable SL of FePc after thermal treatment of a FePc TF has been observed by following of the core-level and valence band structure evolution during annealing [IV]

In Fig. (5.3) we present a set of XPS spectra of the N 1*s* and C 1*s* core-levels and valence band, obtained after a thermal annealing of a FePc TF up to 500°C, with a linear temperature ramp whose constant rate is 0.3 K/s. The spectra recorded afterwards at RT (black dots) are of the same magnitude and with the same lineshape of the SL spectra (red curve): the permanence of unperturbed signals up to at least 500°C, is a sign of intact FePc molecules still anchored to

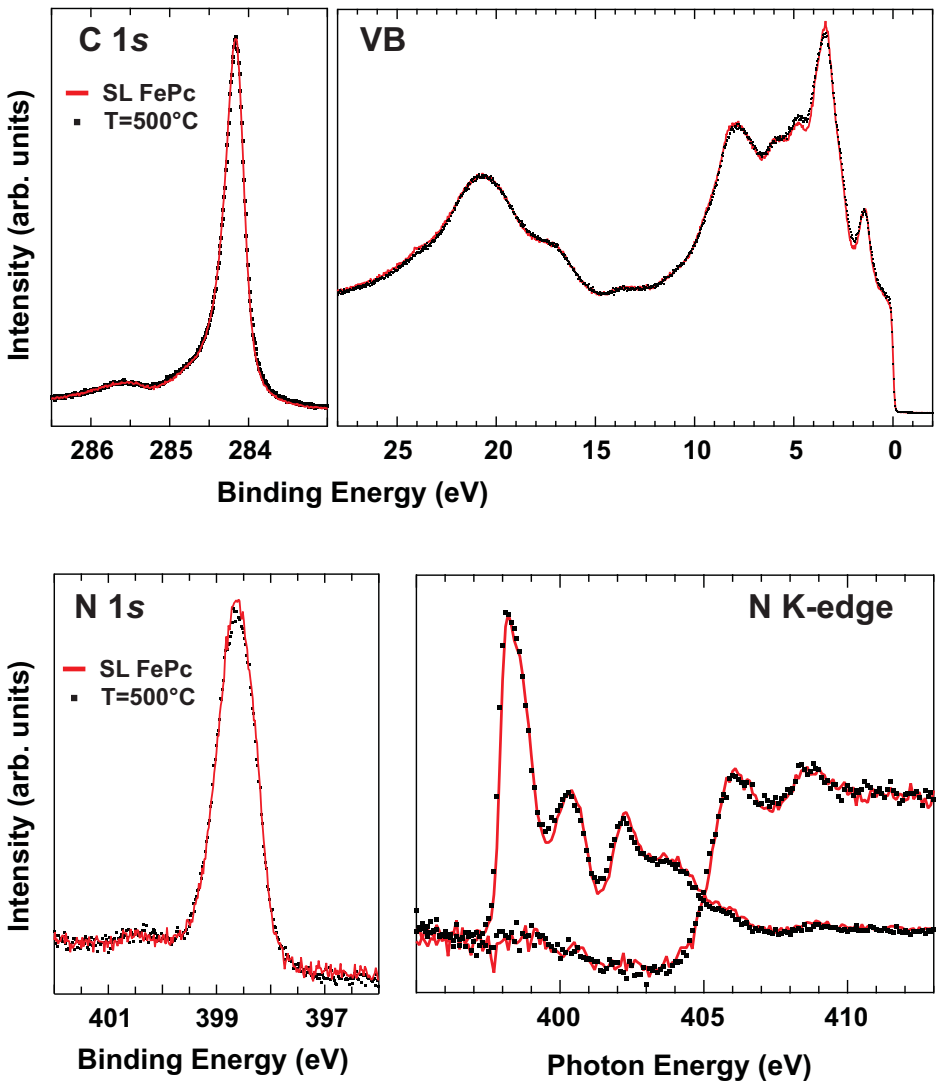

Figure 5.3: Direct comparison between the as-grown FePc SL (continuous red curve) with an annealed TF at 500°C (black dots). The perfect agreement of N 1*s* and C 1*s* core level spectra, valence band and N-K NEXAFS, demonstrates the realization of an high-quality SL after thermal treatment of a TF and its presence up to high temperatures.

the substrate. Absorption spectra across the nitrogen K-edge show that even this annealed layer has a flat-lying configuration, recovering the same lineshape of an as-deposited single-layer. In the N 1*s* spectra, the background was intentionally not subtracted to make the comparison more evident.

This result suggests that the interaction strength of the molecular TF, the molecule-molecule interaction, is not as strong as the molecule-substrate interaction, in fact we recover an high-quality single layer even after an annealing up to 500°C.

5.2.2 Real time temperature-programmed experiments

In order to deeply investigate how the desorption takes place and whether there are differences between SL of similar molecules differing by the central metal atom, we need to follow this process in real time. Thus, we performed temperature-programmed fast X-ray photoelectron spectroscopy (TP-XPS), see Sec. (2.3.1). After the molecular deposition, we linearly increased the temperature of the sample following in situ and in real time the desorption process. By properly choosing a core level signal to detect, we followed the evolution with temperature of the remaining layers of molecules on the substrate . We choose to follow the N 1*s* core-level, because it is a signature of the MPc molecule (M-$C_{32}H_{16}N_8$), since the C 1*s* is difficult to deconvolve from the graphene signal, especially for a single layer of molecules, and the signal coming from the metal atom is too low, both because there is only one metal atom *per* molecule and because the SuperESCA monocromathor does not have access to the deep 1*s* core levels (7-9 keV) and has a very low cross section for the metal 2*p* (700-900 eV) which, besides, is a broaden peak. Thus, the changes in the N 1*s* core-level spectra in intensity, binding energy and width, will give a direct information on the desorption temperature, hence the adsorption energy, of the molecular film deposited on the graphene surface [IV].

With a linear temperature ramp, $T = T_0 + \beta t$ (with β =0.3 K/s in our experiments), we can use of the Redhead Equation (2.34) to estimate the adsorption energy of the molecules. Moreover, since the area of TD peak represents the coverage (Sec. (2.3.2)), by numerically differentiating the total coverage curve versus temperature, we have an approximation of the desorption rate curve, this

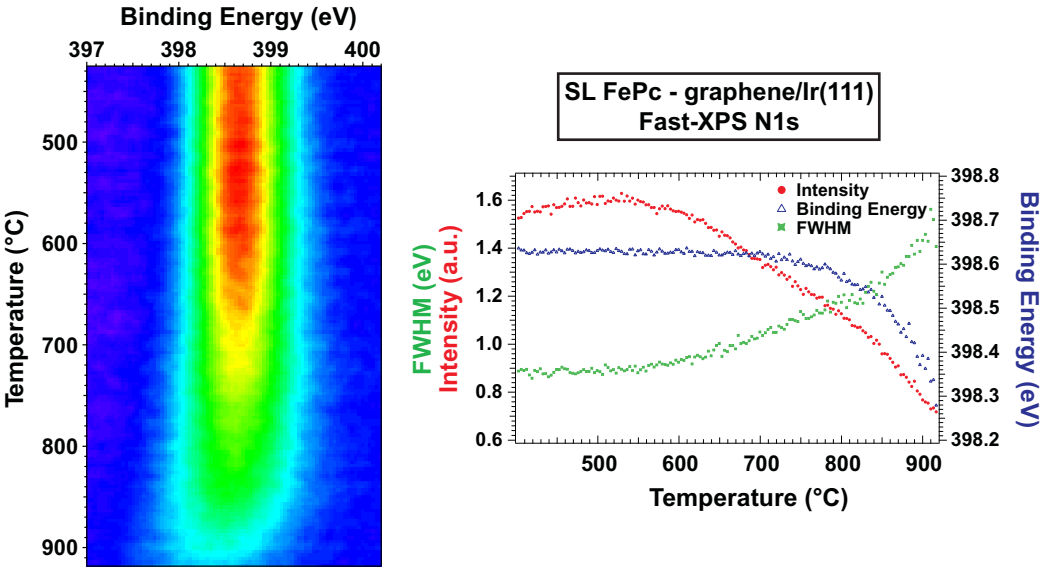

Figure 5.4: *Left)*: Thermal-Programmed (TP) XPS of N 1*s* core-level of a FePc SL adsorbed on graphene/Ir(111). The temperature is linearly increased (rate β=0.3 K/s). *Right)*: resuming fit parameters (one Gaussian peak *per* spectrum), intensity (red) and FWHM (green) are plotted on the left axis, binding energy (blue) on the right axis.

permits to make a direct comparison of this two complementary techniques.

In order to better follow the real-time dynamics, we have to reach a compromise between resolution and acquisition time: with respect to the XPS spectra reported in Section (4.4), in this kind of experiment we increased the used energy step (ΔE from 20 to 38 meV) and the pass energy (PE from 10 to 15 eV) and decreased the acquisition time *per* point (from 0.1 to 0.03 s); in such a way we can recorder a spectrum every 10-11 seconds (which means an acquisition every 3°C). Due to this lower resolution we fit the N 1*s* spectra with only one Gaussian curve, which enables to obtain intensity, width and binding energy, without loosing information with respect to a two components Voigt fit.

FePc

In Fig. (5.4, left panel) we present the TP-XPS spectra performed on the N 1s core-level of the SL FePc/graphene discussed in Sec. (5.2.1). In the right panel there are the resulting fitting parameter: intensity (red) and FWHM (green), plotted on the left axis and binding energy (blue) plotted on the right axis.

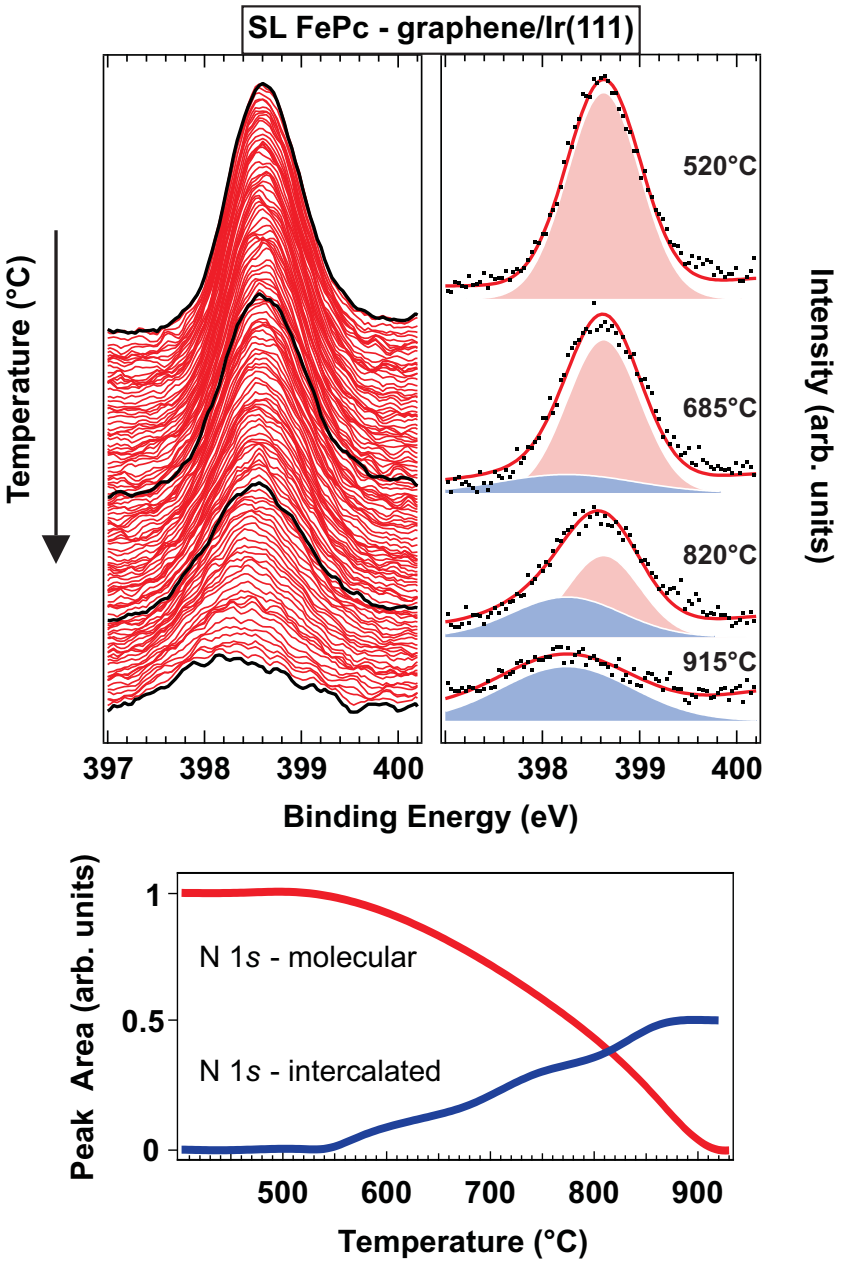

Figure 5.5: *Top*: single spectra of the bidimensional matrix of Fig.(5.4, left), in black a selection of spectra of which the fit analysis is shown (see text for details). *Bottom*: resulting peak area of the two fitted component.

We can easily identify, both in the 2D image and in the fitting parameters, the start of a gentle slope change in the intensity at about 600°C up to very high temperatures (≈ 900°C). This is associated with a progressive broadening of the peak, from 0.9 to 1.5 eV FHWM and then also a shifting of the center position towards lower binding energies (≈ 0.2 eV). The changing in binding energy and width that occurs in the case of SL FePc are unexpected for the N 1*s* core level of the molecule (for MPc, in general), since, even at low coverages (less than a single layer) the only difference is in the intensity, not in shape or position. We interpret these modification as the growing up of a new component at lower binding energy (398.25 eV), wider (1.5 eV) with respect to the molecular component (398.65 eV BE, 0.9 eV FWHM). This component is not properly a modification of the molecular core level, but rather nitrogen coming out from molecular fragments at high temperature.

In Fig. (5.5) we report the single spectra of the fast-XPS and a selection of fits, showing the growing up of the high-T component. By plotting the trend of the peak areas of the two components, we can see that the low energy peak starts to grow up above 550°C togheter with the increase in width of the overall peak, see Fig. (5.4) right panel, and becomes dominant above 800°C. In this way, we can isolate the contribution of the N 1*s* of the phthalocyanine molecule and obtain a more pronounced slope after 550°C, the temperature at which the desorption of the FePc-SL on graphene starts. By using the Redhead equation (2.34) we can estimate the activation energy E_d for the desorption of the SL, with β= 0.3 K/s and T_{max} = (550°C ± 20)°C, obtaining (2.43 ± 0.05) eV.

We used a frequency factor ν in the Redhead equation, equal to 10^{-13} even if, as reported in Section (2.3.2), it could be larger for large molecules. However, we remind that we used always the same heating rate and we the same kind of molecule, thus data are self-consistent even if the absolute value of the activation energy could be affected by a systematic error.

CoPc

In the case of CoPc, we performed a desorption experiment starting at RT from a TF in order to highlight the differences between moelcule-molecule and molecule-substrate interaction strength. In Fig. (5.6 a) we report the fast-XPS

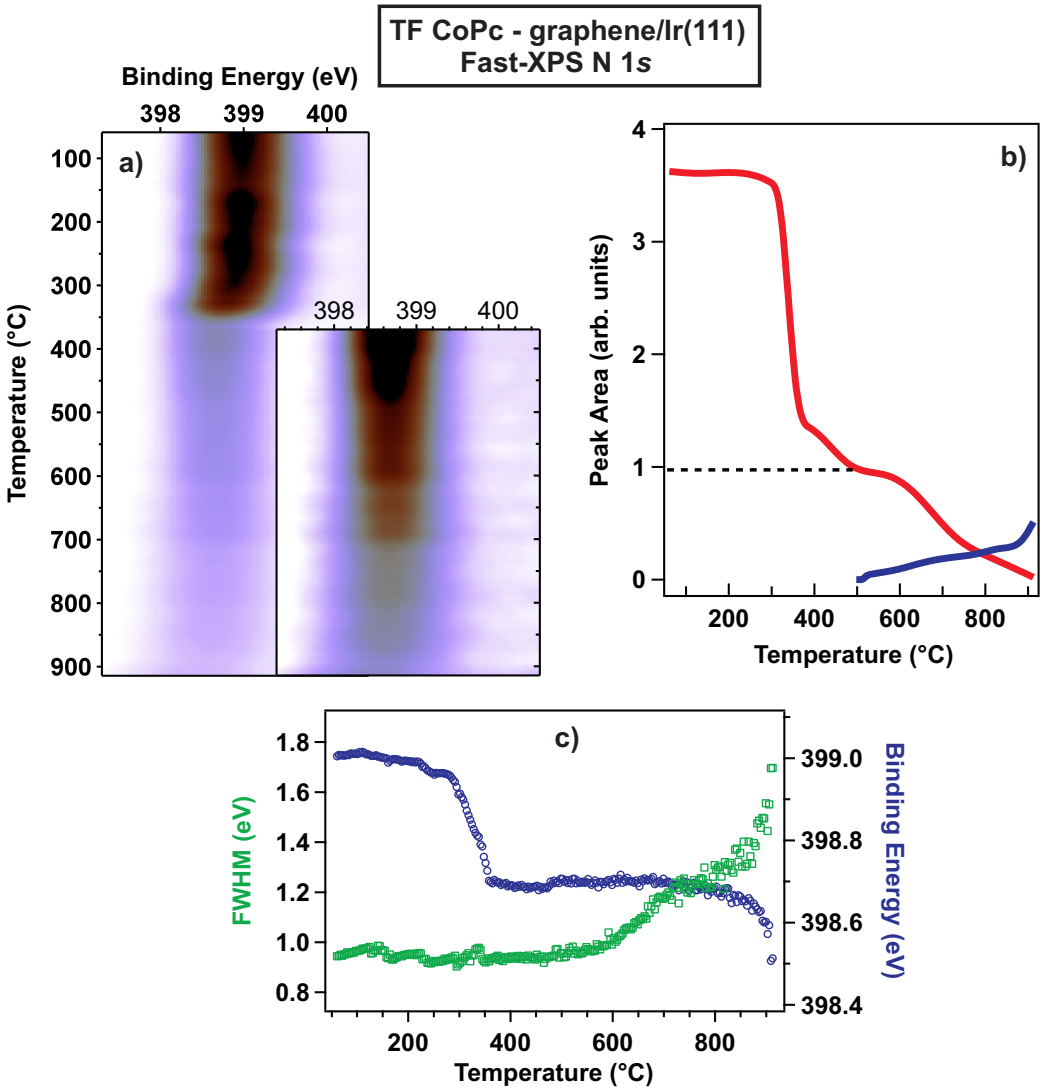

Figure 5.6: Thermal-Programmed XPS of the N 1*s* core level of an initial CoPc TF adsorbed on graphene/Ir(111). *a)* Due to the high intensity of the starting TF, an inset of the less intense region is reported in another scale. *b)* Resulting peak area after the deconvolution of the two nitrogen components. Normalized as coverage curve, 1 indicates the SL. *c)* resulting fitting parameters of initial one-component fit, FWHM (green) plotted on left axis, binding energy (blue) plotted on right axis.

spectra for a CoPc TF (nominally 5 nm, hence $\approx$ 15 layers), sideways a zoom from 380°C with another intensity scale. In order to avoid any possible photon induced damage, as will be shown in the next paragraph, we performed the TP-XPS by periodically varying the position of the sample under the beam, especially for the TF coverages, thus explaining some of the rigid steps in the 2D plot.

We can identify an evident drop of the intensity at $\approx$ 300°C, along with no effects on the width of the peak and a shift to lower binding energy of the N 1*s* centroid position, of about 0.25 eV, Fig. (5.6 c). Once reached 400°C this desorption is completed and the N 1*s* stabilized to the parameter of the SL, even the fall in intensity (Fig. 5.6 b, red line) is consistent with the ratio between TF and SL intensity; in particular, the red curve is normalized to the total coverage: Area=1 corresponds to the SL. These results indicate that this is the desorption of the molecular thin film.

After the desorption of the TF, the behaviour is similar to that observed for FePc: there is a plateau until $\approx$550°C and then a gentle slope change starts up to very high temperatures (900°C), this is associated with a progressive broadening of the peak, from 0.95 to 1.65 eV and then also a shifting of the center position towards lower binding energies. Even in this case, the fit analysis leads to the same conclusion drawn for FePc: a new nitrogen-component which starts to grow up after 500°C, see blue line in Fig. (5.6 b).

CuPc

In Fig. (5.7 a) we report the TP-XPS experiment performed on CuPc. We start with a 2.4nm-thick film of CuPc adsorbed on graphene/Ir(111). We remind that all the films prepared are flat-lying, as confirmed by x-ray absorption across the nitrogen K-edge.

As done for FePc and CoPc, even in this case we performed a fit analysis whose resulting parameters are reported in Fig. (5.7 c). Likewise the desorption of CoPc-TF, we find here a first fall in intensity along with a shift of the peak position towards lower BE (398.65 eV) at 300°C. This is the desorption of the CuPc multilayer, in fact, since this is due only to pure molecule-molecule interaction, it does not depend on the substrate.

The main difference between the two previous case is the second fall in in-

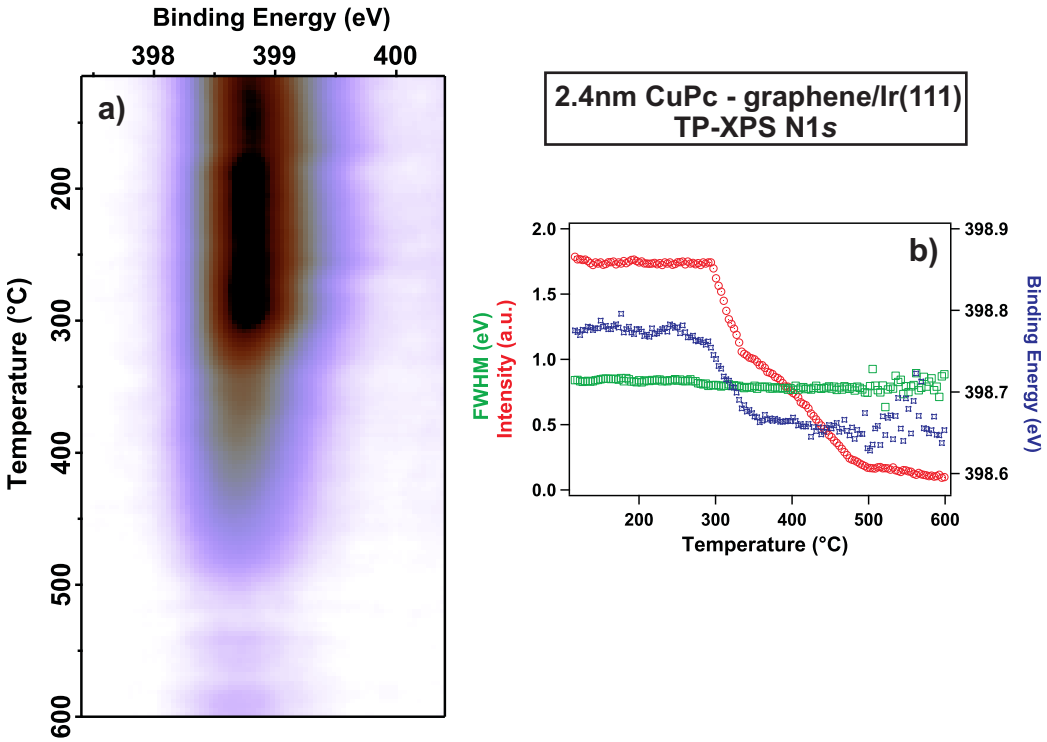

Figure 5.7: *Left)*: Thermal-Programmed (TP) XPS of N 1*s* core-level of a CuPc 2.4 nm-tick film adsorbed on graphene/Ir(111). The temperature is linearly increased (rate β=0.3 K/s). *Right)*: resuming fit parameters (one Gaussian peak *per* spectrum), intensity (red) and FWHM (green) are plotted on the left axis, binding energy (blue) on the right axis.

	FePc	CoPc	CuPc
TF	1.67 eV (300°C)	1.67 eV (300°C)	1.67 eV (300°C)
SL	2.43 eV (550°C)	2.43 eV (550°C)	1.97 eV (400°C)

Table 5.1: Activation energies calculated with the Redhead equation (2.34) for the processes studied. Errors are of ±20°C on the temperature and ±0.05 eV on the energy.

tensity, that corresponds to the desorption of the single layer: for CuPc it starts around 400°C and it is faster than FePc and CoPc, in fact it concludes at about 500°C, as can be seen in the comparison in Fig. (5.8) where the N 1s peak's area of the three phtalocyanines are plotted together. The constant FWHM of the N 1*s* component for CuPc during annealing, Fig. (5.7 c), confirms that the second nitrogen component found for FePc and CoPc is related to the permanence of the molecule up to high temperatures.

By using the Redhead equation (2.34) we can estimate the activation energy E_d for the desorption of the TF and the SL, with β= 0.3 K/s and T_{max} = (300 ± 20)°C and (400°C ± 20)°C respectively, obtaining (1.67 ± 0.05) eV for the TF and (1.97 ± 0.05) eV for the SL [IV]. For a direct comparison the calculated activation energies for the three MPcs studied are resumed in Table (5.1).

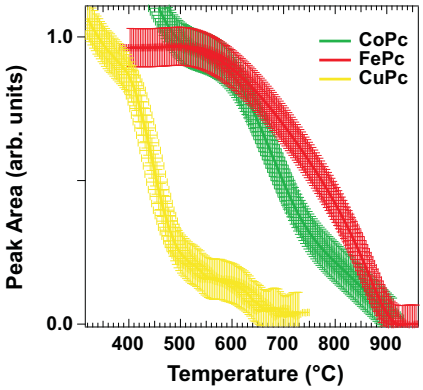

Figure 5.8: Peak areas of the molecular N 1*s* component as a function of temperature of the three investigated MPcs: CuPc (yellow), CoPc (green) and FePc (red). 1 correspond to SL. The desorption temperature is evidently lower for CuPc with respect to FePc and CoPc.

The desorption energy of CuPc is in agreement with similar organic molecules physisorbed on metal surfaces, as pentacene on Au(110) or Cu(110)[219,220] or the CuPc itself on Cu(100)[221]. The desorption energy of FePc and CoPc, instead, is comparable to more interacting interface, in which the structures are dominated by molecule-substrate interactions, due to higher interaction or to particular surface morphology, as pentacene on the vicinal Cu(119) surface[219] where the surface step reconstruction creates preferentially and energetically favourable adsorption site[222] or the organic molecule

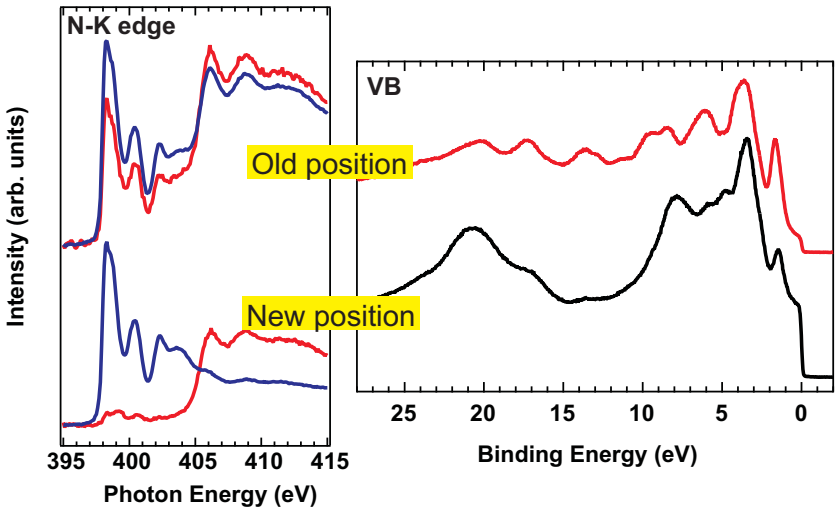

Figure 5.9: The effect of the beam in a molecular thin film. *Left)* NEXAFS spectra across the N K-edge of a 3nm-thick FePc film taken in two different postions: *old position* is where the sample was measured over one day; *new position* was never utilised before. The beam always impinging in the same point has disordered the molecular film, as observed by a non-dichroic signal, otherwise flat-lying. *Right* Valence band spectra taken for an annealed FePc TF up to 500°C: by measuring in the same position of previous measurements the film appear still very thick, as observed by a low Fermi level and prominent molecular structures, while changing position a SL is recovered.

2,4'-BTP adsorbed on graphene/Ru(0001) due to the lateral variations in the molecule-substrate interactions, as we will see later in this Chapter.

5.2.3 Beam-induced processes

Highly intense X-ray photons, as those available at SuperESCA beamline, are a perfect tool to resolve small features and to perform real time XPS, but they can be also a problem when dealing with molecules. Beam damage can break the molecules and, together with high substrate temperature, it can create photon induced effects which are more problematic with thin films of molecules rather than some layers.

Some of the effects that the beam and the high temperature can create are presented in Fig. (5.9). A beam damage effect is the disordering of the molecular film: in Fig. (5.9 left panel) two NEXAFS spectra across the nitrogen K-edge for a 3 nm-thick FePc film adsorbed on graphene/Ir(111) are presented for two different sample positions. We know that a FePc TF lies flat on this system

(Section (4.2)), instead, if the measure is taken in the same position of previous measurements, the absorption signal is non-dichroic, thus sign of a disordered molecular film. This is clearly a beam induced effect since by changing position, and in every other new position, the multilayer turns to be flat-lying.

A second effect, shown in Fig. (5.9 right panel), is a "non-desorbing" TF. In the previous paragraph we demonstrated that upon annealing a FePc TF up to 500°C leaves a high-quality SL, with the same lineshapes of a SL grown directly. The shrewdness is to change the beam position on the sample frequently, otherwise we obtain a film again thick as demonstrated by the valence band spectra which after thermal treatment at 500°C still present prominent molecular structures and a very low Fermi level.

While CuPc desorbs at relatively low temperature, FePc and CoPc are still anchored at $\approx$ 550°C; during their desorption, due to the high temperature, a beam induced nitrogen intercalation seems to take place: the growing of a lower energy peak ($\approx$ 398.3 eV), next to the N 1*s* of the phthalocyanine is observed. This is due to nitrogen atoms in a different chemical environment with respect to the molecular pyrrole ring, that we interpret as an intercalated nitrogen in the graphene film, and referring to the literature[223], we can assigned to a pyridinic form of nitrogen impurity.

5.3 The role of the substrate in the adsorption process

When molecules are organized into well-defined two-dimensional patterns it is not surprising that the nature of the underlying substrate is of essential importance. It can strongly drive the self-assembly process by guiding the organization of molecules into epitaxial layers, even when only weak interactions are present between the adsorbed molecules and the substrate.

5.3.1 FePc adsorbed on Ir(111)

In this and in the previous chapter we demonstrated that MPCs adsorbed on graphene/Ir(111) do not show sign of strong electronic interaction; on the

contrary, graphene acts as a buffer layer decoupling the molecules from the underlying metal. In order to have direct information on the decoupling action exerted by graphene between the Ir(111) surface and the FePc molecules, the FePc molecules have been directly adsorbed on the Ir(111) surface ^{II} with the same rate and substrate temperature (RT) used for the FePc/graphene/Ir interface. The Ir $4f_{7/2}$ and N 1*s* core-levels for the FePc/Ir(111) interface as a function of FePc coverage, are shown in Fig. (5.10). The Ir $4f_{7/2}$ core-level (Fig. (5.10) left panel) at the clean Ir(111) surface presents two main peaks attributed to a bulk and a surface component, at 60.855 eV and at 60.310 eV binding energy (BE), respectively. Adsorption of FePc produces a reduction of the surface component till its quenching when the first single-layer fully covers the surface. In contrast with the case of FePc adsorption on the graphene-covered Ir surface, the molecules have a direct impact on the surface properties of Ir. At higher coverage, the bulk-like component of the Ir $4f_{7/2}$ core-level strongly reduces its intensity. As it concerns the N 1*s* core-level, we present the direct comparison of the spectral feature for the single-layer of FePc adsorbed on Ir and on graphene/Ir (Fig. (5.10) right panel). The N 1*s* structure for FePc/Ir is broader and more structured than the feature on graphene/Ir, and in both systems the satellites at higher BE are still present. The broader N 1*s* peak is indicative of more interaction with Ir, through the pyrrole rings of the molecule.

The NEXAFS absorption spectra at the nitrogen K-edge on the FePc/Ir(111) interface as a function of FePc thickness, are shown in Fig. (5.11). The thin-film spectra (bottom spectra) present the first resonance at about 398.4 eV photon energy, constituted by the two structures associated to the N_1-isoindole and N_2-azomethine nitrogen atoms in the pyrrole ring to the LUMO of π*-symmetry, and the higher-energy structures due to transitions to higher-lying unoccupied states mainly involving the pyrrole ring[173], in agreement with the attribution given for the FePc TF prepared on graphene/Ir(111) shown in this manuscript and on Au(110).[174] However, there is a substantial difference with respect to the TF grown on graphene, concerning the dichroic behaviour. There is an evident reduction of dichroism in the case of the FePc thin film prepared on bare Ir(111), indicating a more disordered molecular uptake. Even at lower coverage, the dichroism is reduced with respect to that measured on the film prepared on graphene and there is a different lineshape of the main absorption features

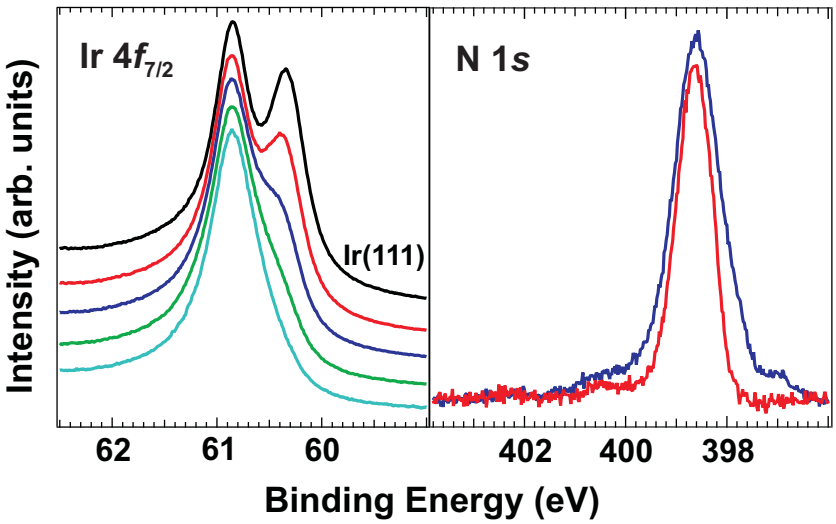

Figure 5.10: Left panel: XPS data of the Ir $4f_{7/2}$core level for the FePc/Ir(111) interface, at increasing FePc coverage (from top to bottom); spectra vertically stacked for clarity. Right panel: XPS data of the N $1s$ core-level at SL FePc on bare Ir(111) (blue line), in comparison with SL-FePc on graphene/Ir(111) (red line).

with a much broader shape for the first resonances involving the empty π levels. Thus, the growth of FePc on Ir(111) determines a different growth morphology with respect to FePc/graphene/Ir: the molecules are not completely flat on the surface. Furthermore, the modified white-line lineshape for the single-layer FePc/Ir with respect to the FePc TF indicates a rearrangement of the empty π-state resonances assessed by the N $1s$ excited electrons upon interaction of FePc with the Ir surface.

In summary, we found that the FePc molecules directly adsorbed on the Ir(111) surface interact with Ir producing quenching of the typical Ir surface states, and the N $1s$ core-level of the molecule presents a broader shape with respect to the case of FePc/graphene/Ir. The FePc single-layer does not form a fully planar layer, and the empty states associated to the π orbitals are modified by this interaction. Moreover, the non fully planar adsorption is further reduced, probably due to vertical rearrangement of the molecules, when a thin-film is formed. Hence, the graphene sheet actually decouples the FePc layer from the underlying metal, allowing the formation of a flat molecular layer potentially available as a thin planar semiconducting channel [II].

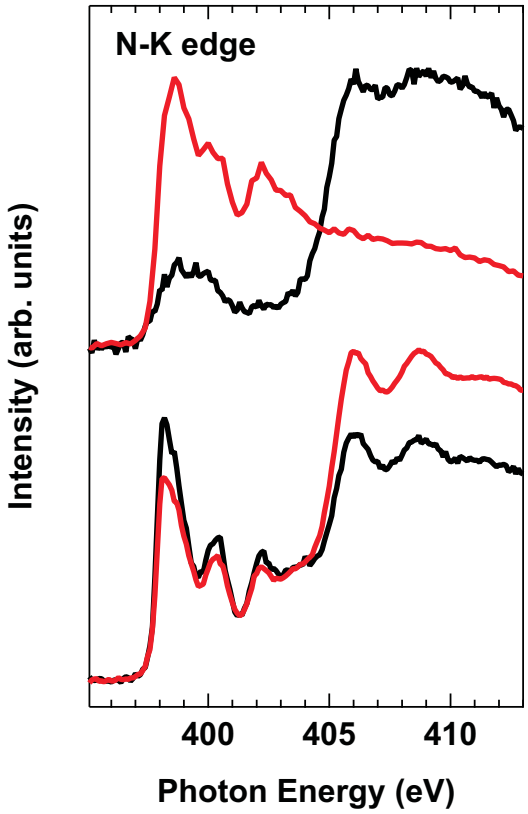

Figure 5.11: N K-edge NEXAFS data for the FePc/Ir(111) interface, as a function of FePc coverage (spectra from top to bottom). Data taken with linearly polarized radiation, with the electric field vector either parallel (black lines) or almost normal (red lines) to the crystal surface. Spectra vertically stacked for clarity.

5.3.2 The role of the moiré superstructure

The results presented in the previous sections that highlight the different behaviour between open 3*d* shell MPcs (FePc and CoPc) with mainly out-of-plane orbitals available for the interaction, and almost filled *d* band MPcs (CuPc), make the point of the role of the central metal atom, defining a scale of interaction strength balanced between molecule-molecule and molecule-substrate interaction.

At the same time we did not observe evident sign of strong interaction between MPcs and the underlying graphene/Ir(111), even better, we report a decoupling role played by the graphene sheet among FePc molecules and iridium, preserving both surface structures of the metal support and the electronic and magnetic properties of the FePc molecules [II,V]

However not only the properties of adsorbates drive the interaction. The other actor is the substrate itself and till now, no words in this sense was said about the particularity of the graphene/Ir(111): the moiré pattern. It does not play only the important role of ordering the molecular adsorption process, as observed in the formation of highly ordered supramolecular kagome lattice of FePc molecules on the moiré pattern of graphene/Ru(0001)[93,96] and, in certain conditions also of CoPc on graphene/Ir(111)[176]. The nanostructured template drives both the adsorption geometry and also the strength without corrupting the properties of the adsorbate [III].

Being graphene a single sheet of graphite, the comparison between them should be done to understand why using a non user-friendly material, as graphene, instead of a most common piece of pencil. To support the importance of the substrate, we report a comparison between FePc adsorbed on highly oriented pyrolitic graphite (HOPG) and on graphene/Ir by means of thermal desorption spectrometry (TDS) and x-ray absorption spectroscopy (XAS), and by the support of literature results.

Adsorption of phthalocyanines, and in particular FePc, on HOPG was widely studied by the group of C. Puglia and coworkers in Sweden[177,196,224] by means of STM and photoemission. They found a high mobility of the molecules under the scanning tip even at low temperatures and a densely packed island nucleation, consistent with a Volmer-Weber growth mode. They performed also density

functional theory (DFT) ground state simulations of a single metal-free phthalocyanine (H_2Pc) molecule and they report a very good agreement between the simulations and the experimental results, indicating that the molecular electronic states are not significantly modified by the adsorption on the surface, they behave as isolated molecules[224]. The same molecular level electronic states resolution is not achieved for the same molecules adsorbed on Au(111), as a consequence of a stronger molecule-substrate interaction[224]. Their conclusion is that only a weak molecule-surface interaction, probably of van der Waals type, takes place. Furthermore they report that, at low coverage, only FePc, and not H_2Pc, tends to organise in chains, but, as they report *"When adsorbed in chains, the molecules are in a metastable position easily disturbed by the scanning tip"*[196]. This difference between these two kinds of molecules highlights the role of the central metal atom in FePc which, even if very weakly, interacts with the substrate. Concerning the growth morphology, with the exception of ZnPC that assume a standing up position with the π-stacking parallel to the substrate[225], Pcs on HOPG form flat-lying densely-packed islands[186,196], without any specific adsorption site, and then evolve in 3D island growth maintaining the planar orientation, a Volmer-Weber mode. This is a clear difference with the growth on graphene, demonstrated to be a Stranski-Krastanov mode [I], and this implies a different interaction at the SL stage, higher on graphene/Ir(111) than on HOPG.

To definitively bring to light this difference, we performed a thermal desorption experiment (TDS), reported in Fig. (5.12). We adsorbed a FePc-TF on HOPG and on graphene/Ir and we annealed the sample with a controlled temperature ramp (heating rate β=0.3 K/s, see Sec. (2.3.2) for experimental details). The desorbing molecular fragments were analysed by means of a quadrupole mass spectrometer, we remind that the molecular cracking *after* the desorption is induced by the spectrometer itself. In Fig. (5.12) is reported only the desorption relative to the 50 amu mass, relative to a benzene component C_4H_2, the smoothed data is in red for FePc/HOPG and blue for FePc/graphene. On both the spectra we can identify three peaks, the first one at about 150-200°C is due to the desorption of disordered molecules from the sample manipulator and the environment, in particular, due to better experimental condition in the case of HOPG, this feature is strongly reduced; the second peak at about 325°C is due to the desorption of the flat molecular thin-film, according with our measurement

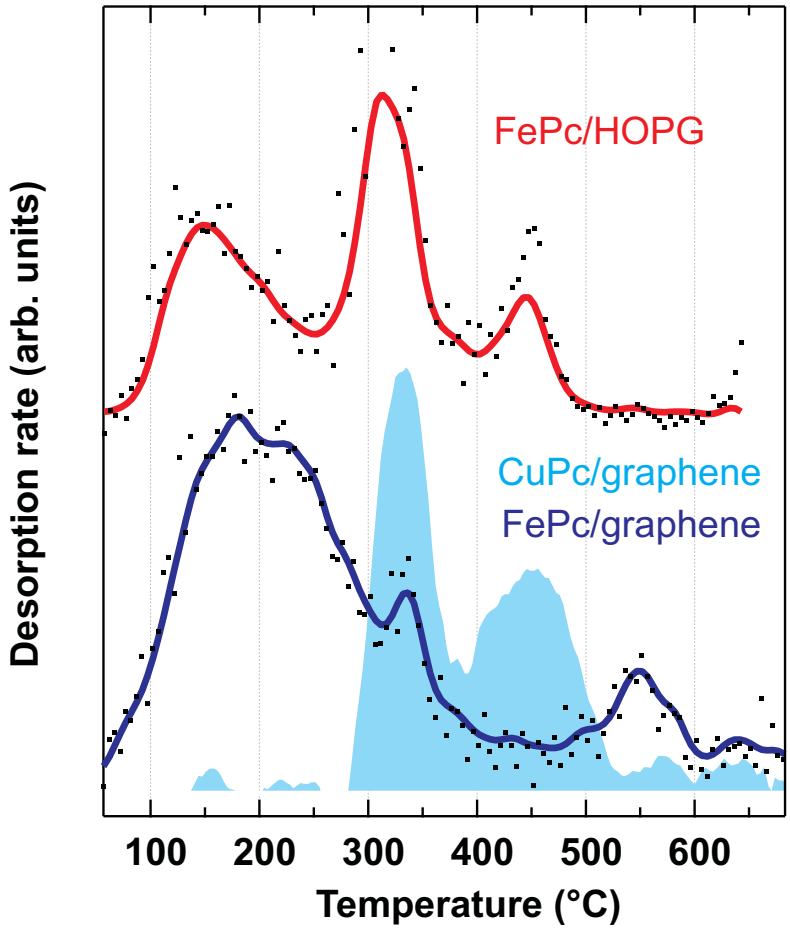

Figure 5.12: Thermal Desorption Spectrometry (TDS) spectra performed on FePc-TF adsorbed on HOPG (red, top) and on graphene/Ir(111) (blue, bottom). Black dots are the data points, continuous curves are obtained after a smoothing procedure. To the FePc/graphene spectrum is superimposed the derived desorption spectrum of CuPc/graphene/Ir(111) obtained from TP-XPS coverage curve of Fig.(5.7).

of TP-XPS (see Sec. (5.2.2)), we confirm that the molecular TF interaction strength is only due to molecule-molecule interaction, indeed it does not depend on the substrate. Finally, we have a third peak, located at different temperatures among the two sample, higher on graphene than on HOPG: it is the desorption of the molecules in direct contact with the substrate: the evident difference of about 100°C confirms the hypothesis that FePc on graphene/Ir(111) are more stronger bound to the substrate with respect that on HOPG and this is reflected in the different growth mode [III].

For each experiment we followed the desorption of several masses (not shown here), we observed the relative peaks at the same temperature for every experiment, this is a sign that the molecule is desorbing as a whole and there is not fragmentation.

Furthermore, in Fig. (5.12) is superimposed to the desorption spectrum of FePc/graphene, the desorption spectrum of CuPc/graphene obtained by numerically derivating the TP-XPS coverage curve of Fig. (5.7). This is a confirmation of the complementarity of these two techniques and besides highlight once more the weak adsorption energy of CuPc on graphene comparable to that on HOPG.

A further comparison between FePc adsorbed on HOPG and graphene has been done by x-ray absorption spectra at the $L_{2,3}$ edge, reported in Fig. (5.13). We can see that peaks on HOPG are sharper and more defined than on graphene, paradigmatic for an isolated molecule.

Since the analysis of core-levels and x-ray absorption data does not show sign of evident interaction in both the systems, the difference in the interaction strength is clearly due to the nature of the substrate, in particular to its morphology: HOPG surface is flat, where the adsorbed molecules are dominated by intermolecular interactions and the substrate-molecule interactions are mainly responsible for the preferential orientation of the respective adlayer networks; the moiré pattern of graphene/Ir, instead, is a template, modulated regularly in shape, with a periodicity of 26 Å (we remind that a FePc molecule has planar size of 11 Å). The geometrical corrugation of the moiré is directly related to a chemical inhomogeneity (see Sec. (3.1)) due to the different arrangement of the carbon atoms with respect to the iridium atoms reflecting in the three different regions, namely *hcp*, *fcc* and *atop*. With this peculiarity, the moiré pattern exhibit very different local electronic structures that influence the self-assembling

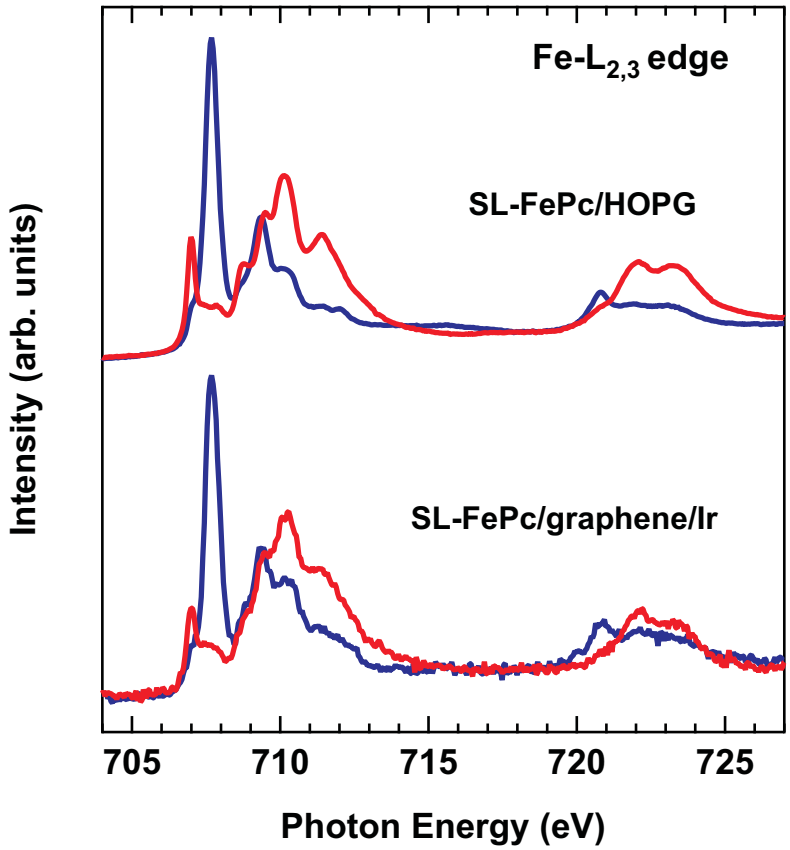

Figure 5.13: X-ray absorption spectra with linearly polarized light across the iron $L_{2,3}$ edges for a FePc SL on HOPG (top spectrum) and graphene/Ir(111) (bottom spectrum). Red line: in plane polarization; Blue line: out-of-plane polarization.

behaviour of adsorbed molecules.

In the very last years, STM studies of MPcs adsorbed on graphene has started to be published, and are mainly STM experiments performed on graphene/Ru(0001) by the group of H.-J. Gao and coworkers in China[92,93,96]. The commensurate match between molecular dimension ($\approx$ 11 Å) and moiré periodicity (30 Å for Ru, 26 Å for Ir) is a first important parameter. They found a selective-site adsorption whose regularity depends on the central metal atom of the molecule. The strongest interaction has been found for FePc which, at initial low coverages, adsorbs only at the *fcc* regions of the moiré until they form an ordered two-dimensional superlattice of isolated molecules[92], while other MPcs occupy both *fcc* and *hcp*, forming molecular chains (MnPc) or a Kagome lattice (NiPc and H_2Pc)[96]. That not only remarks the already reported difference among the family of phthalocyanines, but also confirms the inhomogeneity of the moiré structure due to the interaction with the TM substrate. In particular they found a local work function variation in different regions of the moiré: minima are found for *fcc* and *hcp* regions, both lower than the atop region[92], this explains why the hills of the moiré remain unoccupied. Upon adsorption of FePc the work function increases, the larger the work function change, the higher the desorption energy; the variation indicates a preferred *hcp* site (where the WF change is larger), thus in contrast to experimental observation which indicates the *fcc* region as a preferred adsorption site. We report a smaller, but in the same direction, (non-local) work function variation of 0.27 eV before and after molecular adsorption, see Fig. (4.14). Not only the local work function variation[38,226] can solve this puzzle: *ab initio* calculations[92] reveal that lateral electric dipole field drive the selective adsorption on the *fcc* regions acting as molecular trapping without the formation of strong covalent bonds, therefore the facts that the hills remain unoccupied indicates that the corrugation of the adsorption potential exceeds the additional intermolecular interactions between the supramolecular layer[113].

We already discussed the differences between graphene grown on different transition metal substrates in Sec. (1.1.2), we remind that graphene grown on nickel and ruthenium are among the most interacting graphene sheets, but only the second presents a moiré corrugation, while on Ni(111) the two lattices have the same periodicity and the graphene sheet does not present an ordered moiré superstructure.

In particular, graphene on iridium is less interacting than on ruthenium, and as a consequence the corrugation (both geometrical and chemical) is lower. Since we have no direct proof of the ordering of the molecules on the surface, it is helpful the comparison with the case of graphene grown on platinum, that, in the scale of interaction, is lower than iridium. On platinum the interaction is so lower that the substrate does not succeed in forcing the graphene sheet to go in register with it, the consequence is the formation of various moiré superstructure with different orientation together with unrippled regions[227,228]. FePc adsorbed on graphene/Pt(111) forms islands[96], growing in a Volmer-Weber mode, as on HOPG, hence with dominating molecule-molecule interaction.

Since graphene/Ir(111) is in between Pt and Ru, concerning the strength of interaction with the metallic substrate, and presents very regular and extended moiré corrugation we expect a behaviour in driving the molecular self-assembly more close to that of graphene/Ru(0001). This assumption is supported by the FePc adsorption, characterized by a Stranski-Krastanov growth mode and by the non-destroyed moiré LEED pattern. The present experimental results demand careful theoretical calculations and a STM experimental support for a deeper understanding of the actual adsorption mechanism of MPcs on graphene/Ir(111).

5.4 Conclusions

All the results presented so far, show a different behaviour between SL of FePc and CoPc, on one side, and CuPc on the other, in their interaction with underlying graphene/Ir(111) substrate. In general we found a substantially weak interaction between the molecular SL and the substrate, however this interaction appears to be even lower in the case of CuPc for two reasons:

- the difference in the benzene and pyrrole carbon atom energy shift indicates a minor deformation for the CuPc molecule at the SL layer stage;
- a low desorption energy at the SL, close to that of the TF, in contrast to a rather high desorption energy for the FePc and CoPc SL, sign of a stronger interaction than a pure Van der Waals.

The reason of this difference lies in the different occupation of the $3d$ shell of the central metal atom of the MPcs: moving from molecules with mostly unfilled

3*d* shell, as FePc and CoPc, to molecules with more filled 3*d* shell, as CuPc, the metallic character of the molecular orbital is progressively reduced. Thus open shell MPcs at the SL-stage are more inclined to interact with supporting substrate.

The role of the substrate is finally remarked: the moiré superstructure plays an important role in the interaction process, trapping the molecules, while maintaining their electronic properties mostly unaffected. The graphene layer indeed act as buffer layer decoupling the anchored molecular layer from the underlying metal substrate.

Appendix A

Magnetic properties

Here we present magnetic moments measurement by means of x-ray magnetic circular dichroism (XMCD) on the flat FePc molecules adsorbed on graphene to determine their spin and orbital configuration exploring both their angular and thickness behaviour [V]*.

A.1 XMCD technique

XMCD technique exploit the differential absorption of right and left polarized light which may take place depending on the magnetization of the sample. Since the sample is paramagnetic, the magnetization can be induced by an external magnetic field $\pm B$. In our notations the x-ray beam and the external magnetic field are collinear and oriented along the z axis. The two different photon helicities, positive (right circular polarization, R) or negative (left circular polarization, L), can be *parallel* or *anti-parallel* to the magnetic field applied, thus generating parallel (I^+) or anti-parallel (I^-) absorption intensities. The XMCD signal is defined as the difference in the absorption coefficients for this two orientation:

$$\Delta I = I^- - I^+, \tag{A.1}$$

*The data analysis conducted in this section is mostly due to the Ph.D. student S. Lisi. For this reason here I present a synthesis of the important results helpful in the context of this Thesis without going into deeper details.

thus, in absence of a net magnetization, this signal will be equal to zero, since for a given initial state, R and L polarized photons will excite photoelectrons having opposite spin polarization, otherwise the $p_{1/2}$ and $p_{3/2}$ shells behave as spin-polarized sources, while vacant spin-up and spin-down 3*d* bands behave as spin-sensitive detectors.

In addition to dipole selection rule, magnetic quantum number and spin quantum number selection rules must be taken into account when the sample has a net magnetic moment. Hence using an external magnetic field to induce the orientation of the spin and orbital moment of the sample, the circular dichroism selection rules allows a determination of the sample magnetic moments. Clearly we are interested in the 3*d* metal atom magnetic configuration, so, in what follows, we refer to the $2p \rightarrow 3d$ absorption spectrum, the $L_{2,3}$ edge.

The per-atom magnetic moments are related to the following magneto-optical sum rules[229,230]:

$$\begin{aligned} \mu_L(\theta) &= -\frac{2n_h}{r}\int(\Delta I_{L_{2,3}})dE\mu_B \\ \mu_S^{eff}(\theta) &= -\frac{2n_h}{r}\int(\Delta I_{L_3} - 2\Delta I_{L_3})dE\mu_B, \end{aligned} \tag{A.2}$$

where n_h is the number of holes in the 3*d* orbital, that it has to be determined via theoretical methods or approximated under reasonably conditions; $\Delta I_{L_{2,3}}$ represent the dE integration over the $L_{2,3}$ absorption edge; r is a normalization factor.

XMCD measurements has been performed at ID08 beamline at ESRF, with a $\pm$5T applied magnetic field and the sample at a temperature of 8 K through a liquid helium cryostat. For each absorption intensity, several scans where collected by changing the applied magnetic field sign and contextually the helicity of the photon since I^+=I(R, +B) or I(L,-B), vice versa for I^-. The strong advantages of this technique are the high sensitivity and the element selectivity.

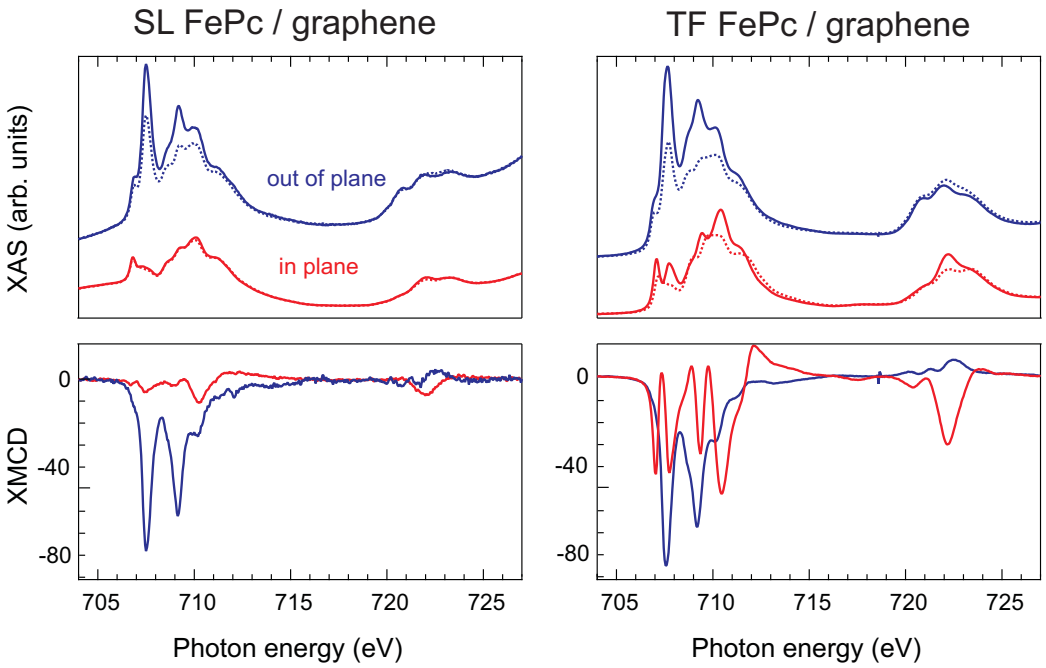

Figure A.1: FePc circular polarized absorption spectra I^+ and I^-, for the single layer (left) and 22nm-thick film (right). In the lower panels, the XMCD is reported

A.2 Magnetic properties of FePc/graphene/Ir(111)

To understand the magnetic properties of FePc molecule it has to been kept in mind the ground state configuration of Fig. (5.1 a). The absorption spectra (with circularly polarized light) and the XMCD signal for SL and TF FePc/graphene/Ir(111) are shown in Fig. A.1. They both presents a magnetic response.

Avoiding the substrate influence, we start in the description of the TF, consistent with previous published data[209]. The higher dichroism for the out-of-plane spectra is due the symmetry of the system: the flat lying molecules and the symmetry of the 3*d* orbitals in the molecular crystal field. Thus the easy magnetization axis direction, given by the direction with the largest component of orbital momentum **L**, is parallel to the substrate. In fact the anisotropy reflects the symmetry of the orbitals involved in the transitions: the out-of-plane absorption spectra are dominated by the transition to the a_{1g} and e_g out-of-plane orbitals, while in the in-plane we can identify the transitions towards the b_{1g} orbital at energy greater than 709 eV; in this last spectrum, the XMCD signal

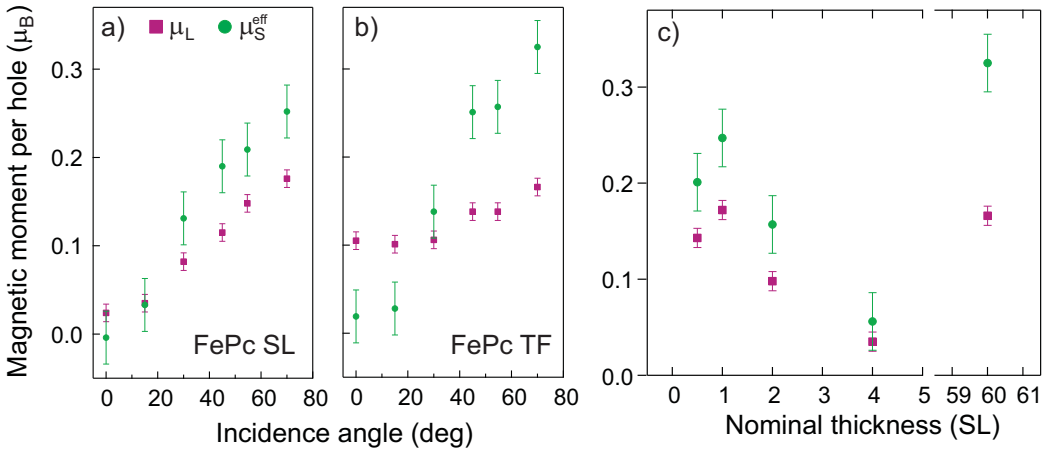

Figure A.2: FePc magnetic moments (orbital moment μ_L and effective spin moment μ_S^{eff}) as calculated using XMCD sum rules A.2. a) and b) behaviour as a function of incidence angle for SL FePc/graphene/Ir(111) and 22nm-thick film, respectively. c) behaviour as a function of surface coverage.

shows two peak with opposite sign corresponding to the b_{1g} double vacancy and hence reflecting the different spin orientation.

Concerning the SL we observe an almost unchanged out-of-plane XMCD signal, while a quenched in-plane signal, hence there is an enhancement of the in-plane/out-of-plane anisotropy for the SL FePc/graphene/Ir(111) with respect to the TF. The almost zero quenching of the XMCD signal can be explained by the weakly interacting a_{1g} and e_g out-of-plane orbitals with the substrate: no charge transfer from the substrate quenches the magnetic response of these states, as instead observed for FePc and CoPc SL deposited on Au(110)[231]. A non-quenching XMCD signal is found for the weakly interacting CuPc SL on Au(110)[231], however in this case the magnetic moment is carried by the planar b_{1g} singlet, which couples weakly to the metal electrons, as stated in the previous paragraph.

A deeper observation of the in-plane component at the SL allows to discern the behaviour of the single peaks: in particular, we can observe a strong quenching of the signal corresponding to the b_{1g} orbitals above 709 eV, while an almost total absence of the signal corresponding to the a_{1g} and e_g orbitals three features before 709 eV. A similar behaviour has been observed even for SL FePc on Au(111)[212] and interpreted through simulations as a very weak orbital configuration mixing at the single layer, best described within a mixed valence

scheme, which substantially does not affect the orbital character of the ground state, therefore the absorption spectra are very similar between SL and TF, but has a great impact on the magnetic moment of the molecule/surface complex, reducing the effective spin from 1 to 1/2 and open the door to Kondo physics.

All these observations can be quantitatively seen by applying the sum rules, Eq. (A.2), to both SL and TF to relate the XMCD signal to the orbital μ_L and effective spin μ_S^{eff} moment (calculated per number of 3*d* holes, n_h), shown in Fig. (A.2 a,b) as function of the x-ray beam (and the collinear applied magnetic field) incidence angle. μ_L and μ_S^{eff} reach the maximum values for both coverages at 70° of incidence, indicating an in-plane easy magnetization axis. Moreover an higher anisotropy of μ_L is observed in the flat SL with respect to the flat TF.

An intriguing behaviour is observed in the trend of magnetic moments in the easy magnetization direction as a function of thickness, as presented in Fig. (A.2 c) FePc μ_L and μ_S^{eff} reach their maximum values at the SL completion, then decrease monotonically at higher coverages: the XMCD signal at 4 SL ($\approx$ 16Å) is strongly reduced compared to the SL, after that re-increase to reach the TF values.

In spite of the similar behaviour of SL CuPc/Au(110) concerning the non quenching XMCD signal, this thickness trend is far to be trivial and different from the FePc/Au(110) monotonous increase.

For SL FePc/graphene/Ir(111) we have thus a "single-molecule" behaviour, miming a non-interacting layer, while for subsequent layers a quenching of about 75% takes place. This is intriguing because it is not supported by changing in the linear absorption $L_{2,3}$ spectra indicating an evident alteration of the lineshapes as observed by Stepanow *et al.* for SL FePc on Au(111)[212].

In conclusion these preliminary data show a quite puzzling problem, a theoretical approach is needed in order to better understand which orbitals are involved and what kind of interaction takes place. Furthermore, an experimental comparison with the behaviour of metal-phthalocyanine with different orbital occupation and spin configuration adsorbed on graphene/Ir(111) would be highly helpful. What is however important to note is the decoupling action of the graphene sheet between molecules and metal substrate, graphene acts as a buffer layer preserving, or even better, enhancing the magnetic properties of a FePc SL self assembled onto it.

Conclusions

In this Thesis, the self-assembling of metal-phthalocyanines on the moiré pattern of graphene/Ir(111) has been studied. Among the several substrates on which graphene can be grown, the hexagonally close-packed (111) surface of iridium has revealed to be the best compromise between interaction and natural corrugation. Graphene on Ir(111) reveals all the electronic properties of free standing graphene almost unaffected by the interaction with the substrate, the weak hybridization is testified by a slight p-doping of the Dirac cone. Ir(111) is therefore a good substrate leading to a quasi-free standing graphene sheet with the remarkable advantage of the formation of a highly-ordered hexagonal modulated moiré superstructure generated by the slight lattice mismatch between the lattice constant of these two materials, testified by both STM and LEED measurements. Furthermore, a high stability and a low degree of degradation of supported graphene after air exposure has been demonstrated by fully recovering of the as-grown properties by annealing treatments.

The moiré structure has been thus exploited as a template to fabricate unique bidimensional molecular networks of metal-phthalocyanines (FePc, CoPc and CuPc). The main effect of the adsorption of a FePc single-layer onto the graphene sheet is a light electron doping, which counterbalances the original p-doping of graphene/Ir, bringing the graphene sheet to a quasi-ideal condition.

By means of X-ray absorption spectroscopy we demonstrated the flat lying geometry of the molecular layers adsorbed on graphene. The organic macrocycle of the molecules presents a weak interaction with the substrate, since no core-level lineshape changes are observed from single-layer stage to thin-film. However, subtle differences between molecules arise: the difference in the benzene and pyrrole carbon atom energy shift indicates a minor deformation of CuPc in direct contact with graphene with respect to FePc and CoPc.

Thermal-programmed experiments have revealed to be a powerful tool to investigate the interaction strength between molecules and substrate. The different behaviour of CuPc with respect to FePc and CoPc is obtained by a low desorption temperature of the molecualr single-layer adsorbed on graphene, consistent with a pure van der Waals interaction. FePc and CoPc instead show a high thermal stability, sign of a stronger interaction than a pure van der Waals. The reason of this difference lies in the different occupation of the $3d$ shell of the central metal atom of the MPcs: moving from molecules with mostly unfilled $3d$ shell, as FePc and CoPc, to molecules with more filled $3d$ shell, as CuPc, the metallic character of the molecular orbital is progressively reduced. Thus open shell MPcs at the SL-stage are more inclined to interact with the supporting substrate.

We determine also the growth mode of the molecular thin-film, which is consistent with a Stranski-Krastanov growth. This is the case of a balance between molecule-molecule and molecule-substrate interaction, since after the completion of the first monolayer an island growth takes place. This is an important achievement, which indicates a template-driven grown at the single-layer stage, different from the case of MPc adsorbed on graphite (HOPG) forming island even at low coverage. The difference with graphite is further highlighted in a thermal desorption experiment comparing the desorption temperature of adsorbed FePc onto the two substrates: it is definitively higher on graphene than on HOPG.

An important role played by graphene is the decoupling action between the underlying Ir metal substrate and the adsorbed molecules. The surface states of iridium are preserved upon adsorption of molecular thin-film when the graphene sheet is in between them, while direct adsorption onto the metal totally quenches these structures already at low coverage. Not only the substrate's surface properties are preserved, indeed graphene seems to induce an enhancement of the magnetic dichroism for a single-layer of FePc; non trivial behaviour of the orbital and spin moments as a function of coverage has been determined. In the perspective to design ordered nanoarchitechtures of molecules in which a single magnetic atom is embedded in an organic frame to exploit an ordered spin network, the moiré template of graphene/Ir(111) is thus a perfect candidate, trapping the molecules without corrupting their properties and, at the same time, leaving graphene almost unaffected by the metallic substrate.

The puzzling problem is then a subtle balance between molecule-molecule

and molecule-substrate interaction, where the morphology of the moiré pattern is a fundamental parameter but it is not the only driver of the interaction, since even the *d*-state occupation of the central metal atom of the MPc molecule determines the interaction strength. The flat monolayer of weakly interacting MPc molecules is then an ideal channel for conduction and doping by using substituted phthalocyanines, rendering it an organic buffer layer decoupled from the underlying metal.

A natural prosecution of this work is to extend of the study to other MPcs with different magnetic metallic center in order to discriminate the relationship between the spin state and molecular orbitals influenced by the graphene sheet. This study provides a procedure protocol to identify the best conditions to control the graphene properties in different environment and to define the best suitable substrate to design ordered nanoarchitechtures.

Bibliography

[1] K.S. Novoselov, A.K. Geim, S.V. Morozov, D. Jiang, Y. Zhang, S.V. Dubonos, I.V. Grigorieva, and A.A. Firsov. Electric Field Effect in Atomically Thin Carbon Films. *Science*, 306:666, 2004.

[2] K.S. Novoselov, D. Jiang, F. Schedin, T. J. Booth, V. V. Khotkevich, S. V. Morozov, and A.K. Geim. Two-Dimensional Atomic Crystals. *Proceedings of the National Academy of Sciences of the United States of America*, 102:10451, 2005.

[3] The Nobel Prize in Physics 2010
. *http://www.nobelprize.org/nobel_prizes/physics/laureates/2010/*.

[4] R.E. Peierls. Bemerkungen über Umwandlungstemperaturen. *Helvetica Physica Acta*, 7:81, 1934.

[5] R.E. Peierls. Quelques Proprietes Typiques des Corpses Solides. *Annales de l'Institut Henri Poincaré*, 5:177, 1935.

[6] L.D. Landau. Statistical Physics Part I. *Physikalische Zeitschrift der Sowjetunion*, 11:26, 1937.

[7] L.D. Landau and E.M. Lifshitz. Statistical Physics Part II. *Pergamon, Oxford, UK*, 1, 1980.

[8] N.D. Mermim. Crystalline Order in Two Dimensions. *Physical Review*, 176:250, 1968.

[9] N.D. Mermim and H. Wagner. Absence of Ferromagnetism or Antiferromagnetism in One- or Two-Dimensional Isotropic Heisenberg Models. *Physical Review Letters*, 17:1133, 1966.

[10] J.C. Meyer, A.K. Geim, M.I. Katsenelson, K.S. Novoselov, T.J. Booth, and S. Roth. The Structure of Suspended Graphene Sheets. *Nature*, 446:60, 2007.

[11] M. Posternak, A. Baldereschi, A. J. Freeman, E. Wimmer, and M. Weinert. Prediction of Electronic Interlayer States in Graphite and Reinterpretation of Alkali Bands in Graphite Intercalation Compounds. *Physical Review Letters*, 50:761, 1983.

[12] M.S. Dresselhaus and G. Dresselhaus. Intercalation Compounds of Graphite. *Advances in Physics*, 51:1, 2002.

[13] E.V. Rutkov and A.Y. Tontegode. A Study of the Carbon Adlayer on Iridium. *Surface Science*, 161:373, 1985.

[14] T.A. Land, T. Michely, R.J. Behm, J.C. Hemminger, and G. Comsa. STM Investigation of Single Layer Graphite Structures Produced on Pt(111) by Hydrocarbon Decomposition. *Surface Science*, 264:261, 1992.

[15] A. Nagashima, K. Nuka, H. Itoh, T. Ichinokawa, C. Oshima, and S. Otani. Electronic States of Monolayer Graphite Formed on TiC(111) Surface. *Surface Science*, 291:93, 1993.

[16] P.R. Wallace. The Band Theory of Graphite. *Physical Review*, 71:622, 1947.

[17] S. Reich, J. Multzsch, C. Thomsen, and P. Ordejón. Tight-Binding Description of Graphene. *Physical Review B*, 66:035412, 2002.

[18] A.H. Castro Neto, F. Guinea, N.M.R. Peres, K.S. Novoselov, and A.K. Geim. The Electronic Properties of Graphene. *Reviews of Modern Physics*, 81:109, 2009.

[19] A.K. Geim and A.H. MacDonald. Graphene: Exploring Carbon Flatland. *Physics Today*, 60:35, 2007.

[20] K.S. Novoselov, Z. Jiang, Y. Zhang, S.V. Morozav, H.L. Stormer, U. Zeitler, J.C. Maan, G.S. Boebiger, P. Kim, and A.K. Geim. Room Temperature Qantum Hall Effect in Graphene. *Science*, 315:1379, 2007.

[21] Y. Zhang, Y.-W. Tan, H.L. Stormer, and P. Kim. Experimental Observation of the Quantum Hall Effect and Berry's Phase in Graphene. *Nature*, 438:201, 2005.

[22] Y. Zhang, Z. Jiang, J.P. Small, M.S. Purewal, Y.-W. Tan, M. Fazlollahi, J.D. Chudow, J.A. Jaszczak, H.L. Stormer, and P. Kim. Landau-Level Splitting in Graphene in High Magnetic Fields. *Physical Review Letters*, 96:136806, 2006.

[23] M.I. Katsnelson, K.S. Novoselov, and A.K. Geim. Chiral Tunnelling and the Klein Paradox in Graphene. *Nature Physics*, 2:620, 2006.

[24] A.F. Young and P. Kim. Quantum Interference and Klein Tunnelling in Graphene Heterojunctions. *Nature Physics*, 5:222, 2009.

[25] V.V. Cheinov, V. Fal'ko, and B.L. Altshuler. The Focusing of Electron Flow and a Veselago Lens in Graphene p-n Junctions. *Science*, 315:1252, 2007.

[26] K.R. Knox, A. Locatelli, D. Yilmaz, A.B. Cvetko, T.O. Mentes, M.A. Nino, P. Kim, A. Morgante, and R.M. Osgood Jr. Making Angle-Resolved Photoemission Measurements on Corrugated Monolayer Crystals: Suspended Exfoliated Single-Crystal Graphene. *Physical Review B*, 84:115401, 2011.

[27] D.V. Badami. Graphitization of α-Silicon Carbide. *Nature*, 193:569, 1962.

[28] T. Seyller, A. Bostwick, K.V. Emtsev, K. Horn, L. Ley, J.L. McChesney, T. Ohta, J.D. Riley, E. Rotenberg, and F. Speck. Epitaxial Graphene: a New Material. *Physica Status Solidi B*, 245:1436, 2008.

[29] C. Berger, Z. Song, X. Li, X. Wu, N. Brown, C. Naud, D. Mayou, T. Li, J. Hass, A.N. Marchenkov, E.H. Conrad, P.N. First, and W. de Heer. Electronic Confinement and Coherence in Patterned Epitaxial Graphene. *Science*, 312:1191, 2006.

[30] A. Bostwick, J. McChesney, T Ohta, E. Rotenberg, T. Seyller, and K. Horn. Experimental Studies of the Electronic Structure of Graphene. *Progress in Surface Science*, 84:380, 2009.

[31] K.V. Emtsev, F. Speck, T. Seyller, L. Ley, and J.D Riley. Interaction, Growth, and Ordering of Epitaxial Graphene on SiC(0001) Surface: a Comparative Photoelectron Spectroscopy Study. *Physical Review B*, 77:155303, 2008.

[32] H. Lyon and G. Somorjai. Low-Energy Electron-Diffraction Study of the Clean (100), (111), and (110) Faces of Platinum. *The Journal of Chemical Physics*, 46:2539, 1967.

[33] J.W. May. Platinum Surface LEED Rings. *Surface Science*, 17:267, 1969.

[34] J. Wintterlin and M.-L. Bocquet. Graphene on Metal Surfaces. *Surface Science*, 603:1841, 2009.

[35] A. Bostwick, T. Ohta, J.L. McChesney, K.V. Emtsev, T. Seyller, K. Horn, and E. Rotenberg. Symmetry Breaking in Few Layer Graphene Films. *New Journal of Physics*, 9:385, 2007.

[36] C. Ederlein, Y.S. Kim, A. Bostwick, E. Rotenberg, and K. Horn. The Formation of an Energy Gap in Graphene on Ruthenium by Controlling the Interface. *New Journal of Physics*, 12:033014, 2010.

[37] A. Grüneis and D.V. Vyalikh. Tunable Hybridization between Electronic States of Graphene and a Metal Surface. *Physical Review B*, 77:193401, 2008.

[38] T. Brugger, S. Günther, B. Wang, J.H. Dil, M.-L. Bocquet, J. Osterwalder, J. Wintterlin, and T. Greber. Comparison of electronic structure and template function of single-layer graphene and a hexagonal boron nitride nanomesh on ru(0001). *Physical Review B*, 79:045407, 2009.

[39] P. Sutter, M.S. Hybertsen, J.T. Sadowski, and E. Sutter. Electronic Structure of Few-Layers Epitaxial Graphene on Ru(0001). *Nano letters*, 9:2654, 2009.

[40] I. Pletikosić, M. Kralj, P. Pervan, R. Brako, J. Coraux, A.T. N'Diaye, C. Busse, and T. Michely. Dirac Cones and Minigaps for Graphene on Ir(111). *Physical Review Letters*, 102:056808, 2009.

[41] A.B. Preobrajenski, M.L. Ng, A.S. Vinogradov, and N. Må rtensson. Controlling Graphene Corrugation on Lattice-Mismatched Substrates. *Physical Review B*, 78:073401, 2008.

[42] S. Rajasekaran, S. Kaya, T. Anniyev, H. Ogasawara, and A. Nilsson. Probing Substrate Effects in the Carbon-Projected Band Structure of Graphene on Pt(111) through Resonant Inelastic X-Ray Scattering. *Physical Review B*, 85:045419, 2012.

[43] S. Marchini, S. Günther, and J. Wintterlin. Scanning Tunneling Microscopy of Graphene on Ru(0001). *Physical Review B*, 76:075429, 2007.

[44] B. Wang, M.-L. Bocquet, S. Marchini, S. Günther, and J. Wintterlin. Chemical Origin of a Graphene Moiré Overlayer on Ru(0001). *Physical Chemistry Chemical Physics*, 10:3530, 2008.

[45] M.M. Ugeda, D. Fernández-Torre, I. Brihuega, P. Pou, A.J. Martínez-Galera, Rubén Pérez, and J.M. Gómez-Rodríguez. Point Defects on Graphene on Metals. *Physical Review Letters*, page 116803, 2011.

[46] A.T. N'Diaye, J. Coraux, T.N. Plasa, C. Busse, and T. Michely. Structure of Epitaxial Graphene on Ir(111). *New Journal of Physics*, 10:043033, 2008.

[47] Y. Pan, H. Zhang, D. Shi, J. Sun, S. Du, F. Liu, and H.-J. Gao. Highly Ordered, Millimeter-Scale, Continuous, Single-Crystalline Graphene Monolayer Formed on Ru (0001). *Advanced Materials*, 21:2777, 2009.

[48] W. Moritz, B. Wang, M. L. Bocquet, T. Brugger, T. Greber, J. Wintterlin, and S. Günther. Structure Determination of the Coincidence Phase of Graphene on Ru(0001). *Physical Review Letters*, 104:136102, 2010.

[49] Z. Sun, S.K. Hämäläinen, J. Sainio, J. Lahtinen, D. Vanmaekelbergh, and P. Liljeroth. Topographic and electronic contrast of the graphene moiré on ir(111) probed by scanning tunneling microscopy and noncontact atomic force microscopy. *Physical Review B*, 83:081415, 2011.

[50] C. Busse, P. Lazić, R. Djemour, J. Coraux, T. Gerber, N. Atodiresei, V. Caciuc, R. Brako, A.T. N'Diaye, S. Blügel, J. Zegenhagen, and T. Michely. Graphene on ir(111): Physisorption with chemical modulation. *Physical Review Letters*, 107:036101, 2011.

[51] C. Lee, X. Wei, J.W. Kysar, and J. Hone. Measurement of the Elastic Properties and Intrinsic Strength of Monolayer Graphene. *Science*, 321:385, 2008.

[52] V. Juvé, M. Scardamaglia, P. Maioli, A. Crut, S. Merabia, L. Joly, N. Del Fatti, and F. Valleé. Cooling Dynamics and Thermal Interface Resistance of Glass-Embedded Metal Nanoparticles. *Physical Review B*, 80:195406, 2009.

[53] R. Mahajan, C. P. Chiu, and G. Chrysler. Cooling a Microprocessor Chip. *Proceedings of the IEEE*, 94:1476, 2006.

[54] Y. Yang, W. Liu, and M. Asheghi. Thermal and Electrical Characterization of Cu/CoFe Superlattices. *Applied Physics Letters*, 84:3121, 2004.

[55] J.H. Seol, I. Jo, A.L. Moore, L. Lindsay, Z.H. Aitken, M.T. Petters, X. Li, Z. Yao, R. Huang, D. Broido, N. Mingo, R.S. Ruoff, and L. Shi. Two-Dimensional Phonon Transport in Supported Graphene. *Science*, 328:213, 2008.

[56] A.A. Balandin, S. Ghosh, W. Bao, I. Calizo, D. Teweldebrhan, F. Miao, and C. N. Lau. Superior Thermal Conductivity of Single-Layer Graphene. *Nano Letters*, 8:902, 2008.

[57] A.K. Geim and K.S. Novoselov. The Rise of Graphene. *Nature materials*, 6:183, 2007.

[58] K.S. Novoselov, A.K. Geim, S.V. Morozov, D. Jiang, M.I. Katsnelson, I.V. Grigorieva, S.V. Dubonos, and A.A. Firsov. Two-Dimensional Gas of Massless Dirac Fermions in Graphene. *Nature*, 438:197, 2005.

[59] A. K. Geim. Graphene: Status and Prospects. *Science*, 324:1530, 2009.

[60] Y.M. Lin, K.A. Jenkins, A. Valdes-Garcia, J.P. Small, D.B. Farmer, and P. Avouris. Operation of Graphene Transistors at Gigahertz Frequencies. *Nano Letters*, 9:422, 2009.

[61] N. Tombros, C. Jozsa, M. Popinciuc, H.T. Jonkman, and B.J. van Wees. Electronic Spin Transport and Spin Precession in Single Graphene Layers at Room Temperature. *Nature*, 448:571, 2007.

[62] F. Schedin, A.K. Geim, S.V. Morozov, E.W. Hill, P. Blake, M.I. Katsnelson, and K.S. Novoselov. Detection of Individual Gas Molecules Adsorbed on Graphene. *Nature materials*, 6:652, 2007.

[63] H. Meiling, J.P. Benschop, U. Dinger, and P. Kuerz. Progress of the EUVL Alpha Tool. *Proc SPIE, Emerging Lithographic Technologies V*, 4343:38, 2001.

[64] V. Bakshi, R. Lebert, B. Jaegle, A. Wies, U. Stamm, J. Kleinschmidt, G. Schriever, C. Ziener, M. Corthout, J. Pankert, K. Bergmann, W. Neff, A. Egbert, and D. Gustafson. Status Report on EUV Source Development and EUV Source Applications in EUVL. *Mask and Lithography Conference (EMLC) 23rd European*, 2007.

[65] G.E. Moore. Progress in Digital Integrated Electronics. *IEEE IEDM Technical Digest*, 21:11, 1975.

[66] A. Facchetti. Semiconductors for Organic Transistors. *Materials Today*, 10:28, 2007.

[67] H.B. Weber, J. Reichert, F. Weigend, R. Ochs, D. Beckmann, M. Mayor, Ahlrichs R., and H.V. Löhneysen. Electronic Transport Through a Single Conjugated Molecule. *Chemical Physics*, 281:113, 2002.

[68] L. Zuppiroli, M.N. Bussac, S. Paschen, O. Chauvet, and L. Forro. Hopping in Disordered Conducting Polymers. *Physical Review B*, 50:5196, 1994.

[69] I.G. Hill, A. Kahn, Z.G. Soos, and R.A. Pascal. Charge-Separation Energy in Films of π-Conjugated Organic Molecules. *Chemical Physics Letters*, 327:181, 2000.

[70] P.P. Ruden and D.L. Smith. Theory of Spin Injection into Conjugated Organic Semiconductors. *Journal of Applied Physics*, 95:4898, 2004.

[71] O.D. Jurchescu, M. Popinciuc, B.J. van Wees, and T.T.M. Palstra. Interface Controlled High Mobility Organic Transistors. *Advanced Materials*, 19:688, 2007.

[72] C.C. Leznoff and A.B.P. Lever. Phthalocyanines: Properties and Applications. *VCH, Weinheim*, 1993.

[73] K. Walzer, B. Maennig, M. Pfeiffer, and K. Leo. Highly Efficient Organic Devices Based on Electrically Doped Transport Layers. *Chemical Reviews*, 107:1233, 2007.

[74] P. Gregory. Applications of Phthalocyanines. *Journal of Porphyrins and Phthalocyanines*, 4:432, 2000.

[75] R.D. Yang, J. Park, C.N. Colesniuc, I.K. Schuller, J.E. Royer, W.C. Trogler, and A.C. Kummel. Analyte Chemisorption and Sensing on n- and p-Channel Copper Phthalocyanine Thin-Film Transistors. *The Journal of Chemical Physics*, 130:164703, 2009.

[76] W. Chan, J.F. Marshall, G.Y.F. Lam, and I.R. Hart. Tissue Uptake, Distribution, and Potency of the Photoactivatable Dye Chloraluminum Sulfonated Phthalocyanine in Mice Bearing Transplantable Tumors. *Cancer Research*, 48:3040, 1988.

[77] S.A. Van Slyke, C.H. Chen, and C.W. Tang. Organic Electroluminescent Devices with Improved Stability. *Applied Physics Letters*, 69:2160, 1996.

[78] M.-M. Ling and Z. Bao. Organic Electroluminescent Devices with Improved Stability. *Organic Electronics*, 7:568, 2006.

[79] P. Peumans and S.R. Forrest. Very-High-Efficiency Double-Heterostructure Copper Phthalocyanine/C_{60} Photovoltaic Cells. *Applied Physics Letters*, 79:126, 2001.

[80] A.B.P. Lever. The Phthalocyanines. *Advances in Inorganic and Radiochemistry*, 27:27, 1965.

[81] M. Evangelisti, J. Bartolomé, L.J. de Jongh, and G. Filoti. Magnetic Properties of α-Iron(II) Phthalocyanine. *Physical Review B*, 66:144410, 2006.

[82] L. Gao, W. Ji, Y.B. Hu, Z.H. Cheng, Z.T. Deng, Q. Liu, N. Jiang, X. Lin, W. Guo, S.X. Du, W.A. Hofer, X.C. Xie, and H.-J. Gao. Site-Specific Kondo Effect at Ambient Temperatures in Iron-Based Molecules. *Physical Review Letter*, 99:106402, 2007.

[83] S.M. Heutz, C. Mitra, W. Wu, A.J. Fisher, A. Kerridge, A.M. Stoneham, A.H. Harker, J. Gardener, H.H. Tseng, T.S. Jones, C. Renner, and G. Aeppli. Molecular Thin Films: a New Type of Magnetic Switch. *Advanced Materials*, 19:3618, 2007.

[84] W.J.M. Naber, S. Faez, and W.G. van der Wiel. Organic Spintronics. *Journal of Physics D: Applied Physics*, 40:R205, 2007.

[85] M.-S. Liao, J.D. Watts, and M.-J. Huang. DFT Study of Unligated and Ligated ManganeseII Porphyrins and Phthalocyanines. *Inorganic Chemistry*, 44:1941, 2005.

[86] P. Gargiani, M. Angelucci, C. Mariani, and M.G. Betti. Metal-Phthalocyanine Chains on the Au(110) Surface : Interaction States Versus d-Metal States Occupancy. *Physical Review B*, 81:085412, 2010.

[87] I. Kröger, B. Stadtmüller, C. Stadler, J. Ziroff, M. Kochler, A. Stahl, F. Pollinger, T.-L. Lee, J. Zegenhagen, F. Reinert, and C. Kumpf. Submonolayer Growth of Copper-Phthalocyanine on Ag(111). *New Journal of Physics*, 12:083038, 2010.

[88] E. Annese, J. Fujii, I. Vobornik, and G. Rossi. Structure and Electron States of Cophthalocyanine Interacting With the Cu(111) Surface. *The Journal of Physical Chemistry C*, 115:17409, 2011.

[89] F. Petraki, H. Peisert, F. Latteyer, U. Ayg, A. Vollmer, and T. Chass. Impact of the 3d Electronic States of Cobalt and Manganese Phthalocyanines on the Electronic Structure at the Interface to Ag(111). *The Journal of Physical Chemistry C*, (111):21334, 2011.

[90] C. Vo-Van, S. Schumacher, J. Coraux, V. Sessi, O. Fruchart, N.B. Brookes, P. Ohresser, and T. Michely. Magnetism of cobalt nanoclusters on graphene on iridium. *Applied Physics Letters*, 99:142504, 2011.

[91] J. Moser, A. Verdaguer, D. Jiméez, A. Barreiro, and A. Bachtold. The Environment of Graphene Probed by Electrostatic Force Microscopy. *Applied Physics Letters*, 92:123507, 2008.

[92] H.G. Zhang, J.T. Sun, T. Low, L.Z. Zhang, Y. Pan, Q. Liu, J.H. Mao, H.T. Zhou, H.M. Guo, S.X. Du, F. Guinea, and H.-J. Gao. Assembly of Iron Phthalocyanine and Pentacene Molecules on a Graphene Monolayer Grown on Ru(0001). *Physical Review B*, 84:245436, 2011.

[93] J. Mao, H. Zhang, Y. Jiang, Y. Pan, M. Gao, W. Xiao, and H.-J. Gao. Tunability of Supramolecular Kagome Lattices of Magnetic Phthalocyanines using Graphene-Based Moire Patterns as Templates. *Journal of the American Chemical Society*, 131:14136, 2009.

[94] H. Zhang, W.D. Xiao, J. Mao, H. Zhou, G. Li, L. Zhang, L. Liu, S. Du, and H.-J Gao. Host-Guest Superstructures on Graphene-Based Kagome Lattice. *The Journal of Physical Chemistry C*, 116:11091, 2012.

[95] Y.H. Mao, R. Wang, Y. Wang, T. Chao Niu, J. Qiang Zhong, M. Yang Huang, D. Chen Qi, K. Ping Loh, A. Thye Shen Wee, and W. Chen. Chemical Vapor Deposition Graphene as Structural Template to Control Interfacial Molecular Orientation of Chloroaluminium Phthalocyanine. *Applied Physics Letters*, 99:093301, 2011.

[96] K. Yang, W. Xiao, Y. Jiang, H. Zhang, L.W. Liu, J. Mao, H. Zhou, S. Du, and H.-J. Gao. Molecule-Substrate Coupling between Metal Phthalocyanines and Epitaxial Graphene Grown on Ru(0001) and Pt(111). *The Journal of Physical Chemistry C*, 116:26, 2012.

[97] W. Dou, S. Huang, R.Q. Zhang, and C.S. Lee. Molecule-Substrate Interaction Channels of Metal-Phthalocyanines on Graphene on Ni(111) Surface. *The Journal of Chemical Physics*, 134:094705, 2011.

[98] SuperESCA beamline description. *http://www.elettra.trieste.it*.

[99] ID08 - Dragon Beamline. *http://www.esrf.eu*.

[100] M.P. Seah and W.A. Dench. Quantitative Electron Spectroscopy of Surfaces: a Standard Data Base for Electron Inelastic Mean Free Paths in Solids. *Surface and Interface Analysis*, 1:2, 1979.

[101] A. Einstein. Concerning an Heuristic Point of View Toward the Emission and Transformation of Light. *Annalen der Physik*, 17:132, 1905.

[102] G. Grimvall. The Electron-Phonon Interaction in Normal Metals. *Physica Scripta*, 14:63, 1976.

[103] R. Matzdorf. Investigation of Line Shapes and Line Intensities by High-Resolution UV-Photoemission Spectroscopy -Some Case Studies on Noble-Metal Surfaces. *Surface Science Reports*, 30:153, 1998.

[104] G. Grimvall. The Electron-Phonon Interaction in Metals. *North-Holland edition*, 1981.

[105] J. Stöhr, K. Baberschke, R. Jaeger, R. Treichler, and S. Brennan. Orientation of Chemisorbed Molecules from Surface-Absorption Fine-Structure Measurements: CO and NO on Ni(100). *Physical Review Letters*, 47:381, 1981.

[106] J. Stöhr. NEXAFS Specroscopy. *Springer series in surface science. Springer-Verlag, Berlin*, 1992.

[107] H. Ebert. Magneto-Optical Effects in Transition Metal Systems. *Reports on Progress in Physics*, 59:1665, 1996.

[108] F. Groot and A. Kotani. Core Level Spectroscopy of Solids. *Advances in condensed matter science, CRC Press*, 2008.

[109] A. Baraldi, G. Comelli, S. Lizzit, D. Cocco, G. Paolucci, and R. Rosei. Temperature Programmed X-Ray Photoelectron Spectroscopy: a New Technique for the Study of Surface Kinetics. *Surface Science Letters*, 367:L67, 1996.

[110] A. Baraldi, G. Comelli, S. Lizzit, M. Kiskinova, and G. Paolucci. Real-Time X-Ray Photoelectron Spectroscopy of Surface Reactions. *Surface Science Reports*, 49:169, 2003.

[111] K.A. Fichthorn and R.A. Miron. Thermal Desorption of Large Molecules from Solid Surfaces. *Physical Review Letters*, 89:196103, 2002.

[112] H. Ulbricht, R. Zacharia, N. Cindir, and T. Hertel. Thermal Desorption of Gases and Solvents from Graphite and Carbon Nanotube Surfaces. *Carbon*, 44:2931, 2006.

[113] M. Roos, D. Künzel, B. Uhl, H. Huang, O.B. Alves, H.E. Hoster, A. Gross, and R.J. Behm. Hierarchical Interactions and Their Influence Upon the Adsorption of Organic Molecules on a Graphene Film. *Journal of the American Chemical Society*, 133:9208, 2011.

[114] S. Lizzit and A. Baraldi. High-Resolution Fast X-Ray Photoelectron Spectroscopy Study of Ethylene Interaction with Ir(111): From Chemisorption to Dissociation and Graphene Formation. *Catalysis Today*, 154:68, 2010.

[115] G. Ehrlich. Thermal Desorption of Gases. *Journal of Applied Physics*, 32:4, 1961.

[116] P. A. Redhead. Thermal Desorption of Gases. *Vacuum*, 12:203, 1962.

[117] G. Carter. Thermal Resolution of Desorption Energy Spectra. *Vacuum*, 12:245, 1962.

[118] M. Polanyi and E. Wigner. Über die Interferenz von Eigenschwingungen als Ursache von Energieschwankungen und chemischer Umsetzungen. *eitschrift für Physikalische Chemie*, 139:439, 1928.

[119] C. Struzzi. Energetica di Adsorbimento di Film Sottili di Molecole Organiche: la Ferro-Ftalocianina su Grafene. *Master's Thesis*, 2012.

[120] E. Kautto, J. Kuhalainen, and M. Manninen. Analysing Methods for Thermal Desorption Spectra. *Physica Scripta*, 1997.

[121] NIST Chemistry WebBook. *http://webbook.nist.gov/chemistry*.

[122] E. Loginova, N.C. Bartelt, P.J. Feibelman, and K.F. McCarty. Factors Influencing Graphene Growth on Metal Surfaces. *New Journal of Physics*, 11:063046, 2009.

[123] T.S. Marinova and K.L. Kostov. Adsorption of Acetylene and Ethylene on a Clean Ir(111) Surface. *Surface Science*, 181:573, 1987.

[124] E. Nieuwenhuys, G. Rovida, D.I. Hagen, and G.A. Somoraj. LEED, AES and Thermal Desorption Studies of Chemisorbed Hydrogen and Hydrocarbons (C_2H_2, C_2H_4, C_6H_6, C_6H_{12}) on (111) and Stepped [6(111)×(100)] Iridium Crystal-Surface-Comparison with Platinum. *Surface Science*, 59:155, 1976.

[125] M. Kralj, I. Pletikosić, M. Petrović, P. Pervan, M. Milun, A.T. N'Diaye, C. Busse, T. Michely, J. Fujii, and I. Vobornik. Graphene on Ir(111) Characterized by Angle-Resolved Photoemission. *Physical Review B*, 84:075427, 2011.

[126] H. Hattab, A.T. N'Diaye, D. Wall, G. Jnawali, J. Coraux, C. Busse, R. van Gastel, B. Poelsema, T. Michely, F.-J. Meyer zu Heringdorf, and M. Horn-von Hoegen. Growth Temperature Dependent Graphene Alignment on Ir(111). *Applied Physics Letters*, 98:141903, 2011.

[127] A. Varykhalov, D. Marchenko, M. R. Scholz, E. D. L. Rienks, T. K. Kim, G. Bihlmayer, J. Sánchez-Barriga, and O. Rader. Ir(111) Surface State with Giant Rashba Splitting Persists under Graphene in Air. *Physical Review Letters*, 108(6):066804, February 2012.

[128] H.J. Wagner, R.O. Loutfy, and C-.K. Hsiao. Purification and Characterization of Phthalocyanines. *Journal of Materials Science*, 17:2781, 1982.

[129] J. Coraux, A.T. N'Diaye, C. Busse, and T. Michely. Structural Coherency of Graphene on Ir(111). *Nano Letters*, 8:565, 2007.

[130] P. Eckerlin and H. Kandler. Group III: Condensed Matter, volume 6 of Landolt-Börnstein: Numerical Data and Functional Relationships in Science and Technology - New Series. *Springer-Verlag*, 1971.

[131] A.T. N'Diaye, S. Bleikamp, P.J. Feibelman, and T. Michely. Two-Dimensional Ir Cluster Lattice on a Graphene Moiré on Ir(111). *Physical Review Letters*, 97:215501, 2006.

[132] J. Knudsen, P.J. Feibelman, T. Gerber, E. Grånäs, K. Schulte, P. Stratmann, Andersen J.N., and T. Michely. Cluster Binding to the Graphene Moiré on Ir(111): X-ray Photoemission Compared to Density Functional Calculations. *Physical Review B*, 85:035407, 2012.

[133] R.A. Rosenberg, P.J. Love, and Victor Rehn. Polarization-dependent C(K) Near-Edge X-ray-Absorption Fine Structure of Graphite. *Physical Review B*, 44:4034, 1985.

[134] V.L. Joseph Joly, M. Kiguchi, S.-J. Hao, K. Takai, T. Enoki, R. Sumii, K. Amemiya, H. Muramatsu, T. Hayashi, Y.A. Kim, M. Endo, J. Campos-Delgado, F. López-Urías, A. Botello-Méndez, H. Terrones, M. Terrones, and M.S. Dresselhaus. Observation of Magnetic Edge State in Graphene Nanoribbons. *Physical Review B*, 44:245428, 2010.

[135] S. Entani, S. Ikeda, M. Kiguchi, K. Saiki, G. Yoshikawa, I. Nakai, H. Kondoh, and T. Ohta. Growth of Nanographite on Pt(111) and its Edge State. *Applied Physics Letters*, 88:153126, 2006.

[136] K. Nakada, M. Fujita, G. Dresselhaus, and M.S. Dresselhaus. Edge State in Graphene Ribbons: Nanometer Size Effect and Edge Shape Dependence. *Physical Review B*, 54:17954, 1996.

[137] D. Pacilé, M. Papagno, A. Fraile Rodríguez, M. Grioni, and L. Papagno. Near-Edge X-Ray Absorption Fine-Structure Investigation of Graphene. *Physical Review Letters*, 101:066806, 2008.

[138] M. Papagno, A. Fraile Rodríguez, Ç.Ö. Girit, J. C. Meyer, A. Zettl, and D. Pacilé. Polarization-Dependent C K Near-Edge X-Ray Absorption Fine-Structure of Graphene. *Chemical Physics Letters*, 475:269, 2009.

[139] S.B. Trickey, F. Müller-Plathe, and G.H.F. Diercksen. Interplanar Binding and Lattice Relaxation in a Graphite Dilayer. *Physical Review B*, 45:4460, 1992.

[140] V.N. Strocov, P. Blaha, H.I. Starnberg, M. Rohlfing, R. Claessen, J.-M. Debever, and J.-M. Themlin. Three-Dimensional Unoccupied Band Structure of Graphite: Very-Low-Energy Electron Diffraction and Band Calculations. *Physical Review B*, 61, 2004.

[141] V. Silkin, J. Zhao, F. Guinea, E. Chulkov, P. Echenique, and H. Petek. *Physical Review B*.

[142] J. Kikuma, K. Yoneyama, M. Nomura, T. Konishi, T. Hashimoto, R. Mitsumoto, Y. Ohuchi, and K. Seki. Cluster binding to the Graphene Moiré on Ir(111): X-ray Photoemission Compared to Density Functional Calculations. *Journal of Electron Spectroscopy and Related Phenomena*, 88:919, 1998.

[143] H.-K. Jeong, H.-J. Noh, J.-Y. Kim, L. Colakerol, P.-A. Glans, M.H. Jin, K.E. Smith, and Y.H. Lee. Comment on "Near-Edge X-Ray Absorption Fine-Structure Investigation of Graphene". *Physical Review Letters*, 102:099701, 2009.

[144] V. Lee, C. Park, C. Jaye, D. A. Fischer, Q. Yu, W. Wu, Z. Liu, J. Bao, S.-S Pei, C. Smith, P. Lysaght, and S. Banerjee. Substrate Hybridization and Rippling of Graphene Evidenced by Near-Edge X-ray Absorption Fine Structure Spectroscopy. *The journal of physical chemistry letters*, 1:1247, 2010.

[145] Y. S. Dedkov, M. Sicot, and M. Fonin. X-Ray Absorption and Magnetic Circular Dichroism of Graphene/Ni(111). *Journal of Applied Physics*, 107:09E121, 2010.

[146] J. Tang, C.Y. Kang, L.M. Li, W.S. Yan, S.Q. Wei, and P.S. Xu. Graphene Films Grown on Si Substrate via Direct Deposition of Solid-State Carbon Atoms. *Physica E: Low-dimensional Systems and Nanostructures*, 43:1415, 2011.

[147] S. Doniach and M. Šunjić. Many-electron Singularity in X-ray Photoemission and X-ray Line Spectra from Metals. *Journal of Physics C: Solid State Physics*, 3:285, 1970.

[148] P. Lacovig, M. Pozzo, D. Alfè, P. Vilmercati, A. Baraldi, and S. Lizzit. Growth of Dome-Shaped Carbon Nanoislands on Ir(111): The Intermediate between Carbidic Clusters and Quasi-Free-Standing Graphene. *Physical Review Letters*, 103:166101, 2009.

[149] S. Lizzit, G. Zampieri, L. Petaccia, R. Larciprete, P. Lacovig, E. D. L. Rienks, G. Bihlmayer, A. Baraldi, and P. Hofmann. Band Dispersion in the Deep 1s Core Level of Graphene. *Nature Physics*, 6:345, 2010.

[150] J.F. van der Veen, F.J. Himpsel, and D.E. Eastman. Structure-Dependent 4f-Core-Level Binding Energies for Surface Atoms on Ir(111), Ir(100)-(5x1), and Metastable Ir(100)-(1x1). *Physical Review Letters*, 44:189, 1980.

[151] M. Bianchi, D. Cassese, A. Cavallin, R. Comin, F. Orlando, L. Postregna, E. Golfetto, S. Lizzit, and A. Baraldi. Surface Core Level Shifts of Clean and Oxygen Covered Ir(111). *New Journal of Physics*, 11:063002, 2009.

[152] A. Baraldi. Structure and Chemical Reactivity of Transition Metal Surfaces as Probed by Synchrotron Radiation Core Level Photoelectron Spectroscopy. *Journal of Physics: Condensed Matter*, 20:093001, 2008.

[153] E.L. Shirley, L.J. Terminello, A. Santoni, and F.J. Himpsel. Brillouin-Zone-Selection Effects in Graphite Photoelectron Angular Distributions. *Physical Review B*, 51:13614, 1995.

[154] M. Mucha-Kruczyński, O. Tsyplyatyev, A. Grishin, E. McCann, V. I. Fal'ko, A. Bostiwick, and E. Rotenberg. Characterization of Graphene Through Anisotropy of Constant-Energy Maps in Angle-Resolved Photoemission. *Physical Review B*, 77:195403, 2008.

[155] F. Kuemmeth and E.I. Rashba. Giant Spin Rotation Under Quasiparticle-Photoelectron Conversion: Joint Effect of Sublattice Interference and Spin-Orbit Coupling. *Physical Review B*, 80:241409(R), 2009.

[156] W.S. Jung, C.S. Leem, C. Kim, S.R. Park, S.Y. Park, B.J. Kim, E. Rotenberg, and C. Kim. Imaging the Electron Density in Solids by Using Multi-Brillouin-Zone Angle Resolved Photoelectron Spectroscopy. *Physical Review B*, 82:235105, 2010.

[157] I. Gierz, J. Henk, H. Höchst, C.R. Ast, and K. Kern. Illuminating the Dark Corridor in Graphene: Polarization Dependence of Angle-Resolved Photoemission Spectroscopy on Graphene. *Physical Review B*, 83:121408(R), 2011.

[158] S.V. Morozov, K.S. Novoselov, M.I. Katsnelson, F. Schedin, L.A. Ponomarenko, D. Jiang, and A.K. Geim. Strong Suppression of Weak Localization in Graphene. *Physical Review Letters*, 97:016801, 2006.

[159] C. Hwang, C.-H. Park, D.A. Siegel, A.V. Fedorov, S.G. Louie, and A. Lanzara. Direct Measurement of Quantum Phases in Graphene via Photoemission Spectroscopy. *Physical Review B*, 83:125422(R), 2011.

[160] Y. Liu, G. Bian, T. Miller, and T.-C. Chiang. Visualizing Electronic Chirality and Berry Phases in Graphene Systems Using Photoemission with Circularly Polarized Light. *Physical Review Letters*, 107:166803, 2011.

[161] I. Gierz, M. Lindroos, H. Höchst, C.R. Ast, and K. Kern. Graphene Sublattice Symmetry and Isospin Determined by Circular Dichroism in Angle-Resolved Photoemission Spectroscopy. *Nano Letters*, 12:3900, 2012.

[162] E. Starodub, A. Bostwick, L. Moreschini, S. Nie, F. Gabaly, K. McCarty, and E. Rotenberg. In-Plane Orientation Effects on the Electronic Structure, Stability, and Raman Scattering of Monolayer Graphene on Ir(111). *Physical Review B*, 83:125428, 2011.

[163] S. Rusponi, M. Papagno, P. Moras, S. Vlaic, M. Etzkorn, P. Sheverdyaeva, D. Pacilé, H. Brune, and C. Carbone. Highly Anisotropic Dirac Cones in Epitaxial Graphene Modulated by an Island Superlattice. *Physical Review Letters*, 105:246803, 2010.

[164] I. Pletikosić, M. Kralj, D. Šokčević, R. Brako, P. Lazić, and P. Pervan. Photoemission and Density Functional Theory Study of Ir(111); Energy Band Gap Mapping. *J. Phys.: Condens. Matter*, 22:135006, 2010.

[165] M. Bianchi, E. D. L. Rienks, S. Lizzit, a. Baraldi, R. Balog, L. Hornekæ r, and Ph. Hofmann. Electron-Phonon Coupling in Potassium-Doped Graphene: Angle-Resolved Photoemission Spectroscopy. *Physical Review B*, 81:041403(R), 2010.

[166] M.K. Brinkley, G. Bian, T. Miller, Y. Liu, L. Zhang, and T.-C Chiang. Phonon-Induced Gaps in Graphene and Graphite Observed by Angle-Resolved Photoemission. *Physical Review Letters*, 105:136804, 2010.

[167] V. Tewary and B. Yang. Singular Behavior of the Debye-Waller Factor of Graphene. *Physical Review B*, 79:125416, 2009.

[168] A. Politano, B. Borca, M. Minniti, J. Hinarejos, A. Vazquez de Parga, D. Farias, and R. Miranda. Helium Reflectivity and Debye Temperature of Graphene Grown Epitaxially on Ru(0001). *Physical Review B*, 84:035450, 2011.

[169] A. Bostwick, T. Ohta, J.L. McChesney, T. Seyller, K. Horn, and E. Rotenberg. Renormalization of Graphene Bands by Many-Body Interactions. *Solid State Communications*, 143:63, 2007.

[170] J.A. Venables. Nucleation and Growth Processes in Thin Film Formation. *Journal of Vacuum Science and Technology B*, 4:870, 1986.

[171] H. Lüth. Solid Surfaces, Interfaces and Thin Films. *Fourth edition, Springer*, 2001.

[172] E. Bauer and H. Poppa. Recent Advances in Epitaxy. *Thin Solid Films*, 12:167, 1972.

[173] A. Calabrese, L. Floreano, A. Verdini, C. Mariani, and M.G. Betti. Filling Empty States in a CuPc Single Layer on the Au (110) Surface via Electron Injection. *Physical Review B*, 79:115446, 2009.

[174] M.G. Betti, P. Gargiani, R. Frisenda, R. Biagi, A. Cossaro, A. Verdini, L. Floreano, and C. Mariani. Localized and Dispersive Electronic States at Ordered FePc and CoPc Chains on Au(110). *Journal of Physical Chemistry C*, 114:21638, 2010.

[175] S.K. Hämäläinen, M. Morozova, R. Drost, P. Liljerot, J. Lahtinen, and J. Sainio. Self-Assembly of Cobalt-Phthalocyanine Molecules on Epitaxial Graphene on Ir(111). *The Journal of Physical Chemistry C*, Just Accepted Manuscript, 2012.

[176] S. Bouvron, P. Erler, E. Cavar, and M. Fonin. Low Temperature Scanning Tunneling Microscopy Study of Co.Phthalocyanine Molecules on Graphene/Ir(111). *Poster presented at CMD-24, ECOSS-29 Conference, Edinburgh*, 2012.

[177] C. Isvoranu, J. Åhlund, B. Wang, E. Ataman, N. Mårtensson, C. Puglia, J. N. Andersen, M.-L. Bocquet, and J. Schnadt. Electron Spectroscopy Study of the Initial Stages of Iron Phthalocyanine Growth on Highly Oriented Pyrolitic Graphite. *The Journal of chemical physics*, 131:214709, 2009.

[178] W. Chen, H. Huang, S. Chen, X.Y. Gao, and A.T.S. Wee. Low-Temperature Scanning Tunneling Microscopy and Near-Edge X-Ray Absorption Fine Structure Investigations of Molecular Orientation of Copper(II) Phthalocyanine Thin Films at Organic Heterojunction Interfaces. *The Journal of Physical Chemistry C*, 112:5036, 2008.

[179] L. Ottaviano, S. Di Nardo, L. Lozzi, M. Passacantando, P. Picozzi, and S. Santucci. Thin and Ultra-Thin Films of Nickel Phthalocyanine Grown on Highly Oriented Pyrolitic Graphite: an XPS, UHV-AFM and Air-Tapping Mode AFM Study. *Surface Science*, 373:318, 1997.

[180] A Cossaro, D Cvetko, G Bavdek, L Floreano, R Gotter, and A Morgante. Copper-Phthalocyanine Induced Reconstruction of Au (110). *Journal of Physical Chemistry B*, 108:14671, 2004.

[181] X. Lu, K.W. Hipps, X.D. Wang, and U. Mazur. Scanning Tunneling Microscopy of Metal Phthalocyanines: d^7 and d^9 cases. *Journal of American Chemical Society*, 118:7197, 1996.

[182] X. Lu and K.W. Hipps. Scanning Tunneling Microscopy of Metal Phthalocyanines: d^6 and d^8 cases. *The Journal of Physical Chemistry B*, 101:5391, 1997.

[183] T. Takami, C. Carrizales, and K. Hipps. Commensurate Ordering of Iron Phthalocyanine on Ag(111) Surface. *Surface Science*, 603:3201, 2009.

[184] C. Isvoranu, J. Knudsen, E. Ataman, K. Schulte, B. Wang, M.-L. Bocquet, J.N. Andersen, and J. Schnadt. Adsorption of Ammonia on Multilayer Iron Phthalocyanine. *The Journal of Chemical Physics*, 134:114711, 2011.

[185] F. Evangelista, A. Ruocco, R. Gotter, A. Cossaro, L. Floreano, A. Morgante, F. Crispoldi, M. G. Betti, and C. Mariani. Electronic States of CuPc Chains on the Au(110) Surface. *The Journal of chemical physics*, 131:174710, 2009.

[186] N. Papageorgiou, E. Salomon, T. Angot, J.-M. Layet, L. Giovanelli, and G.L. Lay. Physics of Ultra-Thin Phthalocyanine Films on Semiconductors. *Progress in Surface Science*, 77(5-8):139–170, January 2004.

[187] A. Ruocco, F. Evangelista, R. Gotter, A. Attili, and G. Stefani. Evidence of Charge Transfer at the Cu-phthalocyanine / Al(100) Interface. *Journal of Physical Chemistry C*, 112:2016–2025, 2008.

[188] M.G. Betti, P. Gargiani, C. Mariani, S. Turchini, N. Zema, S. Fortuna, A. Calzolari, and S. Fabris. Formation of Hybrid Electronic States in FePc Chains Mediated by the Au(110) Surface. *The Journal of Physical Chemistry C*, 116:8657–8663, 2012.

[189] M. Grobosch, C. Schmidt, R. Kraus, and M. Knupfer. Electronic Properties of Transition Metal Phthalocyanines: The Impact of the Central Metal Atom (d5-d10). *Organic Electronics*, 11(9):1483–1488, September 2010.

[190] T.E. Gallon. A Simple Model for the Dependence of Auger Intensities on Specimen Thickness. *Surface Science*, 17:486, 1969.

[191] G.R. Rhead, M.G. Barthès, and C. Argile. Determination of Growth Modes of Ultrathin Films from Auger Electron Spectroscopy: an Assessment and Commentary. *Thin Solid Films*, 82:201, 1972.

[192] J.A. Venables, G.D.T. Spiller, and M. Hanbücken. Nucleation and Growth of Thin Films. *Reports on Progress in Physics*, 47:399, 1984.

[193] G. Forte. Grafene su Ir(111): uno Studio di Fotoemissione. *Master's Thesis*, 2010.

[194] R. Memeo, F. Ciccacci, C. Mariani, and S. Ossicini. On the Use of the Auger Technique for Quantitative Analysis of Overlayers. *Thin Solid Films*, 109:159, 1983.

[195] S. Ossicini, R. Memeo, and F. Ciccacci. AES Analysis of the Growth Mechanism of Metal Layers on Metal Surfaces. *J. Vac. Sci. Technol. A*, 3:387, 1985.

[196] J. Åhlund, J. Schnadt, K. Nilson, E. Göthelid, J. Schiessling, F. Besenbacher, N. Må rtensson, and C. Puglia. The Adsorption of Iron Phthalocyanine on Graphite: a Scanning Tunnelling Microscopy Study. *Surface Science*, 601:3661, 2007.

[197] M.-S. Liao and S. Scheiner. Electronic Structure and Bonding in Metal Phthalocyanines, Metal=Fe, Co, Ni, Cu, Zn, Mg. *The Journal of Chemical Physics*, 114:9780, 2001.

[198] T. Ohta, A. Bostwick, T. Seyller, K. Horn, and E. Rotenberg. Controlling the Electronic Structure of Bilayer Graphene. *Science*, 313:951, 2009.

[199] I. Gierz, C. Riedl, U. Starke, C. R. Ast, and K. Kern. Atomic Hole Doping of Graphene. *Nano letters*, 8:4603, 2008.

[200] X. Wang, J.-B. Xu, W. Xie, and J. Du. Quantitative Analysis of Graphene Doping by Organic Molecular Charge Transfer. *The Journal of Physical Chemistry C*, 115:7596, 2011.

[201] W. Zhang, C.-T. Lin, K.-K. Liu, T. Tite, C.-Y. Su, C.-H. Chang, Y.-H. Lee, C.-W. Chu, K.-H. Wei, J.-L. Kuo, and L.-J. Li. Opening an Electrical Band Gap of Bilayer Graphene with Molecular Doping. *ACS Nano*, 5(9):7517–24, September 2011.

[202] W. Chen, S. Chen, D. C. Qi, X. Y. Gao, and A. T. S. Wee. Surface Transfer p-Type Doping of Epitaxial Graphene. *Journal of the American Chemical Society*, 129:10418, 2007.

[203] H. Huang, S. Chen, X. Gao, W. Chen, and T.A.S. Wee. Structural and Electronic Properties of PTCDA Thin Films on Epitaxial Graphene. *ACS nano*, 3:3431, 2009.

[204] Stephen R. Forrest. Ultrathin Organic Films Grown by Organic Molecular Beam Deposition and Related Techniques. *Chemical Reviews*, 97:1793, 1997.

[205] N. Marom and L. Kronik. Density Functional Theory of Transition Metal Phthalocyanines, I: Electronic Structure of NiPc and CoPc - Self-Interaction Effects. *Applied Physics A*, 95:159, 2008.

[206] N. Marom and L. Kronik. Density Functional Theory of Transition Metal Phthalocyanines, II: Electronic Structure of MnPc and FePc - Symmetry and Symmetry Breaking. *Applied Physics A*, 95:165, 2008.

[207] M. Sumimoto, Y. Kawashima, K. Hori, and H. Fujimoto. Theoretical Investigation of the Molecular, Electronic Structures and Vibrational Spectra of a Series of First Transition Metal Phthalocyanines by Z. Liu et al. *Spectrochimica acta. Part A, Molecular and biomolecular spectroscopy*, 71:286, 2008.

[208] J. Wang, Y. Shi, J. Cao, and R. Wu. Magnetization and Magnetic Anisotropy of Metallophthalocyanine Molecules from the First Principles Calculations. *Applied Physics Letters*, 94:122502, 2009.

[209] J. Bartolomé, F. Bartolomé, L.M. García, G. Filoti, T. Gredig, C.N. Colesniuc, I.K. Schuller, and J.C. Cezar. Highly Unquenched Orbital Moment in Textured Fe-Phthalocyanine Thin Films. *Physical Review B*, 81:195405, 2010.

[210] B.T. Thole and G. van der Laan. Spin Polarization and Magnetic Dichroism in Photoemission from Core and Valence States in Localized Magnetic Systems. *Physical Review B*, 44:424, 1991.

[211] F. Roth, A. König, R. Kraus, M. Grobosch, T. Kroll, and M. Knupfer. Probing the Molecular Orbitals of FePc Near the Chemical Potential Using Electron Energy-Loss Spectroscopy. *The European Physical Journal B*, 74:339, 2010.

[212] S. Stepanow, P. Miedema, A. Mugarza, G. Ceballos, P. Moras, J. Cezar, C. Carbone, F. de Groot, and P. Gambardella. *Physical Review B*.

[213] K. T. Chan, J. B. Neaton, and Marvin L. Cohen. First-Principles Study of Metal Adatom Adsorption on Graphene. *Physical Review B*, 77:235430, 2008.

[214] M.-S. Liao, J.D. Watts, M.-J. Huang, S.M. Gorun, T. Kar, and S. Scheiner. Effects of Peripheral Substituents on the Electronic Structure and Properties of Unligated and Ligated Metal Phthalocyanines, Metal = Fe, Co, Zn. *Journal of Chemical Theory and Computation*, 1:1201, 2005.

[215] V.V. Maslyuk, V.Y. Aristov, O.V. Molodtsova, D.V. Vyalikh, V.M. Zhilin, Y.A. Ossipyan, T. Bredow, I. Mertig, and M. Knupfer. The Electronic Structure of Cobalt Phthalocyanine. *Applied Physics A*, 94:485, 2009.

[216] A. Zhao, Q. Li, L. Chen, H. Xiang, W. Wang, S. Pan, B. Wang, X. Xiao, J. Yang, J.G. Hou, and Q. Zhu. Controlling the Kondo Effect of an Adsorbed Magnetic Ion through its Chemical Bonding. *Science*, 309:1542, 2005.

[217] T. Kroll, V.Y. Aristov, O.V. Molodtsova, Y.A. Ossipyan, D.V. Vyalikh, B. Büchner, and M. Knupfer. Spin and Orbital Ground State of Co in Cobalt Phthalocyanine. *The Journal of Physical Chemistry A*, 113:8917, 2009.

[218] M. Somashekarappa, R.K. Venugopala, M. Harish, and J. Keshavayya. Synthesis, Spectral and Magnetic Susceptibility Studies on Tetrachloro Metal(II)phthalocyanines. *Journal of Molecular Structure*, 753:190, 2005.

[219] C. Baldacchini, C. Mariani, and M.G. Betti. Adsorption of Pentacene on Filled d-Band Metal Surfaces: Long-Range Ordering and Adsorption Energy. *The Journal of Chemical Physics*, 124:154702, 2006.

[220] A. Kanjilal, L. Ottaviano, V. Di Castro, M. Beccari, M.G. Betti, and C. Mariani. Pentacene Grown on Self-Assembled Monolayer: Adsorption Energy, Interface Dipole, and Electronic Properties. *Journal of Physical Chemistry C*, 17:286, 2007.

[221] T.J. Schuerlein and N.R. Armstrong. Pentacene Grown on Self-Assembled Monolayer: Adsorption Energy, Interface Dipole, and Electronic Properties. *Journal of Vacuum Science and Technology A*, 12:1992, 1994.

[222] S. Lukas, S. Vollmer, G. Witte, and Ch. Wöll. Adsorption of acenes on flat and vicinal Cu(111) surfaces: Step Inducend Formation of Lateral Order. *Journal of Chemical Physics*, 114:10123, 2001.

[223] D. Usachov, O. Vilkov, A. Grüneis, D. Haberer, A. Fedorov, V.K. Adamchuk, A.B. Preobrajensi, P. Dudin, A. Barinov, M. Oehzelt, C. Laubschat, and D.V. Vyalikh. Nitrogen-Doped Graphene: Efficient Growth, Structure, and Electronic Properties. *Nano Letters*, 1:5401, 2011.

[224] K. Nilson, J. Åhlund, B. Brena, E. Göthelid, J. Schiessling, N. Mårtensson, and C. Puglia. Scanning Tunneling Microscopy Study of Metal-Free Phthalocyanine Monolayer Structures on Graphite. *The Journal of Chemical Physics*, 127:114702, 2007.

[225] Y. Naitoh, T. Matsumoto, K.-I. Sugiura, Y. Sakata, and T. Kawai. Self-Assembled Stripe Structure of Zinc-Phthalocyanine on Graphite Surfaces. *Surface Science Letters*, 487:L534, 2001.

[226] A.J. Pollard, E.W. Perkins, N.A. Smith, A. Saywell, G. Goretzki, A.G. Phillips, S.P. Argent, H. Sachdev, F. Müller, S. Hüfner, S. Gsell, M. Fischer, M. Schreck, J. Osterwalder, T. Greber, S. Berner, N.R. Champness, and P.H. Beton. Supramolecular assemblies formed on an epitaxial graphene superstructure. *Angewandte Chemie International Edition*, 49:1794, 2010.

[227] P. Sutter, J.T. Sadowski, and E. Sutter. Graphene on Pt(111): Growth and Substrate Interaction. *Physical Review B*, 80:245411, 2009.

[228] M. Gao, Y. Pan, L. Huang, H. Hu, L.Z. Zhang, H.M. Guo, S.X. Du, and H.-J. Gao. Epitaxial Growth and Structural Property of Graphene on Pt(111). *Applied Physics Letters*, 98:033101, 2011.

[229] B.T. Thole, P. Carra, F. Sette, and G. van der Laan. X-Ray Circular Dichroism as a Probe of Orbital Magnetization. *Physical Review Letters*, 68:1943, 1992.

[230] P. Carra, B.T. Thole, M. Altarelli, and X. Wang. X-Ray Circular Dichroism and Local Magnetic Fields. *Physical Review Letters*, 70:694, 1993.

[231] M.G. Betti et al. . *to be published*, 2012.